

# **Politecnico di Torino**

Master of Science in Biomedical Engineering



Master Thesis

## **Design and optimization of hybrid formulations based on PLLA and inorganic phases for 3D printing of bone scaffolds**

### **Supervisors**

Prof.ssa Sonia Lucia Fiorilli  
Prof.ssa Chiara Vitale Brovarone  
Prof. Kenny Dalgarno

### **Candidate**

Ilaria Corvaglia

Academic Year 2019/2020







## Table of contents

List of figures .....	7
List of tables .....	9
Introduction .....	10
1 – Biomaterials for bone tissue engineering .....	12
1.1 Bone tissue.....	13
1.2 Osteoporosis .....	17
1.3 Mesoporous bioactive glasses .....	20
1.3.1 Bioactive materials .....	20
1.3.2 Bioactive glasses.....	20
1.3.3 Mesoporous materials .....	24
1.3.4 Mesoporous bioactive glasses .....	27
1.3.5 Synthesis methods .....	29
1.3.6 Bioactive properties.....	30
1.4 Hydroxyapatite .....	32
1.5 Thermoplastic polymers for medical applications.....	36
2 – Scaffold for bone tissue engineering .....	43
2.1 Scaffold for bone tissue engineering .....	44
2.1.1 Polymeric scaffold production.....	45
2.2 Scaffold functionalisation strategies.....	49
2.3 Additive manufacturing (AM) techniques: printing of bone scaffolds.....	51
2.4 Composite materials in additive manufacturing .....	56
3 – Materials and methods.....	60
3.1 Materials .....	61
3.1.1 Synthesis of MBG containing strontium ions by sol-gel synthesis in basic medium.....	61
3.1.2 Synthesis of MBG containing strontium ions by aerosol-assisted spray-drying process .....	62
3.1.3 Incorporation of bioactive inorganic phases in PLLA pellets .....	64
3.1.4 Extrusion process of pure PLLA and hybrid formulations.....	67
3.2 Methods of characterization .....	71
3.2.1 Nitrogen adsorption-desorption.....	71
3.2.2 Field emission scanning electron microscopy (FESEM).....	72
3.2.3 Energy dispersive X-ray Spectroscopy (EDS) .....	74
3.2.4 X-ray Diffraction (XRD).....	75
3.2.5 Strontium ion release test from inorganic phases .....	77
3.2.6 Tensile testing.....	78

3.2.7 Rheological characterization .....	81
4 – Results and discussion .....	86
4.1 Characterization of mesoporous bioactive glasses containing strontium ions .....	86
4.1.1 MBG containing strontium ions: aerosol-assisted spray-drying process (MBG_SG_10%Sr) .....	86
4.1.2 MBG containing strontium ions: sol-gel synthesis in basic medium (MBG_SG_10%Sr) .....	91
4.2 Characterization of nano-hydroxyapatites .....	95
4.3 Characterization of extruded pure PLLA and composite filaments .....	99
4.3.1 Morphological assessment of the extruded filaments .....	99
4.3.2 Compositional assessment of the extruded filaments .....	103
4.3.3 Mechanical properties of the extruded filaments .....	108
4.3.4 Rheological properties of the extruded filaments .....	111
5 – Conclusions and future perspectives .....	124
5.1 Conclusions .....	124
5.2 Future perspectives .....	129
Bibliography .....	130
Acknowledgments .....	138

## List of figures

Figure 1: The organization of osteons and lamellae in compact long bone. <sup>5</sup> .....	14
Figure 2: Classification of bone cells based on source, resorption and formation function. <sup>4</sup> .....	15
Figure 3: Left: Projection of the proposed structure of collagen along the fibre axis. Right: Ball and stick diagram showing two projections of collagen structure. Each chain has a different colour ribbon drawn through the backbone. <sup>8,9</sup> .....	16
Figure 4: Expected costs in 2050 based on changes in demography.....	19
Figure 5: 2D presentation of random glass network modifiers and network formers. <sup>29</sup> .....	21
Figure 6: Phase diagram indicating the glass-forming region as proposed by Hench. <sup>24</sup> .....	22
Figure 7: Pore size scales according to IUPAC terminology. <sup>31</sup> .....	24
Figure 8: Representation of some arrangements for amphiphilic molecules.....	25
Figure 9: Formation of mesoporous materials by structure-directing agents: a) true liquid-crystal template mechanism, b) cooperative liquid-crystal template mechanism. <sup>37</sup> .....	26
Figure 10: N <sub>2</sub> adsorption-desorption isotherm of calcinated MBG in presence of P123 template. The inset shows a plot of the pore size distribution. ....	28
Figure 11: Sequence of the interfacial reactions involved in forming the bond between tissue and bioactive glass, focusing on bone-tissue interface. <sup>40</sup> .....	30
Figure 12: Crystal structure of stoichiometric hydroxyapatite. <sup>47</sup> .....	32
Figure 13: Structure of biopolymers. <sup>52</sup> .....	37
Figure 14: Stereoisomeric forms of lactide. <sup>56</sup> .....	39
Figure 15: Production of poly-L-lactic acid (PLLA). <sup>52</sup> .....	40
Figure 16: Schematic representation of solvent casting technique. <sup>76</sup> .....	45
Figure 17: Schematic representation of freeze-drying process. <sup>77</sup> .....	46
Figure 18: Schematic of electrospinning system. <sup>79</sup> .....	48
Figure 19: Example of fibres produced from electrospinning.....	49
Figure 20: Stereolithography approaches. Left: a bottom-up approach with laser beam. Right: a top-down approach with light projection. <sup>89</sup> .....	53
Figure 21: Schematic of direct 3D printing. <sup>87</sup> .....	55
Figure 22: Example of structures obtained by AM. Left: scaffold produced by FDM. Right: scaffold and detail magnification of a structure produced by 3D printing. <sup>75,92</sup> .....	56
Figure 23: Schematic representation of spray-drying mechanism. 1) Atomization. 2) Droplet-to-particle conversion. 3) Particle collection. <sup>105</sup> .....	62
Figure 24: Mini Spray-Dryer B-290 Büchi Labortechnik. ....	63
Figure 25: Pellets production. Left: PLLA mixed with HA suspension. Right: dried pellets. ....	66
Figure 26: Stirring of MBG_SG_10%Sr aqueous suspension. ....	67
Figure 27: Left: Rondol 10mm Twin Screw Mini Extruder. Right: Rondol Haul-Off.....	68
Figure 28: Schematic representation of a single-screw extruder. <sup>107</sup> .....	68
Figure 29: ASAP2020 from Micrometrics for N <sub>2</sub> adsorption-desorption analysis.....	72
Figure 30: Schematic diagram of FESEM. <sup>114</sup> .....	73
Figure 31: FESEM ZEISS MERLIN with EDS analyser.....	75
Figure 32: Diffraction phenomenon. ....	76
Figure 33: Shimadzu 1kN testing machine in G15 laboratory. ....	78
Figure 34: Example of tensile – elongation curve from a tensile test for a ductile material. <sup>120</sup> .....	79
Figure 35: Example of the grip used to hold the filaments. <sup>121</sup> .....	80
Figure 36: Quantification of shear rate and shear stress for layers of fluids sliding over one another. <sup>122</sup> .....	81
Figure 37: Shear stress/shear rate plots depicting various types of flow behaviours. <sup>122</sup> .....	83
Figure 38: Left: DHR-2 rotational rheometer. Right: Detail of the 25 mm parallel plate geometry.....	84

Figure 39: FESEM micrographs of MBG_SD_10%Sr sample. ....	86
Figure 40: EDS spectrum of MBG_SD_10%Sr sample. ....	88
Figure 41: N <sub>2</sub> adsorption-desorption isotherm of MBG_SD_10%Sr sample. ....	89
Figure 42: Pore size distribution of MBG_SD_10%Sr sample. ....	90
Figure 43: Release kinetics of strontium from the MBG_SD_10%Sr in Tris-HCl buffer at 37°C and pH 7.4. The results are expressed as average ± standard deviation. ....	91
Figure 44: FESEM micrographs of MBG_SG_10%Sr sample. ....	91
Figure 45: EDS spectrum of MBG_SG_10%Sr. ....	92
Figure 46: N <sub>2</sub> adsorption-desorption isotherm of MBG_SG_10%Sr sample. ....	93
Figure 47: Pore size distribution of MBG_SG_10%Sr sample. ....	93
Figure 48: Release kinetics of strontium from the MBG_SG_10%Sr in Tris-HCl buffer at 37°C and pH 7.4. The results are presented as average ± standard deviation. ....	95
Figure 49: FESEM micrographs of nano-HA. Up left: HA_0%Sr. Up right: HA_50%Sr. Down: HA_100%Sr. ....	96
Figure 50: XRD patterns of pure nano-HA (HA_0%Sr) and substituted HA (50 and 100% Sr ion content). ....	98
Figure 51: Release kinetics of strontium from HA_50%Sr and HA_100%Sr in Tris-HCl buffer at 37°C and pH 7.4. The results are expressed as average ± standard deviation. ....	99
Figure 52: Left: Pure PLLA filaments after the first extrusion process. Right: Detail of PLLA_HA_50%Sr filament after the first extrusion process. ....	100
Figure 53: Left: PLLA_MBGS_D_10%Sr filaments after the second extrusion process. Right: PLLA_HA_50%Sr filaments after the second extrusion process. ....	101
Figure 54: SEM micrographs of the cross-sections of the performed experiments. A: PLLA. B: PLLA_MBGS_D_10%Sr. C: PLLA_MBGS_S_10%Sr. D: PLLA_HA_0%Sr. E: PLLA_HA_50%Sr. F: PLLA_HA_100%Sr. ....	102
Figure 55: EDS spectrum of PLLA filament. Insert: detail of the element distribution. Yellow represent oxygen and blue represents carbon. ....	103
Figure 56: Up: EDS spectrum of PLLA_MBGS_D_10%Sr sample. Insert: detail of the scanned zone. Elemental distribution. Down: EDS spectrum of PLLA_MBGS_S_10%Sr sample. Insert: detail of the scanned zone. Elemental distribution. Yellow represents oxygen, green is carbon, blue is silicon and pink is strontium. ....	104
Figure 57: Up: EDS spectrum of PLLA_HA_0%Sr sample. Insert: detail of the scanned zone. Elemental distribution. Middle: EDS spectrum of PLLA_HA_50%Sr sample. Insert: detail of the scanned zone. Elemental distribution. Down: EDS spectrum of PLLA_HA_100%Sr sample. Insert: detail of the scanned zone. Elemental distribution. Yellow represents oxygen, green is carbon, red is phosphorous, blue if presented is calcium and pink if presented is strontium. ....	106
Figure 58: Stress-strain curves for the extruded filaments. ....	108
Figure 59: Frequency sweep tests of PLLA, PLLA_MBGS_D_10%Sr and PLLA_MBGS_S_10%Sr samples. ....	113
Figure 60: Frequency sweep tests of PLLA_HA_0%Sr, PLLA_HA_50%Sr and PLLA_HA_100%Sr samples. ....	114
Figure 61: Flow ramps of PLLA, PLLA_MBGS_D_10%Sr and PLLA_MBGS_S_10%Sr samples. ....	120
Figure 62: Flow ramps of PLLA_HA_0%Sr, PLLA_HA_50%Sr and PLLA_HA_100%Sr samples. ....	121

## List of tables

Table 1: Remaining lifetime probability of fracture (%) in men and women from Sweden at the ages shown. ....	18
Table 2: Clinical risk factors associated with increased risk of fragility fractures. ....	18
Table 3: Typical values of composition and textural properties of both families of glasses. <sup>34</sup> .....	27
Table 4: Mechanical and thermal properties of dense HA. <sup>24,48</sup> .....	33
Table 5: Characteristic features of the HA production properties. <sup>49</sup> .....	34
Table 6: Different coating techniques for HA. ....	35
Table 7: Mechanical properties of some biopolymers. <sup>32</sup> .....	42
Table 8: Summary of the mechanical properties of human bone. <sup>70</sup> .....	44
Table 9: Geometrical factors and architecture of some scaffold fabrication technologies. ....	47
Table 10: Fibre diameter behaviour as some process or solution parameters change. ....	49
Table 11: Growth factors acting on bone repair. <sup>83</sup> .....	50
Table 12: Summary of 3D printers based on printing type, matrix and fillers. ....	57
Table 13: General specification of the HA suspensions from Fluidinova. ....	65
Table 14: Weight of the PLLA pellet and provided suspensions in the desired concentration. ....	65
Table 15: Weighted material to prepare water suspensions. ....	66
Table 16: Weight of the PLLA pellets and suspensions for each formulation. ....	67
Table 17: Parameters used in the extrusion of pure PLLA sample. ....	69
Table 18: Parameters used in the extrusion of PLLA_HA_0%Sr and PLLA_HA_100%Sr samples. ....	70
Table 19: Parameters used in the second extrusion of PLLA_HA_50%Sr, PLLA_MBG_SD_10%Sr and PLLA_MBG_SG_10%Sr samples. ....	70
Table 20: Dilutions for ICP analysis. ....	77
Table 21: Experimental conditions for tensile test. ....	80
Table 22: Relationships between spray-drying parameters. <sup>105</sup> .....	87
Table 23: Weight and atomic percentage of the elements in MBG_SD_10%Sr sample.....	88
Table 24: Results of the BET analysis from MBG_SD_10%Sr sample.....	90
Table 25: Weight and atomic percentage of the elements in MBG_SG_10%Sr sample.....	92
Table 26: Results of the BET analysis from MBG_SG_10%Sr sample.....	94
Table 27: Dimensions of nano-HA samples.....	96
Table 28: (Ca+Sr)/P ratio calculated from EDS analysis for HA samples.....	97
Table 29: Atomic and weight concentration of PLLA sample. ....	103
Table 30: Atomic and weight concentration of PLLA_MBG_SD_10%Sr and PLLA_MBG_SG_10%Sr samples. ....	105
Table 31: Atomic and weight concentration of PLLA_HA_0%Sr, PLLA_HA_50%Sr and PLLA_HA_100%Sr samples.....	107
Table 32: Tensile strength and Young's modulus of the filaments in comparison to bone tissue values. ....	110
Table 33: Strain of the extruded filaments. The results are presented as average $\pm$ standard deviation. ....	110
Table 34: Crossover frequencies of the performed samples.....	116
Table 35: Storage and loss modulus of the performed samples at 1 rad/s.....	117
Table 36: Viscosity parameters of the performed samples at 1 and 100 s <sup>-1</sup> . ....	122

## Introduction

The present work is framed in the H2020 GIOTTO project where the general aim is to develop medical devices with the ability to affectively treat osteoporotic fractures. Osteoporosis is a worldwide degenerative pathology that affect people, generally after the age of 50 years, reducing their quality of life and burdening the health system. This disease is due by an imbalance between bone resorption and deposition. The constant ageing of population is leading to a continuous growth of affected people. In this context, the scope is to develop a customized device able to inspire and stimulate bone renewal in elderly people, whose regeneration ability is decreased because of the abovementioned pathology.

In particular, the aim of the work is the synthesis and fabrication of hybrid formulations based on biodegradable polymer and osteoinductive inorganic phases, that will then be used to fabricate a customized and bioactive device. Key is the synthesis and characterization of the inorganic phases (chosen are hydroxyapatite and mesoporous bioactive glasses), their incorporation within a polymeric matrix and the extrusion of the prepared hybrid formulations. Main focus of the work is to discuss the best incorporation method and characterize the obtained composites to evaluate the most suitable material for the fabrication.

Hydroxyapatite (HA) is a calcium phosphate, which constitutes the mineralized phase of human bone and teeth. HA can be produced through synthetic routes and incorporated into medical devices, being recognised for its ability to promote bioactivity. Moreover, a crucial advantage is its analogous morphology and composition to biological apatite, then becoming an ideal source for implantation purposes and bone regrowth.

Mesoporous bioactive glasses (MBG), have gained great attention in the medical field due to their high bioactivity and excellent structural properties, in terms of specific area and pore volume. The presence of a mesoporous structure (defined by a pore diameter comprised between 2 and 50 nm) favours ion exchange, inducing an osteoinductive behaviour and is suitable for therapeutic agent (drugs or ions) release.

The present work is based on the production of polymeric filaments, obtained through extrusion process, comprising inorganic phases and assess their mechanical and rheological properties. The filaments are the base material used by Fused Filament Fabrication (FFF) machines to create the device. FFF is part of Additive Manufacturing (AM), new processing technologies with the ability to generate complex and various shaped structures characterized by high porosity at different scales. This type of technology, in particular, is a liquid-based process founded on material extrusion. The deposition of the extruded material is controlled by a software that realizes the cross-section of the desired device. A crucial downside is the low choice of materials that can be used for fabrication using this method. Thermoplastic polymers as PLA are generally utilized because of their good melt viscosity properties, as are able to maintain their shape and sustain the developing structure. A benefit of this technology is the little wasted material during fabrication. The molten material will be deposited onto the previous layer and, as it solidifies, the two layers are joined.

The first part of the work consists in the synthesis of the inorganic phases that will be successively incorporated into the polymeric matrix to obtain the hybrid formulation. In particular, MBGs are prepared and fully characterized in DISAT laboratories, IRIS group, at Politecnico di Torino. MBGs are produced through two different synthesis routes, a batch sol-gel in basic medium and spray-drying aerosol-assisted sol-gel procedure. Strontium is known for its ability to promote osteogenesis, therefore improving bone remodelling; because of this beneficial effect, the bioactive phases are combined with a constant concentration of strontium ion (10% molar). At variance, the nano-HA are provided by a project partner of GIOTTO consortium and are fully characterized at Politecnico di Torino. The HA is provided with different degrees of strontium ion substitution (0 – 50 – 100%). Physicochemical characterization is performed on both inorganic phases to evaluate the structural, compositional properties and assess the ion release kinetic.

The second part of the work is focussed on the incorporation of inorganic phases within a polymeric matrix. The chosen polymer is poly L-lactic acid (PLLA), known for its good mechanical properties. Polymer combining with inorganic phases, filament extrusion and evaluation of mechanical properties are conducted at Newcastle University, in Newcastle Upon Tyne, United Kingdom. Firstly, the inorganic phases in form of suspensions are dispersed within PLLA polymeric matrix. Here, a physicochemical characterization is performed on polymer alone and including the inorganic phases, after being extruded into filaments. The characterization estimated the influence of HA and MBGs on polymer mechanical behaviour and allowed to understand how the ion release is affected once the particles are embedded into the polymer matrix.

## 1 – Biomaterials for bone tissue engineering

The present chapter will focus on bone tissue, highlighting its fundamental features, used as inspiration for the design of the medical device. An overview of osteoporosis is also given describing the personal and social impact of the disease, the number of people affected and its economic impact.

It will then focus on the description of the materials used in the present work, namely the description of their properties and applications in the field of bone regeneration. In particular, the chapter focuses on the description of mesoporous bioactive glasses (synthesis methods and bioactive properties) and on hydroxyapatite, highlighting its similarity to the inorganic phase of human bone, and its importance in the bioactivity processes. The chapter will be concluded with a description of thermoplastic polymers, their tuneable mechanical properties and degradation profiles.

## 1.1 Bone tissue

Human bone is a dynamic, mineralized, highly vascularized connective tissue with the ability to remodel throughout life by regulated activity of bone-forming (osteoblasts) and bone-resorbing cells (osteoclasts).<sup>1</sup> Present are also osteocytes, which comprise 90 – 95% of the total bone cells. Bone is characterized by its rigidity and great resistance to traction and compression, providing support to body and protection to the soft organs. Moreover, it participates on the generation of movement in cooperation with muscles. Additionally, when calcium and phosphorus ionic concentration increases in the blood current, bone tissue acts as the main depot, where the ions can be stored.<sup>2</sup>

The extracellular matrix is composed of water, organic (20-30%) and inorganic (60-70%) compounds. The main organic components are collagenous proteins (especially Type I collagen, up to 90% of the organic mass), non-collagenous proteins, growth factors and proteoglycans. The inorganic components are calcium phosphate (86%) in the form of hydroxyapatite crystals, calcium carbonate (12%), magnesium phosphate (1.5%), magnesium fluoride (0.5%) and traces of iron oxide.<sup>3</sup>

All bones are covered with periosteum, a connective membrane highly innervated and vascularized. Periosteum helps in the bone formation process during a person's growth, sustaining the tissue with the necessary vasculature and nutritional factors. Sharpey' fibres, a matrix of connective tissue predominantly made of Type I collagen, allow a strong periosteum-bone connection penetrating through a certain depth within bone tissue.<sup>3</sup>

Based on their density and histoarchitecture bones are divided in two phases, cortical and trabecular. Cortical tissue is characterized by a highly homogeneous bone layer while trabecular bone is a high porous structure (from 50 up to 90%). Trabecular bone makes up approximately one-fifth of the bone mass and occupies much of the medullary cavity. This tissue is extremely rich of blood supply and various populations of progenitor cells. It is characterized by the presence of trabeculae, with various shape and thickness, adjacent to irregular cavities. The trabeculae are arranged differently in their directions to guarantee the suitable resistance and stiffness and can realign in case of stress change.<sup>4</sup>

The bone tissue can be classified in lamellar and non-lamellar. The difference between the two types of bone tissue is the presence, or absence, of an organized structure. The lamellar bone tissue characterizes most bones and its basic structure is osteon (few millimetres long and hundreds of micrometres thick).<sup>3</sup> The osteon is defined by a central Haversian canal, occupied by blood vessels, nerve fibres and lymphatic vessels. In compact bone, it is surrounded by concentric lamellae of matrix, as shown in figure 1. Lamellae contain collagen fibres, arranged in parallel to bone length and a small number of proteoglycans. Cells can be found in spaces called *lacunae* between the matrix rings which are linked to one another and to the Haversian canal through Volkmann's canals.<sup>4</sup>

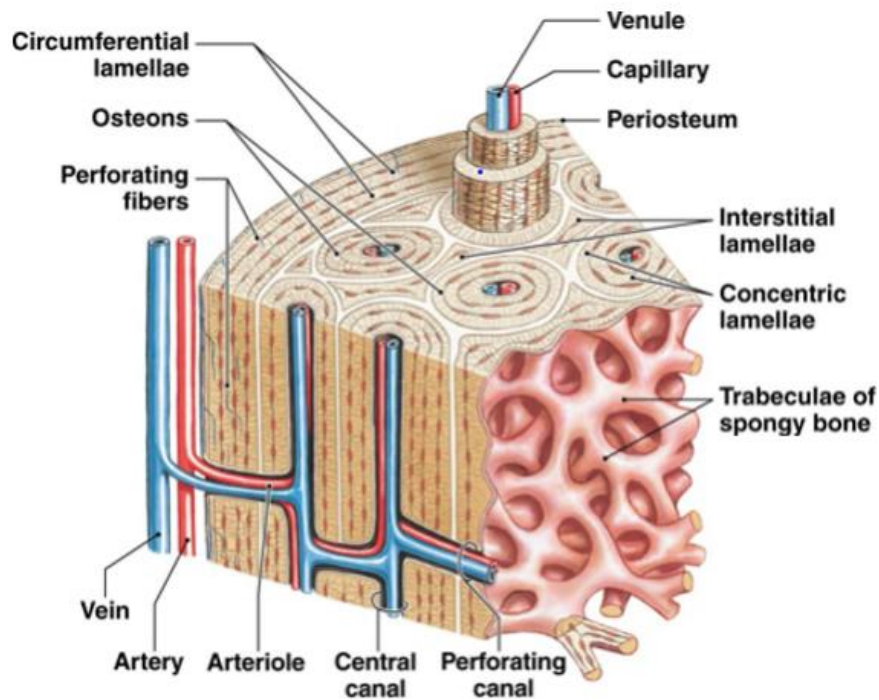


Figure 1: The organization of osteons and lamellae in compact long bone.<sup>5</sup>

Bone tissue function depends majorly on 3 cell-types, (Fig. 2):<sup>2</sup>

- Osteoblasts: cuboidal cells derived from mesenchymal stem cells (MSCs), located along the bone surface. Their main function is to synthesise new bone matrix through deposition of organic matrix and then its mineralization. The first phase of mineralization, also named vesicular, occurs when matrix vesicles (with a variable diameter from 30 to 200 nm) are released from the osteoblasts into the newly formed bone matrix. Those vesicles bind to proteoglycans and other organic components which, due to their negative charge, cause the immobilization of calcium ions stored within the vesicles. The phosphate ions are stored inside the vesicles thanks to the degradation of phosphate-containing compounds, degraded by the alkaline phosphatases. The phosphate and calcium ions inside the vesicles nucleate, forming HA crystals. The second phase of mineralization process, fibrillar, occurs when the supersaturation of calcium and phosphate ions inside the vesicles leads to the rupture of these structures and the hydroxyapatite crystals spread to the surrounding matrix.
- Osteocytes: cells with a dendritic morphology derived from the MSCs lineage through osteoblast differentiation. After new bone mineralization, osteoblasts within the lacunae are surrounded by bone matrix and become osteocytes. The transformation process is accompanied by conspicuous morphological and structural changes, including the reduction of the round osteoblast size. The number of organelles such as rough endoplasmic reticulum and Golgi apparatus decreases, corresponding to a decrease in the protein synthesis and secretion. The osteocytes are rich in lysosomes, providing the necessary enzymes for the osteolytic activity.<sup>3</sup> The osteocytes communicate

with other cells by interstitial fluid, which flows within the canaliculi. Thanks to this canalicular system, these cells act as mechanosensors regulating stresses and mechanical forces. Moreover, the osteocytes, can control the osteoblasts and osteoclasts activity, hence can maintain bone matrix and control bone remodelling.

- Osteoclasts: terminally differentiated multinucleated cells derived from the hematopoietic stem cells lineage, responsible for bone resorption. Those cells can reach 100  $\mu\text{m}$  in dimensions, having a slightly acidic cytoplasm rich of ribosomes and lysosomes. The osteoclasts can secrete acid hydrolases, which are able to dissociate minerals and destroy collagen fibres. Other osteoclasts functions are the production of factors called clastokines that control osteoblast during the bone remodelling cycle, the direct regulation of the hematopoietic stem cell niche and contribute to blood to bone calcium exchange.<sup>3</sup>

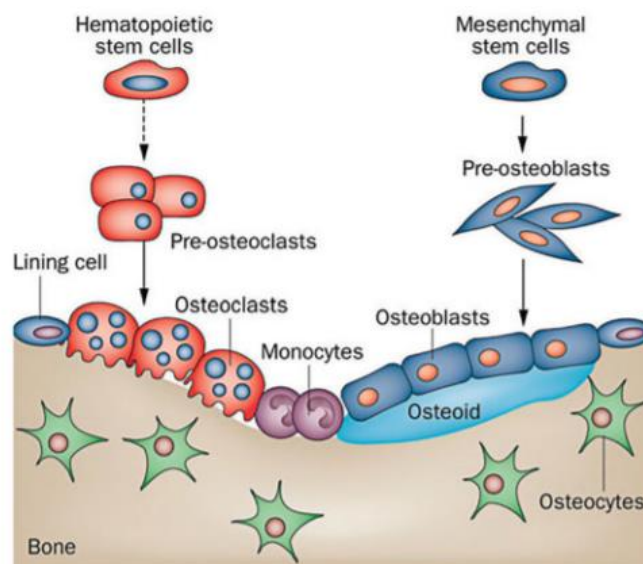


Figure 2: Classification of bone cells based on source, resorption and formation function.<sup>4</sup>

In human bone, the most abundant organic component is Type I collagen (Fig. 3) providing elasticity and toughness. Bone strength is explained not only by the interaction between the mineral phase and collagen but also by the orientation of collagen fibres according to the load direction. For example, the femur can resist significant vertical compressive load without substantial damage. In contrast, the same load applied transversally may cause fractures. The strength of bone is higher in the direction of physiological loading that corresponds, in the cortical bone, to the orientation of osteons, and consequently that of the collagen fibres.<sup>6</sup> In woven and trabecular bone instead, unorganized collagen fibres contribute to a decreased mechanical properties.<sup>7</sup> In case of cortical bone, as the osteons are highly packed, density rises up to 90-95%, whilst trabecular bone is highly porous due to its morphological organization. Being it a network of trabeculae, the porosity is high, from 50 to 90%. Consequently, because of the different tissue organisation, the mechanical

properties of the two phases are different. In particular, cortical bone is stiffer than trabecular bone, meaning it can bear higher loads. This confirms that collagen orientation is an influencing factor in the ability of bone to bear stress, but also its morphological structure affects the final properties.

In general, all types of collagen have a rod shape and consist of a right-handed triple helix composed of three polypeptide chains,  $\alpha$  chains, with the characteristic sequence Gly-X-Y. Each of the three  $\alpha$  chain forms an extended left-handed helix. The X and Y positions are usually occupied by proline and hydroxyproline, even though other amino acids can be present in the collagen structure.<sup>8</sup>

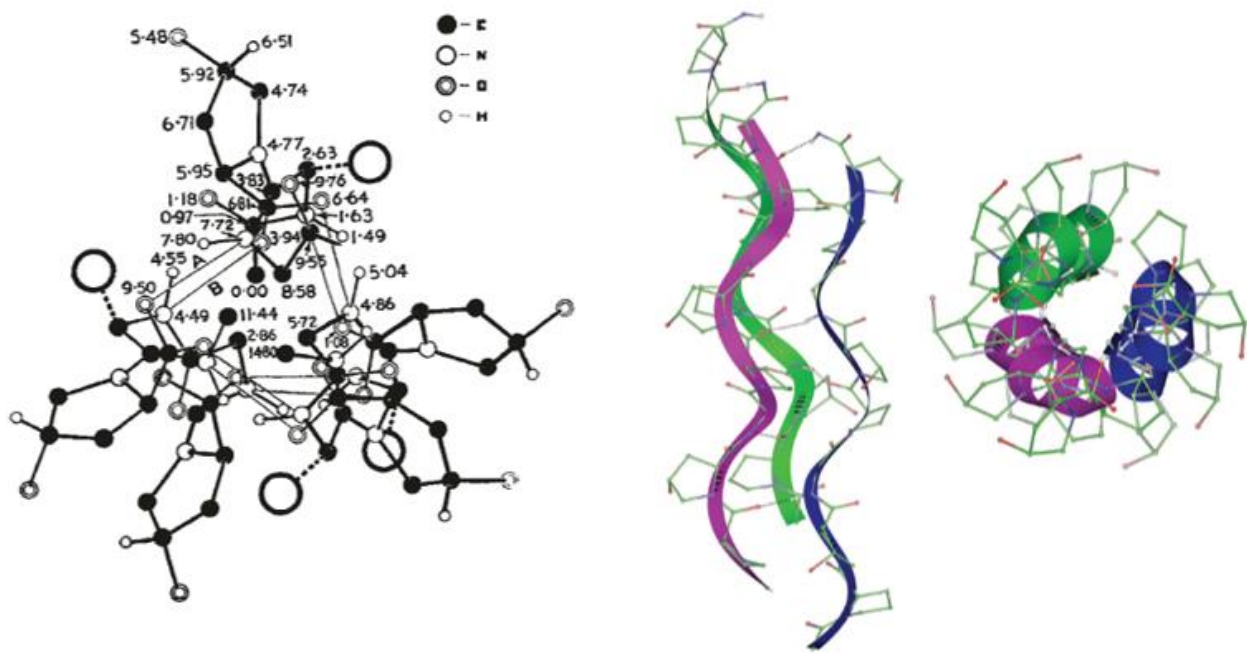


Figure 3: Left: Projection of the proposed structure of collagen along the fibre axis. Right: Ball and stick diagram showing two projections of collagen structure. Each chain has a different colour ribbon drawn through the backbone.<sup>8,9</sup>

Collagen has three different  $\alpha$  chains, described as  $\alpha_1$ ,  $\alpha_2$ ,  $\alpha_3$ . The collagen Type I triple helix is usually characterized by two identical  $\alpha_1(I)$ -chains and one  $\alpha_2(I)$ -chain and *in vivo* is often coupled with Type V collagen.<sup>10</sup>

Bone formation can follow two distinct routes called intramembranous ossification and endochondral ossification. Intramembranous ossification is the characteristic route in which the flat bones (e.g. skull bones) are formed and is based on the direct conversion of mesenchymal tissue into bone. In endochondral ossification the mesenchymal cells differentiate into cartilage, later replaced by bone. The process is rather complex and involves several stages. On first, the mesenchymal cells are committed by paracrine factors to become cartilage cells, then condensed into compact nodules. The nodules can differentiate into chondrocytes and rapidly proliferate to form the model of the bone. The chondrocytes then will stop proliferating increasing instead their

volume, becoming hypertrophic chondrocytes. Those cells are able to mineralize the matrix by adding calcium carbonate. In the last phase blood vessel will invade the cartilage tissue, while hypertrophic chondrocytes die by apoptosis. As cartilage cells die, the surviving cells are able to differentiate into osteoblasts. Ultimately, all the cartilage is replaced by bone.<sup>11</sup>

Bone remodelling is needed for fracture healing, skeleton adaptation and calcium homeostasis but an imbalance in bone resorption and formation leads to several diseases (osteoporosis in case of exaggerated resorption and osteopetrosis in case of exaggerated bone formation).

The process of remodelling in bone is determined by the cooperation of all types of cells. It starts with osteoclast formation and osteoclast-mediated bone resorption, followed by a reversal period and a long phase of bone matrix formation and mineralisation. Osteoclasts activation may be initiated by a range of local factors released from nearby cells. This process is followed by their fusion and attachment to bone surface. In the resorption phase, osteoclasts generate an acidic microenvironment between the cell-bone surface, dissolving the mineral content of bone. After resorption, mononuclear phagocytes of hemopoietic origin or osteoblast-lineage cells complete the resorption process. The osteoclasts then undergo apoptosis and osteoblasts are recruited. Osteoblasts can rapidly deposit woven bone, but for lamellar bone the process is slower. The mechanism behind this process is still not clear as the type of reformed bone depends partially on how collagen and other proteins are deposited by the osteoblasts. In the formation phase, osteoblasts work together and communicate to each other through gap junctions as well as by the expression of membrane-bound and released biofactors (IGFs, BMPs, TGF $\beta$ , PDGF and FGF).<sup>12,13</sup>

The next section will be dedicated to osteoporosis, one of the most challenging diseases in the scientific community.<sup>2</sup>

## 1.2 Osteoporosis

The osteoporotic disease, as defined by World Health Organisation, is characterized by “low bone mass and micro architectural deterioration of bone tissue, leading to enhanced bone fragility and consequent increase in fracture risk”.<sup>14</sup> The number of people affected by this pathology is constantly growing because of the increased longevity of the population, in both first and third world countries.<sup>15</sup> In 1990 the number of hip fractures was 1.7 million worldwide and, based on recent projections, the number in 2050 could rise to 21 million. Those projections underline that 50% of women and 25% of men between 50 and 85 years old will sustain an osteoporotic fracture.<sup>15,16</sup>

The most common osteoporotic fractures occur at forearm, hip and spine, even though fractures at other sites are also associated with low bone mass and could be considered osteoporotic. Table 1 shows the lifetime

fracture risk in both women and men at age 50 and 80. It could be noticed that the female population is subjected to a higher risk, which can be linked to menopause. During menopause, generally affecting women after 50, oestrogen deficiency impairs the normal bone remodelling cycle by increasing osteoclastic resorption without a corresponding increase in osteoblastic activity. This process is also associated with negative calcium balance caused by its malabsorption, consequently leading to an increased risk of fractures. Malabsorption of calcium can be caused by two separated processes, a primary unspecified defect involving the gut and a secondary step due to the decreased production of a type D vitamin by the aging kidney. Vitamin D is known to be important for muscle function, though both the maintenance of serum calcium and a direct effect on skeletal muscle growth and differentiation. Its deficiency will lead to an aggravation of hyperparathyroidism and increasing bone resorption.<sup>15,14</sup>

Table 1: Remaining lifetime probability of fracture (%) in men and women from Sweden at the ages shown.

Type of fracture	At 50 years		At 80 years	
	Men	Women	Men	Women
Forearm	4.6	20.8	1.6	8.9
Hip	10.7	22.9	9.1	19.3
Spine	8.3	15.1	4.7	8.7
Proximal humerus	4.1	12.9	2.5	7.7
Other	22.4	46.4	15.3	31.7

Other clinical risk factors leading to an increased hazard of fragility fractures are listed in Table 2 and can be divided in risk factors associated with low bone mineral density (BMD) and risk factors linked to falls.<sup>16</sup>

Table 2: Clinical risk factors associated with increased risk of fragility fractures.

Risk factors associated with low BMD	Risk factors for falls
Parental history of fragility fractures	Age
Premature menopause	Poor vision
Poor neuromuscular function	Sarcopenia
Alcohol intake	Malnutrition
Smoking	Dehydration
Prolonged immobilization – inactivity	Neurological risk factors
Type I diabetes	Environmental risk
Vitamin D insufficiency	Depression
Stroke	Urgent urinary incontinence
Hematologic disorders	Reduced sunlight exposure

The fractures caused by osteoporosis have worrisome consequences on both individual and societal levels. Concerning the personal level, the patient suffers pain, a long-time recovery, decreased functional mobility (often associated with partial or total loss of walking independence),<sup>17</sup> and increased mortality. As for the societal level, the main issues are related to the costs of fractures. They could be divided into *inpatient costs*, related to hospital care and rehabilitation, *outpatient costs*, including medications and home care and *family costs*, counting the informal care costs. According to recent projections, the costs of osteoporotic disease in EU will reach €76.7 billion in 2025, more than double of 2010, where the costs were estimated at €30.7 billion.<sup>16,18</sup> Figure 4 shows the expected costs in 2050 in United States, Europe and China.<sup>16</sup>

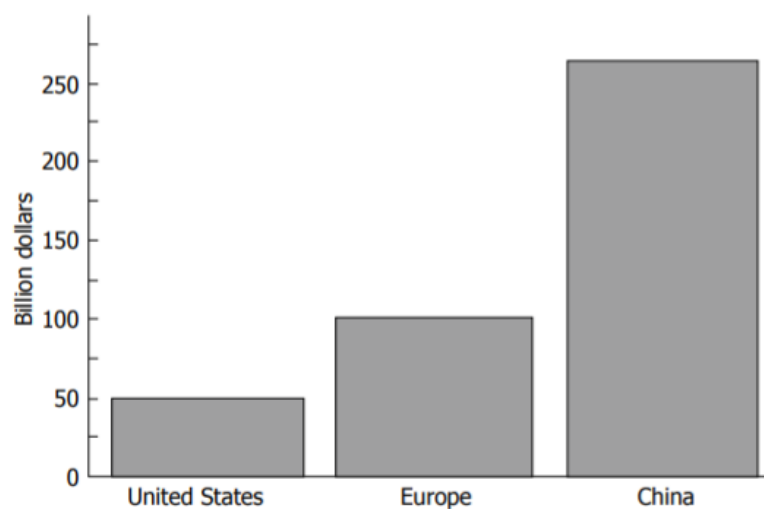


Figure 4: Expected costs in 2050 based on changes in demography.

Moreover, it should be considered the possibility of re-fracture, as the risk of a second fracture is 2.3% per year tending to increase regardless of the results obtained for BMD.<sup>19</sup>

Current treatments are based on pharmacological therapies. Widely prescribed are bisphosphonates, monoclonal antibody medications, hormone-related therapy and bone-building medications. All the mentioned methods possess severe side effects including nausea, abdominal pain and heartburn-like symptoms. Other effects are related to an increased risk of fracture if the medication is stopped, then it would be supportive to treat bone fractures differently. The patient would sustain less risks and suffer less pain in the case of implantation of a specific device able to improve bone healing, sustaining new bone formation and contrasting bone resorption. This would reduce the associated social costs, guaranteeing a faster recovery and a greater quality life for patients.<sup>20</sup>

## 1.3 Mesoporous bioactive glasses

### 1.3.1 Bioactive materials

A bioactive material can be described as a material that is able to develop a series of surface reactions, when implanted into the body, leading to the formation of a bond with both hard and soft tissues.<sup>21</sup> In the specific glass context, bioactivity is the ability to form a hydroxycarbonated apatite layer (HCA) on the glass surface derived from the contact of glass with the solutions mimicking human plasma, such as simulated body fluid, (SBF), developed by Kokubo et al.<sup>22</sup>. The formed HCA phase is equivalent chemically and structurally to the mineral phase of human bone, thus leading to the adhesion of native tissue.<sup>23</sup> Bioactive glasses are defined a class A material within bioactive materials, meaning it should be compatible with the surrounding living tissues, non-mutagenic, non-carcinogenic, and non-antigenic, in order to avoid adverse effects on the cells.<sup>24</sup>

This glass was based on a 45% SiO<sub>2</sub> - 24.5% Na<sub>2</sub>O - 24.4% CaO - 6% P<sub>2</sub>O<sub>5</sub> composition (in weight percentage – wt%). Hench et al. discovered that this system, Bioglass® 45S5, had excellent biocompatibility, great ability to bond bone and that was able to degrade, being resorbed and replaced by natural tissue.<sup>21,24</sup> The bioactive mechanism will be discussed in detail later in this chapter, section 1.3.6.

Within the category of bioactive glasses, mesoporous bioactive glasses (MBGs) have recently gathered great attention within the scientific community for their highly ordered mesoporous structure, large surface area and pore volume, capable of enhancing the bioactive properties.<sup>25</sup>

### 1.3.2 Bioactive glasses

Glass is an amorphous material, lacking long-range order of atoms and periodic structure, which has received great importance in tissue engineering applications, among which bone regeneration. An attractive feature relates to the osteoinduction, the phenomenon by which undifferentiated cells are stimulated to develop into the bone-forming cell lineage (i.e. pre-osteoblasts). A second feature is osteoconduction, allowing bone growth on the surface of implants and inside their pores or channels. The last crucial requirement is osseointegration, defined as the direct anchorage of an implant to native tissue, guaranteed by the formation of bone-like tissue at the interface without the presence of a fibrous capsule.<sup>26</sup>

An example of a bioactive glass structure is shown in figure 5, where each type of atom has a specific function. In fact, glasses are usually produced with three types of inorganic oxides:

- a- Glass network formers: such as  $\text{SiO}_2$ ,  $\text{B}_2\text{O}_3$  and  $\text{P}_2\text{O}_5$ , creating the backbone of glass.
- b- Glass modifiers: usually alkaline or earth-alkaline oxides, such as  $\text{Na}_2\text{O}$ ,  $\text{CaO}$ ,  $\text{MgO}$  and  $\text{K}_2\text{O}$ , occupying random positions and modifying the structure adding more oxygen atoms (known as non-bridging oxygens).
- c- Glass intermediate: such as  $\text{Al}_2\text{O}_3$ ,  $\text{ZnO}$  and  $\text{TiO}_2$ , working either as network formers or modifiers.

Other additional elements include fining agents and colorants. As for fining agents (mostly arsenic and antimony, or  $\text{NaCl}$ ,  $\text{CaF}_2$  and  $\text{NaF}$ ), they can be found in small amount in the structure, thus not affecting the properties of the glass. During glass formation from the melt, contaminants tend to form gas bubbles, also referred to as “seeds”. The seeds affect the performance and quality of the glass, and efforts are made to remove them. The fining elements release gas to the existing bubbles, increasing their size and facilitating their ascension towards the top of the melt.<sup>27</sup> As for colorants, they are oxides belonging to 4f rare earth or 3d transition metal series, e.g. copper, vanadium, iron, manganese, gold and silver. The last two bring a colour in the glass by formation of colloids.<sup>24,28</sup>

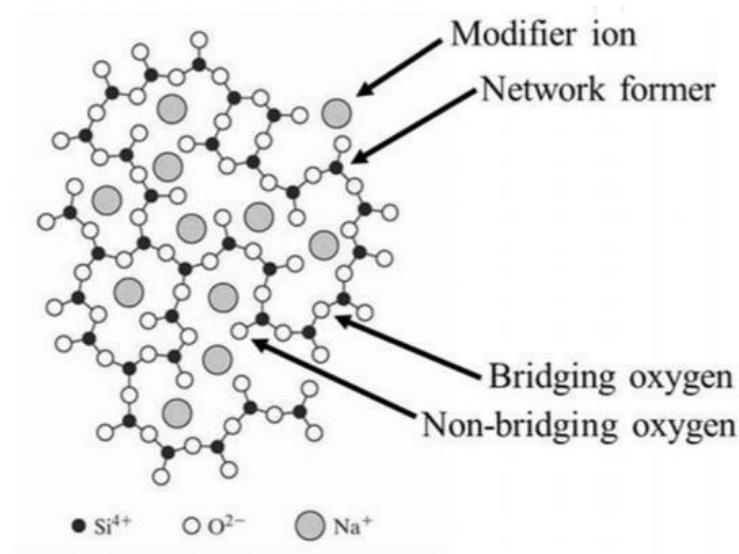


Figure 5: 2D presentation of random glass network modifiers and network formers.<sup>29</sup>

Silicate glasses are typically based on an amorphous network of  $\text{SiO}_4^{4-}$  tetrahedra, linked to each other at the oxygen centres. The modifier elements cause the opening of the network substituting bridging oxygens with non-bridging oxygens (they are not part of the tetrahedral unit). Several properties are affected by the presence of modifier elements, e.g. the type of chemical bonds (from covalent to ionic) and the glass melting temperature, which is usually reduced.<sup>29,30</sup>

Zachariassen et al.<sup>24</sup> explained why certain coordination numbers are favoured for the glass formation. He observed the tetrahedral network of silicate crystals and the random connections between the structural units; the 3D network is then extended casually over all possible directions with isotropic properties. The following four rules must be satisfied by a material melt aiming glass formation:

- oxygen can only be linked at two glass-forming atoms. It should not have higher coordination number as the oxygen-cation-oxide bond angles diminish;
- the cation coordination number should be small (between 3 and 4);
- the oxygen polyhedral share the corners and cannot be present at edges. This way, the structure is more open, and the cations are located far from each other;
- the network can be 3D, if at least 3 corner oxygens of a polyhedron are shared.

In 1969, Hench also proposed a diagram (Fig. 6), describing how the bond with bone may occur, depending on the glass composition, with a constant 6 wt% of  $P_2O_5$ , assumed enough for a glass to be bioactive.<sup>29</sup>

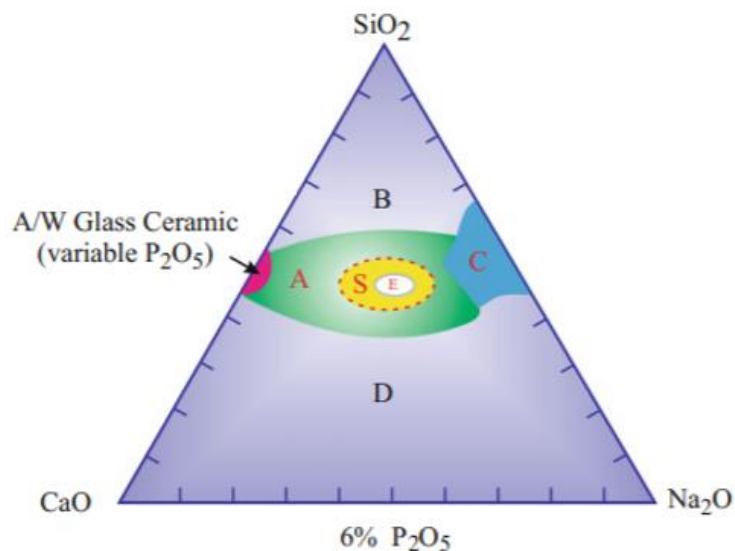


Figure 6: Phase diagram indicating the glass-forming region as proposed by Hench.<sup>24</sup>

Zone A glasses, in the middle of the triangle, form a bond with bone and therefore it is defined as the bioactive bone-bonding boundary. Glasses from region B act similarly to inert materials and, if implanted in the body, provoke the formation of a fibrous capsule at the implant-tissue interface. Glasses from region C, are resorbable but the kinetics of degradation are too fast, meaning the glass disappears within 30 days after implantation. Glasses from region D are non-glass forming so are not tested as implants. Glasses from region S are specialized in bonding with soft tissues, while the region E represents the Bioglass® composition.<sup>23</sup>

Taking as a reference figure 6, to obtain a bioactive glass there are some composition boundaries to be considered:

- SiO<sub>2</sub> content between 45 and 60 wt%;
- high Na<sub>2</sub>O and CaO content;
- high CaO/P<sub>2</sub>O<sub>5</sub> ratio.

The silica content is extremely important in the definition of the bioactive properties and ion dissolution rates. In fact, a silica content higher than 60 wt% decreases the dissolution rate of the ions from the surface, affecting the bioactivity, while a low silica content result in totally dissolvable monomeric SiO<sub>4</sub><sup>4-</sup> units. The CaO/P<sub>2</sub>O<sub>5</sub> ratio is fundamental in the tuning of ion release, greater with a high ratio, allowing the HCA layer to be formed in a short time.<sup>29</sup>

Those rules can be applied to the 45S5 Bioglass® produced by Hench through melt-quench method, but the technique is characterized by several drawbacks. Namely, some issues are related to the high working temperatures (greater than liquidus temperature of the composition) and the lack of microporous structure inside the materials leading to a low specific surface area.<sup>31</sup> To overcome those limitations, the sol-gel technique was developed, so that produced glasses could demonstrate a bioactive behaviour, whilst increasing the range of achievable compositions (up to 90 wt% of SiO<sub>2</sub>). Allied to this, these materials show an excellent degradation and resorption profiles. Sol-gel technique, however, has some limitations regarding the chemical compositions that can be produced and the need to remove water or solvent residuals.<sup>32</sup>

Desired parameters for bioactive glasses to function as a suitable biomaterial for regenerative medicine:<sup>21,24</sup>

- in contact with SBF, formation of HCA layer on the glass surface;
- suitable mechanical properties in order to prevent any structural failure being also comparable to those of native tissue;
- biocompatible, non-toxic and promoting cell adhesion;
- the architecture of devices produced from bioactive glasses must be porous, to promote cell proliferation, vascularization and diffusion of nutrients;
- absence of inflammatory response, immunogenicity or cytotoxicity;
- degradation in non-toxic products, easily resorbed or excreted from the body.

### 1.3.3 Mesoporous materials

Mesoporous materials have attracted attention in the last 20 years because of their large surface area, ordered structure, tuneable pore size and volume. Therefore, they can be applied as a versatile platform for bone regeneration applications and controlled release of drugs and growth factors. According to International Union of Pure and Applied Chemistry (IUPAC), the pore size classification, shown graphically in figure 7, can be depicted as follows:<sup>33</sup>

- Micropores (diameter below 2 nm);
- Mesopores (diameter in the range 2-50 nm);
- Macropores (diameter greater than 50 nm).

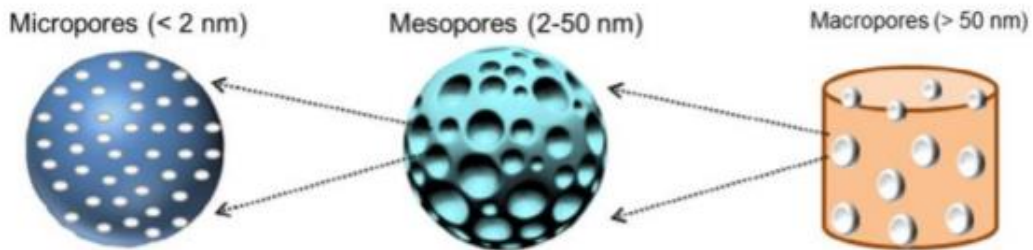


Figure 7: Pore size scales according to IUPAC terminology.<sup>31</sup>

The main characteristics of mesoporous materials are their good biocompatibility, low cytotoxicity and wide possibility for organic functionalization.<sup>33</sup> In particular, fundamental properties of mesoporous silica-based materials are:<sup>34</sup>

- two-dimensional or three-dimensional channel arrangements;
- regular pore morphology;
- surface area larger than 1000 m<sup>2</sup>/g;
- pore volume over 1 cm<sup>3</sup>/g;
- surface plentiful of silanol groups, so the material is easily functionalable

The mechanism of formation of mesoporous materials utilizes structure-directing agents (SDA), such as CTAB (cetyltrimethyl ammonium bromide), P123 (with composition PEO<sub>20</sub>-PPO<sub>70</sub>-PEO<sub>20</sub>) and F127 (with composition PEO<sub>106</sub>-PPO<sub>70</sub>-PEO<sub>106</sub>) which are able to self-assemble into micelles if they exhibit a concentration above the critical micelle concentration (cmc). The self-assembly process could be defined as “the spontaneous organization of materials through noncovalent interactions”, e.g. Van der Waals forces, hydrogen bonding and electrostatic forces. The SDA agents are amphiphilic molecules or polymers composed of both hydrophilic (characterized by great affinity with water) and hydrophobic (dissolving in polar solvent)

parts.<sup>33,35</sup> An amphiphilic molecule faces specific domains with the highest affinity for the solvent toward that solvent, shielding the other part that is not able to dissolve in that solvent. The morphology of the resulting aggregate depends on the ratio between the size of domains, on the molecular concentration and on the nature of solvent. Example of those morphologies are the lamellar, hexagonal, multiple or inversed micelles, presented in figure 8.<sup>35</sup>

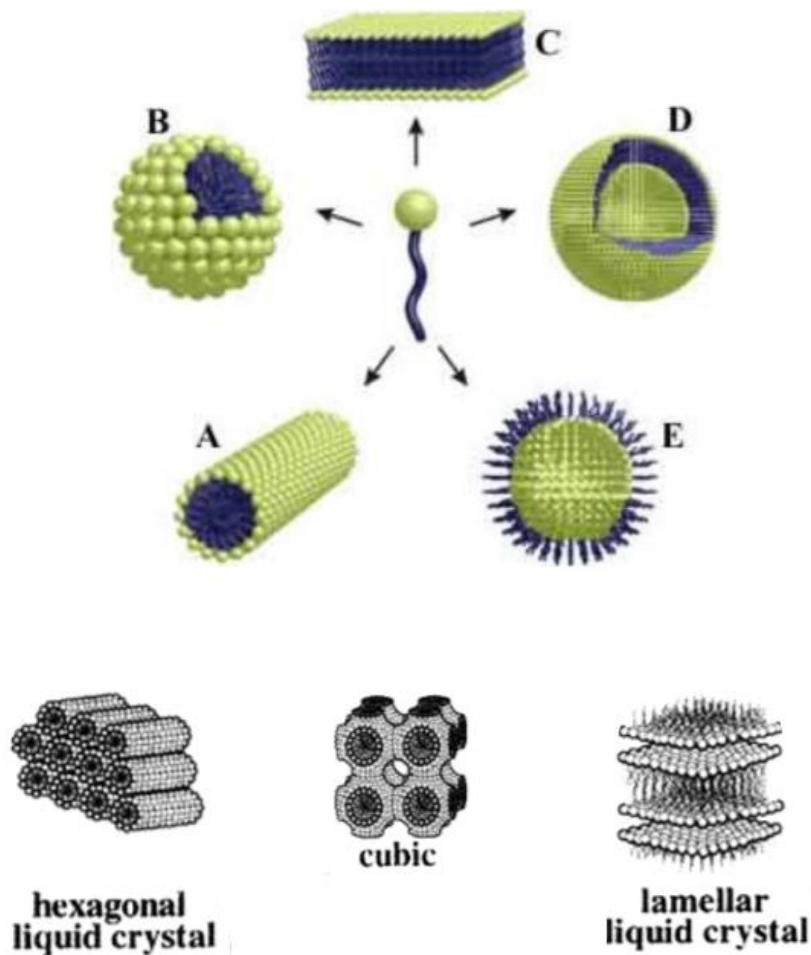


Figure 8: Representation of some arrangements for amphiphilic molecules.

The first mechanism of mesoporous silica production was developed by Mobil Oil Company in 1992, called Liquid Templating Mechanism, and was based on the electrostatic interactions of an aqueous micellar phase, positively charged, and silica precursors, especially TEOS or TMOS, negatively charged.<sup>36</sup>

There are two different mechanism that could explain the formation of those mesoporous structures (Fig. 9). The first mechanism consists on the true liquid-crystal templating (TLCT), (Fig. 9a), characterized by an extremely high concentration of surfactant that, under the same working conditions of temperature and pH, causes the formation of a lyotropic liquid-crystalline phase, avoiding the presence of the inorganic precursor

framework. The silica precursor is added after the liquid-crystalline phase is developed and condensate around that phase. Finally, the surfactant material is removed by calcination or extraction, thus forming the mesoporous network. The second mechanism, shown in figure 9b, is based on a lower concentration of surfactant molecules, where the silica precursor is added before the micellar structure formation. The organic/inorganic micellar structure is then developed because of the interaction between the two phases. Those micelles interact with each other creating a liquid-crystalline phase that, by removing the surfactant, are able to mature in the ultimate mesostructure.<sup>37</sup>

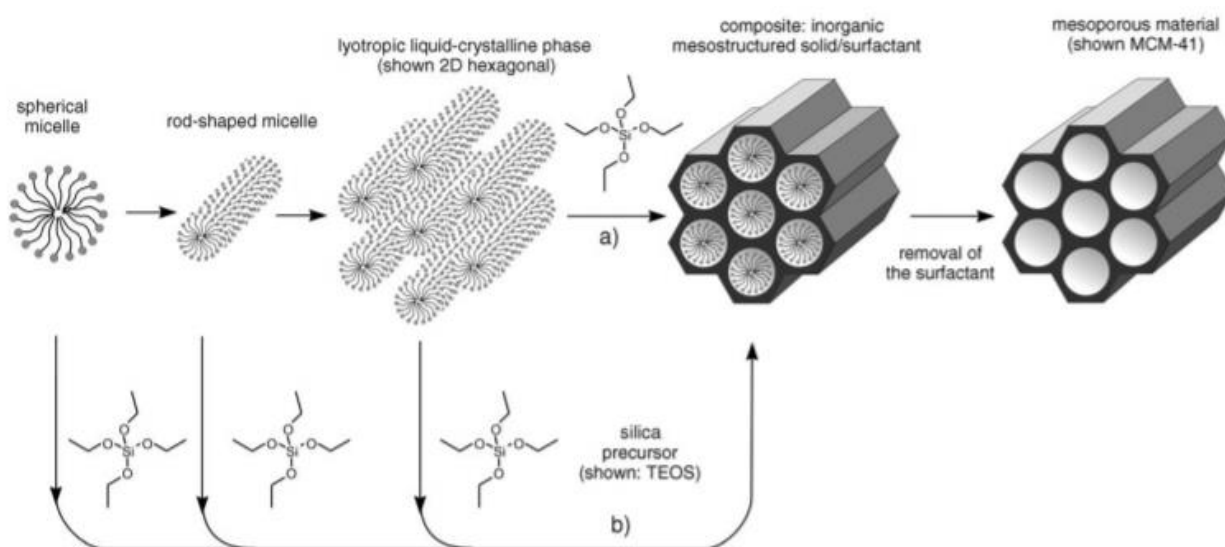


Figure 9: Formation of mesoporous materials by structure-directing agents: a) true liquid-crystal template mechanism, b) cooperative liquid-crystal template mechanism.<sup>37</sup>

The approaches previously described are based on cationic surfactants and anionic silicate species ( $S^+I^-$ ), but other interactions can be achieved changing the charge of the species ( $S^-I^+$ ) or by a combination of anionic/cationic surfactants and the matching inorganic species. Some examples are  $S^+X^-I^+$ , with X being a halide, or  $S^-M^+I^-$ , with M being an alkali metal ion. There are also two other pathways displaying a hydrogen bond, based on neutral ( $S^0$ ) or non-ionic surfactants ( $N^0$ ).<sup>36</sup>

Despite the functionalization strategies and the remarkable textural properties, because of the lack of CaO or  $P_2O_5$  components, the mesoporous silica materials are characterized by poor in vitro bioactivity. Led to the work of Zhao and Vallet-Regi et al.<sup>38</sup> where a new material is developed by combining the mesoporous silica and the sol-gel glass systems.<sup>34</sup>

### 1.3.4 Mesoporous bioactive glasses

The mesoporous bioactive glass (MBG) is characterized by highly ordered pores in the range of 2-50 nm, high surface area and pore volume. Those parameters can be efficiently tuned and easily controlled compared to the traditional sol-gel-based glasses.<sup>28</sup> The composition and textural properties from the two different families of glasses are summarized in the following table.

Table 3: Typical values of composition and textural properties of both families of glasses.<sup>34</sup>

Family of glass	Composition	SiO <sub>2</sub> content (mol%)	Surface area (m <sup>2</sup> /g)	Pore volume (cm <sup>3</sup> /g)
MBG	CaO-P <sub>2</sub> O <sub>5</sub> -SiO <sub>2</sub>	58-95	200-500	0.5-0.7
	CaO-SiO <sub>2</sub>			
Sol-gel glass	CaO-P <sub>2</sub> O <sub>5</sub> -SiO <sub>2</sub>	50-95	100-200	0.2-0.4
	CaO-SiO <sub>2</sub>			

Surface area and pore volume in MBG two times higher compared to sol-gel glasses with analogous composition, therefore displaying a faster *in vitro* bioactivity.

The ordered mesoporous structure can be confirmed by nitrogen adsorption isotherms, shown in figure 10, because of the presence of a type IV isotherm curve: the type H1 hysteresis loop is representative of cylindrical pores open at both ends.<sup>39</sup> The figure also displays the pore size distribution, tuneable by varying the templating agent and presenting narrow distribution. Both ordered structure and narrow pore distribution are crucial in tissue engineering applications for optimal drug delivery and bone scaffolds.<sup>34</sup> The structure-directing agents for MBG are the same discussed for silica materials: CTAB, F127 and P123. The resulting pores have different sizes, being the ones from CTAB generally smaller (2-3 nm) than P123- or F127-derived MBG (4-10 nm). Moreover, the P123 develops a two-dimensional hexagonal mesopore structure.<sup>33,40</sup>

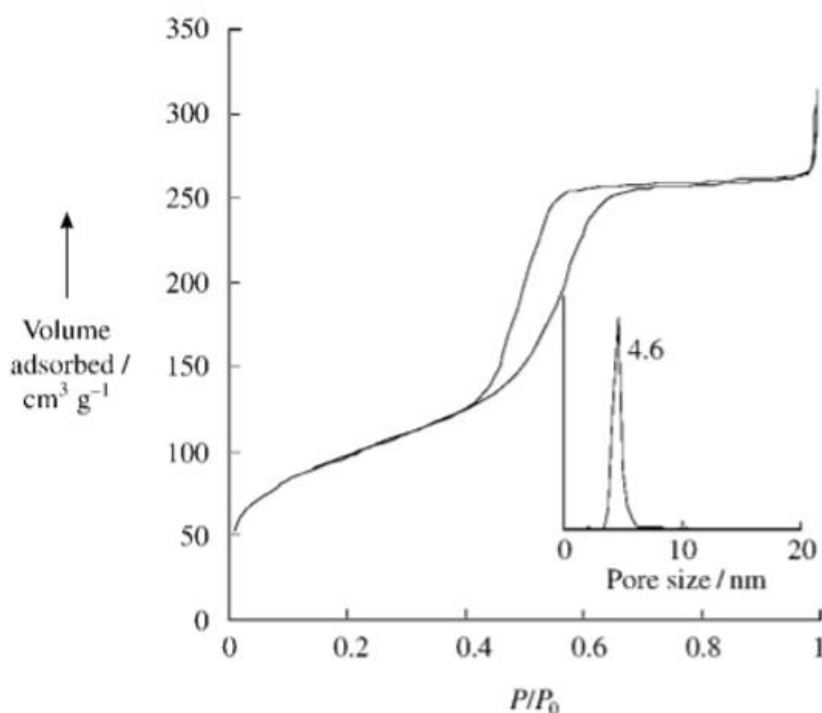


Figure 10:  $N_2$  adsorption-desorption isotherm of calcinated MBG in presence of P123 template. The inset shows a plot of the pore size distribution.

These structures also contain high amount of surface silanol groups that favour their bioactive response and their functionalization, in order to modulate the properties according to precise requirements.

It is also possible to modify the traditional composition of MBGs by adding small amounts of inorganic ions as cerium, gallium, zinc, strontium and many other in order to improve and guide their biological behaviour toward specific directions.<sup>34</sup> Strontium ion is a trace element present in human body, especially in liver, muscles, physiological fluids and within the mineralized part of bone. As strontium has ionic dimensions similar to calcium ion, various studies have been conducted to evaluate its substitution within mesoporous materials. It was established that  $Sr^{2+}$  containing MBGs display the ability to release both calcium and strontium ions, and have been widely utilized in case of bone disease.<sup>41</sup> Strontium plays a fundamental role in improving the stimulation of osteoblasts, increasing bone formation while inhibiting osteoclasts activity, and consequently bone resorption.<sup>42</sup> It was demonstrated that strontium can stimulate the proliferation and osteogenic differentiation through increased activity of alkaline phosphatase and angiogenic factor expression by human osteoblast-like cells (MG-63).<sup>43</sup> Moreover, it was verified that strontium containing MBGs display a faster bioactivity, allowing for a quicker production of apatite layer on their surfaces. This phenomenon can be explicated by the slightly greater ionic dimension of strontium, if compared to calcium ion. As a consequence, the forming network will increase its dimensions, then making the dissolution rate of the glass matrix faster. Because of the abovementioned properties, strontium can be assumed as a suitable candidate for treating osteoporosis.

### 1.3.5 Synthesis methods

The first mesoporous bioactive glass was synthesised by Yu et al. in 2004 by sol-gel method and supramolecular chemistry principles.<sup>33</sup> Other studies developed a new synthesis method, based on evaporation-induced self-assembly (EISA) process in near non-aqueous condition, that allowed the extensive use and develop of MBGs technology in medical applications. EISA process is based on the spontaneous organization of non-ionic surfactants through non-covalent interactions without external intervention.

The initial mixture is obtained by dissolving surfactant (CTAB, F127 or P123) and inorganic precursors (for example TEOS, TEP and  $\text{Ca}(\text{NO}_3)_2$ ) in a common medium, such as an ethanol-water system, and stirred for 12 hours. The solution is poured in a Petri dish and left for several days at ambient or slightly higher temperature allowing solvent evaporation. At the beginning of the evaporation process, the initial surfactant concentration is lower than the critical micellar concentration (cmc) required for the surfactant self-assembly. As the evaporation progresses, the surfactant concentration increases until reaching the cmc, then the surfactants assemble into micelles, with spherical or cylindrical structure. These micelles, bind the hydrolysed precursors in order to form the mesophase and once the mixture is dried and the surfactant is removed by calcination, a well-ordered structure will be obtained.<sup>33,34</sup>

Compared to the conventional bioactive glasses, MBG produced with this method have two unique characteristics. The first related to the mechanism for the generation of the mesopores. In sol-gel glasses the mesopores are generated from the random distribution of CaO within the silica network, while in MBG structures the self-assembly of surfactants give rise to uniform mesopores alongside ordered mesostructures. The second characteristic is associated with the compositional homogeneity of the framework. A microphase separation and heterogeneity are common in sol-gel glasses, while all the components are homogeneously distributed in the MBG structure.<sup>44</sup>

The process and the consequent result are influenced by several parameters including temperature, composition and time of aging and drying. CaO, other than guarantee a bioactive response, is a crucial parameter that influences the symmetry of the mesopore arrangement. When the content is decreased, the mesopore structure change from 2D-hexagonal to 3D-bicontinuous cubic. Moreover, the inverse variation can be observed when the aging temperature is increased.<sup>34</sup> As for the order of porosity, this parameter depend on surfactant chemistry (ionic, non-ionic, polymeric, etc.) and concentration, organic/inorganic phase volume ratio, temperature and pH of the solution.<sup>29</sup>

### 1.3.6 Bioactive properties

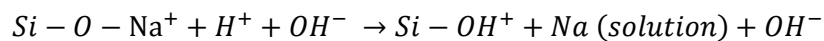
Chemical bonding with bone is the key for bioactive glasses success; because of the HCA layer formation, the bond with bone is stable and biocompatible, thus the whole device can be accepted by the body, avoiding adverse reactions. The process of device-bone bonding involves twelve reactions when the device is immersed in SBF or PBS. The reactions are summarized in figure 11, being acceptable for both conventional bioactive glasses and silica based mesoporous glasses.

	Reaction stage	Process occurring on bioactive glass surface	
↓ Log time / hours ↓	1		
	1 & 2	Formation of SiOH bonds and release of Si(OH) <sub>4</sub>	
	3	Polycondensation of SiOH + SiOH → Si-O-Si to form hydrated silica gel	
	2	4	Adsorption of amorphous Ca + PO <sub>4</sub> + CO <sub>3</sub>
	5	Crystallization of hydroxyl carbonate apatite (HCA)	
	10	6	Adsorption of biological moieties in HCA layer
	7	Action of macrophages	
	8	Attachment of osteoblast stem cells	
	20	9	Differentiation and proliferation of osteoblasts
	10	Generation of matrix	
	100	11	Crystallization of matrix
	12	Growth of bone	

Figure 11: Sequence of the interfacial reactions involved in forming the bond between tissue and bioactive glass, focusing on bone-tissue interface.<sup>40</sup>

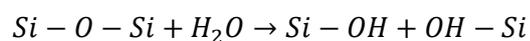
The stages are listed below.<sup>23,29</sup>

- 1- Leaching and formation of silanols:



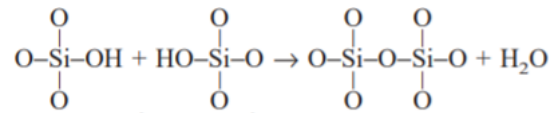
This stage is usually controlled by diffusion and displays a  $t^{-1/2}$  dependence.

- 2- Breaking of Si-O-Si bonds, release of Si(OH)<sub>4</sub> groups and formation of a considerable amount of silanol groups at the glass-solution interface:



This stage reaction is caused by the increase of pH (increasing released OH<sup>-</sup> groups).

3- Polycondensation of silanol groups forming hydrated silica-gel:



- 4- Adsorption of amorphous Ca – PO<sub>4</sub> – CO<sub>3</sub>, forming a CaO-P<sub>2</sub>O<sub>5</sub>-rich film on top of the silica layer, followed by its growth through the incorporation of soluble calcium and phosphate ions from solution.
- 5- Crystallization of HCA layer, by incorporation of hydrolysis and carbonate from solution.
- 6- Adsorption of biological moieties in HCA layer, able to activate the cellular differentiation process;
- 7- Action of macrophages, removing debris and thus freeing the surface;
- 8- Attachment of osteoblast stem cells;
- 9- Differentiation and proliferation of stem cells in osteoblasts;
- 10- Generation of extracellular matrix by osteoblasts;
- 11- Crystallization of extracellular matrix;
- 12- Growth of bone.

The reactions at the surface of bioactive glasses can be described as three general stages: leaching, dissolution and precipitation. Leaching is characterized by release of ions, because of the exchange between alkali or alkaline earth metal ions and hydrogen ions from the solution. This process occurs rapidly as the modifier ions, not being part of the glass network, leak easily when immersed in an aqueous solution. The ion exchange causes the increase in hydroxide ion concentration, thus increasing the basicity of the solution (pH > 7).

Network dissolution occurs simultaneously by breaking of the glass forming silica bonds by the attack of hydroxyl ions, releasing silicic acid. The glass composition has a great importance in this step and affects greatly the final bioactivity rate of the device. In fact, if silica content exceeds 55%, the rates of reaction steeply decrease, while if exceeding 60% the rate of reaction is sufficiently slow to consider the material as inert.<sup>3</sup> This could be explained with the increasing number of bridging oxygens, associated with the increased silica content, that can hold the network very strongly. It also occurs that hydrated silica undergoes polycondensation with neighbouring silanols to form silica-rich layer.

In the precipitation stage, both the calcium and phosphate ions released from the network and the ones existing in the solution form the calcium-phosphate-rich layer on the glass surface. Then the layer crystallizes to form HCA, by incorporation of carbonate ions from the solution. The rate of HCA formation and crystallization also affect the bioactivity of the implant because, if too slow, no bond forms and the material is no longer bioactive.<sup>29</sup> Moreover, the interfacial strength seems to be inversely dependent on the thickness of the bonding zone. For example, 45S5 Bioglass® has a bonding layer of 100 µm, characterized by low strength, whilst devices based on Apatite-Wollastonite (A/W) glass-ceramic have an interface of 20 µm and a high resistance to shear.<sup>23</sup>

The first five stages of bioactivity can be tested *in vitro* and are not dependent on the presence of the tissue. The remaining steps must be demonstrated by *in vivo* tests. The level of *in vivo* bioactivity depends on the rate of development of the interfacial bond between an implanted device and the surrounding native tissue. Hench et al. proposed a bioactivity index ( $I_B$ ), that vary from 0 to 12. A high value, comprised between 10 and 12, pictures soft tissue bonding.

$$I_B = 100/t_{0.5bb}$$

Where  $t_{0.5bb}$  is the time for more than 50% of the surface to be bonded to bone.<sup>45</sup>

Since MBGs have a higher surface area and pore volume, the HCA layer was demonstrated to be formed in simulated body fluid (SBF) after only 4 hours soaking.<sup>44</sup>

## 1.4 Hydroxyapatite

Hydroxyapatite (HA) is a calcium phosphate, with a base composition  $\text{Ca}_{10}(\text{PO}_4)_6(\text{OH})_2$ , which constitutes the mineralized phase of human bone and teeth. Synthetic HA is produced and highly desirable for its analogous morphology and composition, ideal for implantation purposes and bone regrowth.

In bone, biological HA consists of nonstoichiometric carbonated HA, which provides stiffness and is present in the form of plates or needles, depending on their width and length (40-60 nm long, 20 nm wide and 1.5-5 nm thick) that grow parallel to collagen fibres.<sup>46</sup>

Synthetic HA (Fig. 12) has a hexagonal structure, with cell dimensions as  $a=b=9.42 \text{ \AA}$  and  $c=6.88 \text{ \AA}$  and stoichiometric Ca/P ratio of 1.67.

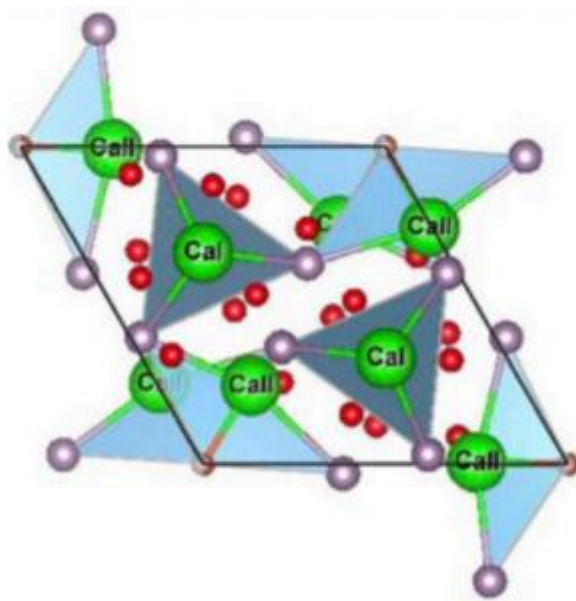


Figure 12: Crystal structure of stoichiometric hydroxyapatite.<sup>47</sup>

Despite the chemical similarities, synthetic HA has lower mechanical properties (Table 4) compared to bone apatite. The compressive strength of dense HA is higher than cortical bone, while having lower tensile strength and fracture toughness.<sup>48</sup> To overcome this deficit, several researches have tried to improve HA properties by using different sintering techniques or incorporating additives to enhance densification through grain boundary strengthening.<sup>46</sup>

*Table 4: Mechanical and thermal properties of dense HA.<sup>24,48</sup>*

<b>Property</b>	<b>Value</b>
Density (g/cm <sup>3</sup> )	3.1
UTS (MPa)	40-300
Compressive Strength (MPa)	300-900
Young's Modulus (GPa)	80-120
Fracture Toughness (MPa*m <sup>1/2</sup> )	0.6-1.0
Hardness (Knoop)	400-500
Poisson's Ratio	0.3
Melting point (°C)	1600-1700
Thermal conductivity (Wm <sup>-1</sup> K <sup>-1</sup> )	2.16
Thermal diffusivity (cm <sup>2</sup> s <sup>-1</sup> )	5.7 x 10 <sup>-3</sup>

Various techniques used to produce HA are sol-gel synthesis, solid-state reactions, hydrothermal reactions and chemical precipitation (Table 5). The sol-gel method has gained lot of interest for its versatility, described previously in section 1.3.2. For HA synthesis it is particularly interesting because it allows the mixing of the calcium and phosphorous precursors at a molecular level, improving chemical homogeneity, purity and reducing synthesis temperature. Solid-state reactions rely on the solid diffusion of ions amongst powder raw materials, therefore requiring high temperature processing to initiate the reaction.<sup>49</sup> Hydrothermal reactions are usually performed into autoclaves, where high temperatures and pressures can be reached.<sup>50</sup> Chemical precipitation is commonly used due to its simplicity and the ability to produce a wide variety of particles sizes and morphologies. The procedure is based on dropwise addition of phosphate solution into a stirring calcium solution.<sup>43</sup>

Table 5: Characteristic features of the HA production properties.<sup>49</sup>

Synthesis method	Processing time (</> 24hrs)	Reaction temperature (°C)	Particle size (µm)	Scalability
Sol-gel	>	37 – 85	> 0.001	Low
Solid-state	>	1050 – 1250	> 2.0	Medium
Hydrothermal reactions	<	150 – 400	> 0.05	Low
Chemical precipitation	>	25 – 85	> 0.1	high

HA can be produced with different degrees of crystallinity, based on the operated synthesis method. Regarding biomedical applications, it has been used as matrix for drug release, nanoparticles incorporated into matrices to form composite scaffolds, cements and mostly as a coating for implanted devices. HA is generally not utilized as a bulk material, because of its brittleness and relatively low mechanical strength.<sup>47</sup>

The application of a coating is useful for the modification of the surface as it can act against corrosion and transform an inert surface into a bioactive one. In fact, despite the possible issues concerning the use of metallic materials e.g. stress shielding, the combination of the mechanical properties from a metallic device and both bioactivity and biocompatibility from the ceramic coating, generate the most widely investigated traditional application for natural bone regrowth.<sup>48</sup>

Several techniques have been developed and applied to metallic materials (as titanium alloys or Co-Cr-Mo alloy), but also carbon implants, sintered ceramics like ZrO<sub>2</sub> and Al<sub>2</sub>O<sub>3</sub> or polymethyl methacrylate (PMMA). Table 6 summarizes some of the coating techniques using HA, highlighting their advantages and disadvantages.<sup>51</sup>

Table 6: Different coating techniques for HA.

Technique	Thickness	Advantages	Disadvantages
Dip coating	0.05-0.5 mm	Inexpensive, quick, coat complex substrates	High temperatures, thermal expansion mismatch
Sputter coating	0.02-1 $\mu\text{m}$	Uniform thickness on flat surfaces	Expensive, time consuming, cannot coat complex substrates
Pulsed laser deposition	0.05-5 $\mu\text{m}$	As for sputter coating	As for sputter coating
Hot pressing	0.2-2 mm	Dense coating	Cannot coat complex substrates
Electrophoretic deposition	0.1-2 mm	Uniform thickness, quick, coat complex substrates	Difficult to produce crack-free coatings, high sintering temperatures
Thermal spraying	30-200 $\mu\text{m}$	High deposition rates	High temperatures induce decomposition, rapid cooling produces amorphous coatings
Sol-gel	<1 $\mu\text{m}$	Coat complex substrates, low processing temperatures, cheap, coating very thin	Controlled atmosphere, expensive raw materials

Similar to traditional approaches, HA in tissue engineering strategies is not used as a bulk material because of the low fracture resistance and load strength. Instead, it can be used as coating over the device or as a reinforcement for the promotion of tissue growth and enhanced differentiation of mesenchymal stem cells.<sup>52</sup> It is also possible to change HA composition, e.g. ions substitution, and some of the possible substituting ions are already present in the body ( $\text{Mg}^{2+}$ ,  $\text{Zn}^{2+}$ ,  $\text{Sr}^{2+}$ ,  $\text{CO}_3^{2-}$ ,  $\text{Cl}^-$  and  $\text{F}^-$ ). The changes are mainly related with the microstructure, thermal stability, decomposition into other phases, grain size, crystal morphology, crystallinity and solubility, tuneable as the specific application requests.<sup>47</sup> It must also be noted that the hexagonal geometry is not significantly altered.<sup>43</sup> As previously stated in section 1.3.4, strontium is a widely utilized ion due to its ability in enhancing the osteoconductivity and inhibition of osteoclast activity.

Tissue engineering overcomes traditional medical applications as it comprehends a wide range of techniques allowing to design bioresorbable and biologically accurate scaffolds for natural bone regrowth. Those can be seeded with cells cultured from the target patient to produce a customized implant able to replace the damaged tissue. The device, once implanted, is a temporary template for the development of new tissue. Important characteristics to consider are biological, immunological and chemical properties of the intended material to control biocompatibility and bioresorbability of the final device. Morphology (pore size, porosity and pore interconnectivity) controls cell migration, adhesion and proliferation, while mechanical properties provide the necessary support. The scaffold can be produced with different techniques and with wide range of materials (synthetic or natural polymers, ceramics, biocomponents), based on the desired application but several times a single material cannot fulfil the totality of the requirements. Then, different strategies using both polymers and other phases can be developed to adapt the devices' properties according the desired application site. In case of bone regeneration, inorganic phases as the ones previously described are useful for drug loading and release of osteoinductive ions; they able to improve the body's response to the implanted device. Those phases are also required for an enhanced biocompatibility. Moreover, as bone is a stiff material, a polymeric matrix is usually utilized to mechanically sustain the new tissue regrowth. Polymers, the basic materials for scaffolds, are the focus of the next section.

## 1.5 Thermoplastic polymers for medical applications

Polymeric materials can be classified as thermoset or thermoplastic. The main difference resides in their molecular bonding, which dictates their behaviour under heating and cooling processes. Thermoset polymers are characterized by a crosslinked structure generated via changes in temperature or chemical reactions. The hardness and stiffness can be tailored by the chemical structures of the reactive components and the amount of crosslinking. A high crosslink density will result in a very stiff, hard and sometimes brittle material.<sup>53</sup> Thermoplastic polymers will soften upon heating and harden when cooled. The molecular chains in thermoplastic polymers are linear and associated with intermolecular forces that weaken rapidly when the temperature is increased. The melting yields to a viscous liquid and then the polymer can be shaped various times.<sup>54</sup>

Thermoplastic polymers are especially interesting for medical applications for their ability to be bioresorbable. The polymer can degrade over time, leading to the formation of low-molecular-weight substances, which are then reabsorbed into the body or blood plasma.<sup>53</sup>

The degradation process is extremely important in medical devices as it must be tuned with the regeneration of native tissue and, with attention to by-products of the degradation to avoid inflammation and cell death, so the material should be carefully selected according to the intended use. The biopolymers that will be further

described undergo hydrolytic degradation due to rupture of the ester group, therefore the degradation rate is dependent on water absorption and chemical environment.<sup>53</sup> Factors that can affect the hydrolytic degradation profile are water permeability and solubility, chemical composition, site of implantation, sterilization, molecular weight and molecular weight distribution.<sup>55</sup>

Some of the most widely used thermoplastic polymers are introduced in Table 7, including the most relevant mechanical properties, and the molecular structures presented on figure 13.

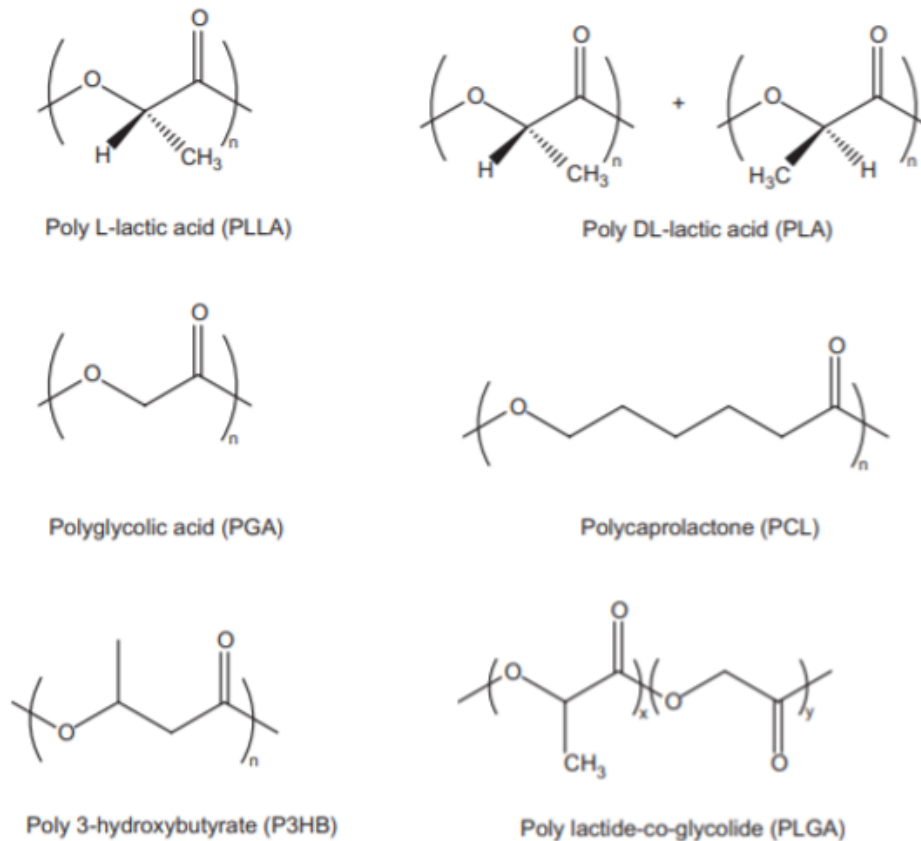


Figure 13: Structure of biopolymers.<sup>52</sup>

- Polyhydroxybutyrate (PHB)

Poly(3-hydroxybutyrate) (P3HB) is a highly crystalline, linear polyester of 3-hydroxybutyric acid, generated from a great variety of bacteria. The fermentation process is operated by the bacterium *Alcaligenes eutrophus* and lead to production of P3HB. The mechanical properties are enough for its implant use; it is stable under humid condition and degrades within two years.<sup>53</sup>

- Polyglycolic Acid or Polyglycolide (PGA) and Poly(L-glycolic acid) (PLGA)

PGA is obtained by the ring-opening polymerization of cyclic dimer of glycolic acid, is highly crystalline and therefore is insoluble in most organic solvents. It has a fast degradation rate, 50% with most mechanical properties lost within two weeks and 100% after four weeks. It is difficult to process because it degrades at its melting point.

PLGA is the success of the copolymerization of a L-lactide or D,L-lactide and a glycolide, with a tailored ratio based on the final product desired properties. For example, the degradation rate of the copolymer decreases when the lactide/glycolide ratio increases and the crystallinity increases according to the increase in lactide content. Namely, a copolymer 25/75 lactide/glycolide is amorphous while a copolymer 80/20 lactide/glycolide is semicrystalline. PLGA degrades quickly into non-toxic products, therefore is mainly used for biodegradable sutures, intravascular stents, drug delivery devices and as temporary scaffold for tissue and bone repair. The degradation mechanism of PLGA is bulk erosion, therefore more than 50% of its mechanical properties are lost within 2 months. This accelerate degradation process can lead to biocompatibility issues, probably caused by an excessive accumulation of lactic and glycolid acids.<sup>53,56,57</sup>

- Polycaprolactone (PCL)

PCL is synthesised by the ring-opening polymerization of  $\epsilon$ -caprolactone with a catalyst. PCL is crystalline and characterized by high flexibility, ductility and toughness, greater than the other biopolymers. Degradation time is about two years, is sustainable and environmentally friendly. Because of its intermediate thermal properties is often used as a plasticizer to improve the processing characteristics of rigid materials, as for example PVC.<sup>58</sup>

- Polylactic Acid (PLA) and Poly-L-lactic acid (PLLA)

PLA is a thermoplastic aliphatic polyester that can be totally degraded in aerobic or anaerobic environment from six months up to five years. The lactic acid is produced via the fermentation of glucose obtained from corn or other agricultural products. It has several attractive properties such as biocompatibility, high strength and stiffness. Its greatest drawback is the low impact strength.<sup>59</sup> There are two methods for the PLA production: ring-opening polymerization and direct polycondensation. Ring-opening polymerization involves the production of a lactide (lactic acid dimer) that is then purified, resulting in a polymer with controlled molecular weight. Direct polycondensation is based on the condensation reaction of lactic acid monomer, with the removal of water under heat and vacuum in a solvent. This method is highly inefficient as it demands a long time for processing, and the resultant molecular weight is lower compared to ring-opening.<sup>53,60,61</sup>

The lactic acid can be present in three stereoisomers (Fig. 14): optically active L-lactide, optically active D-lactide and non-optically active DL-lactide.

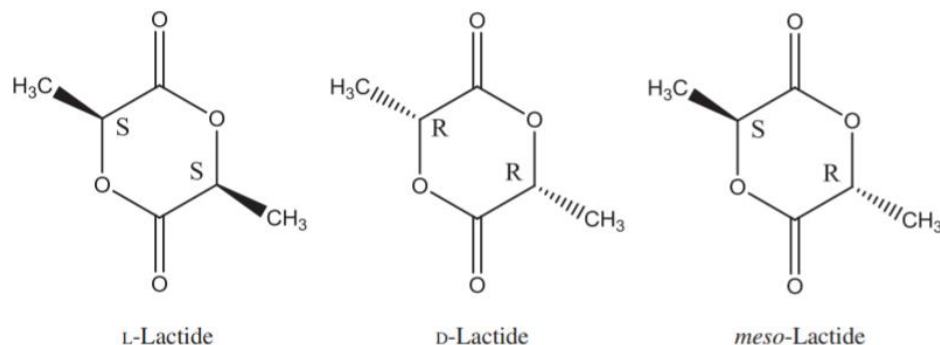


Figure 14: Stereoisomeric forms of lactide.<sup>56</sup>

PLA can be processed at temperatures of 185-190 °C. At these temperatures, it frequently occurs that chains can be disrupted, leading to loss of molecular weight and thermal degradation. The processing of the polymer at high temperatures for a prolonged period can favour the formation of lactide in the melt. This can reduce melt viscosity and elasticity, as well as the production of fumes. Therefore, PLA has a very narrow processing window. The mechanical properties of PLA depend on its optical purity and molecular weight. An increased molecular weight raises tensile strength, elastic modulus and lower the elongation at break.<sup>56</sup>

Poly-L-lactic acid (PLLA) is a transparent biopolymer, being totally amorphous or with a crystalline content up to 40%. Degradation time depends on the level of crystallinity, and for highly crystallized polymers degradation takes more than three years. Molecular weight, polymer architecture and crystallinity can affect some properties of PLLA.<sup>53</sup>

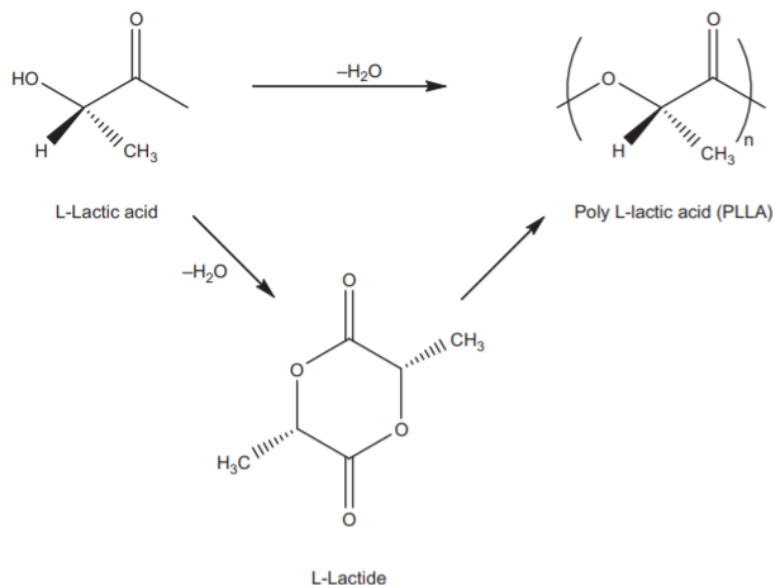


Figure 15: Production of poly-L-lactic acid (PLLA).<sup>52</sup>

According to the L and D-lactide content, the resulting polymer has different properties. In fact, polymers produced from L-lactide are semicrystalline, whilst D-lactide content above 15% leads to an amorphous structure (intermediate mechanical properties, degradation in less than two years). It must be noted that the crystallinity is not an intrinsic property of the material as it depends on thermal history and orientation of the chains.<sup>56</sup>

Table 7 presents some of the mechanical properties of the previously described polymers. It is foremost important to know about glass transition temperature and melting point. Glass transition temperature consists on a phase transition in which an amorphous polymer transforms from a glassy into a rubber state.<sup>62</sup> This phenomenon is not a phase transition, and the temperature that defines glass transition is always lower than melting temperature, if existing. Melting temperature can be defined when a semicrystalline polymer transforms from a solid to a liquid. In a liquid crystal, melting occurs when the solid 3D periodic structure collapses and transforms into a liquid-crystal phase in which the molecules have orientational order, but not long-range translational order. Both glass transition and melting temperatures strongly depends on the microscopic structure and the bonds linking the constituents. In fact, the values are usually higher in semicrystalline rather than amorphous structures, as the stronger bonds require higher energy to be disrupted. Another critical parameter is the processing temperature, generally equal or higher to the melting temperature to allow an easier processing of the material. As a consequence, semicrystalline polymers generally have higher melting and processing temperatures, as the bonds within their chains are stronger than those found in amorphous polymers. The higher working and melting temperatures among the analysed biopolymers belong to PLA, PLLA and PGA, being only the first one typically amorphous.

Flexural modulus can be defined as the stiffness that can be measured in the first or initial step of the bending process. Graphically, it is the slope of the initial straight portion in a stress-strain curve. It can be calculated as the ratio between the change in stress and the corresponding change in strain. According to ASTM D-970, for practical purposes, its value is usually lower than the tensile modulus.<sup>63</sup> The analysed polymers display similar values, except for PCL, whose flexural modulus is one order of magnitude lower than the others. Despite this limited performance, PCL exhibits a higher flexibility than the other biopolymers, with a degree of elongation at break two orders of magnitude higher.

Impact strength, or Izod impact, measures the energy required to break a specimen by striking a specific size bar with a pendulum. The test is usually referring to a notched specimen; in some cases, the specimen can be unnotched. The sample sizes and experimental conditions are defined by ISO 180:1993 and ASTM D-256.<sup>64</sup>

Based on a comparison among mechanical properties reported in Table 7, it can be said that PLLA has good mechanical properties for medical implants as screws, plates, pins and is usually used as feedstock material for Fused Filament Fabrication. It must be considered that those characteristics (e.g. crystallinity, melting point) are regulated by its molecular weight and polymer architecture. PLA can be presented with a different degree of crystallinity, meaning that its properties can vary. Commercially available P3HB has sufficient mechanical properties for being used as sutures, stents, drug delivery and tissue engineering scaffolds. The degradation rate is faster PLLA due to its amorphous structure. As the data of elongation at break suggests that this polymer is quite brittle, copolymers are developed to improve its flexibility and processability. PGA is usually displaying with high rates of crystallinity, and its tensile strength at break is intensely higher than the other polymers. PLGA displays a wide range of properties, because of the tuneable ratio between the components (L-lactide or D,L-lactide with glycolide). Usually, it is presented as an amorphous polymer, but its mechanical properties are not remarkable.

Table 7: Mechanical properties of some biopolymers.<sup>32</sup>

<b>Property</b>	<b>Unit</b>	<b>P3HB</b>	<b>PGA</b>	<b>PLGA</b>	<b>PCL</b>	<b>PLA</b>	<b>PLLA</b>
Density	g/cc	1.25	1.5-1.7	0.75	0.8-1.1	1.26	1.25
Glass transition temperature	°C	1	35-40	45-50	-60	55-60	50-55
Melting point	°C	170-180	224-230	70-80	60	173-178	170-180
Tensile strength at break	MPa	36	890	41-55	5.17-29.0	29-50	40-70
Elongation at break	%	3	30	3-10	650-800	6	6-12
Flexural modulus	GPa	1-3	5-7	1-3	0.2-0.5	1-3	2-4
Impact strength, notched, 23 °C	J/m	35-60	-	-	120-375	15-135	10-15
Processing temperature	°C	180-190	220-240	80-100	80-100	180-200	180-190
Degradation rate	Months	2-18	0.5-1.5	1-6	24	<24	18-60
Morphology		C	C	A	C	A	C

N.B: A = amorphous; C = crystalline.

## 2 – Scaffold for bone tissue engineering

The constant ageing of population can be associated with an increased need for new approaches in order to repair damaged tissues. The most widely utilized techniques are based on bone grafts and metallic devices. Bone grafts can derive from the patient's body (autografts), from a cadaver of the same species (allograft), or from a cadaver of a different species (xenograft).<sup>4</sup> The autografts have the crucial advantages of excellent biologic and biocompatibility properties, nevertheless there are several limitations such as donor site morbidity and the limited volume available.<sup>65</sup> In orthopaedics, metals can be used as fixation devices, screws, plates, partial and total joint replacement prosthesis. Despite the high mechanical properties of those devices, several problems occur as stress shielding, bone resorption and the lack of osteoinductive behaviour. Therefore, the device will remain for the lifetime within the patient's body.

To overcome the limitation of the conventional treatments based on biomaterial implantation, tissue engineering (TE) was developed. TE has the potential to produce immunologically tolerant artificial tissue and organ, avoiding additional therapies and therefore making it a cost-effective treatment in the long term.<sup>66</sup> TE is focused on the use of materials and cells, for the development of devices that can substitute the defect structurally and functionally.<sup>67</sup> These devices can reduce medical costs and serve as a carriers for drugs, bioactive proteins and cells. In bone regeneration applications, scaffolds generally serve as mechanical support for the growing tissue; they can also release the loaded drugs and therapeutic and/or osteoinductive ions that can be incorporated. As a single material is not able to fulfil all the requirements, e.g. mechanical properties, degradation profile and bioactive properties, composite formulations are investigated to better embrace the beneficial properties of the single materials or phases.

The focus of this work is the development of a hybrid formulation based on polymeric matrix, containing inorganic phases such as mesoporous bioactive glasses or hydroxyapatite. Both of the inorganic phases contain strontium ions ( $\text{Sr}^{2+}$ ), well known for the pro-osteogenic and anti-clastogenic properties and thus able to stimulate bone regeneration in compromised clinical context, such as osteoporosis. The main advantage of the composite formulation is, as mentioned before, the integration of the single component properties. The composite is extruded in a filament that will be then printed using additive manufacturing (AM) technologies. The materials' characterization has guided the best combination among the tested ones and provided the information about its printability, in view of the device production by extrusion printing. AM technologies allow for enhanced design freedom in term of geometry and complexity, permitting to increase the range of applications and versatility of the materials typically used in TE approaches (e.g. polymers and ceramics).

The chapter is focused on the description of the main technologies to produce polymer-based scaffold, alongside a brief report on surface functionalization strategies. Amongst traditional manufacturing techniques, it is introduced AM as new way to produce 3D-bespoke devices, with a high versatility in terms of material selection and design freedom.

## 2.1 Scaffold for bone tissue engineering

The scaffold technology is a combination of biological, chemical and engineering principles. The main objective of a scaffold is “provide a framework and initial support for the cells to attach, proliferate and differentiate, and form an extracellular matrix”.<sup>68</sup>

The most important requirements are:<sup>4,69</sup>

- The surface should be biocompatible to allow cell adhesion and growth. Biocompatibility is related to the material’s ability in making cells able to achieve suitable responses in the biological environment.
- The scaffold must be biodegradable. The degradation products must not rise an inflammatory reaction or toxicity and should be totally absorbed.
- The scaffold must have a porous structure to guarantee cell seeding, diffusion and permit nutrient supply. The percentage of porosity affects the number of cells that can be hosted and the structural strength of scaffold; the pore diameter can be altered based on cell dimensions. Moreover, the pore orientation can be adjusted with various techniques and induce the cell growth in a specific direction.
- The degradation profile of the scaffold must be tuned to native tissue growth, to assure its formation in the native shape. In fact, if the degradation is too slow interferes with tissue remodelling while, if it is too rapid, does not sustain the device throughout the healing process.
- The scaffold should provide mechanical support, to withstand the body stresses until the cells have synthesised their own extracellular matrix. Different synthetic polymers can be blended to obtain specific mechanical requests; instead, natural polymers can be reinforced and strengthened by the addition of mineral phases, synthetic polymers by cross-linking.

As for bone, the mechanical properties are listed in Table 8.

*Table 8: Summary of the mechanical properties of human bone.<sup>70</sup>*

<b>Bone</b>	<b>Compressive strength (Mpa)</b>	<b>Flexural strength (Mpa)</b>	<b>Tensile strength (MPa)</b>	<b>Modulus (GPa)</b>	<b>Fracture toughness (MPa*m<sup>1/2</sup>)</b>	<b>Porosity (%)</b>
Cortical	100-150	135-193	50-151	10-20	2-12	5-10
Trabecular	2-12	10-20	1-5	0.1-5	0.1-0.8	50-90

The scaffold elastic modulus should be ideally comparable to the substituting tissues to promote load transfer and limit stress shielding. Indeed, if there is a large mismatch between the elastic moduli of tissue and scaffold, the stresses are not correctly transferred to bone tissue. Bone needs to be under continuous tensile load stimulus to remain healthy, otherwise its density will be reduced. This condition was described by Wolff’s Law: “Every change in the form and function of bone or their

function alone is followed by certain definite changes in their internal architecture, and equally definite alteration in their external conformation, in accordance with mathematical laws”.<sup>71</sup> This law states that mechanics can cause changes in bone architecture, even without saying how. In the process known as “bone remodelling”, bone density decreases and causes the tissue weakening. The process could lastly lead to bone fracture.<sup>72</sup>

Several difficulties arise from dealing with those requirements, as some of them are contradictory. Namely, the scaffold must be bioresorbable, but over time the degradation hinders mechanical properties and increases fragility, placing difficulty in tuning the device degradation and new tissue growth rates.<sup>73</sup>

### 2.1.1 Polymeric scaffold production

Some of the technologies for scaffolds production from polymeric materials are:

- Solvent casting and particulate leaching. The method is based on the dissolution of the polymer into a suitable organic solvent and then cast into a mould filled with porogen particles (Fig. 16). The porogen could be inorganic salts as NaCl, crystals of saccharose or spheres of paraffin and their dimension will affect the size of the pores. The solvent can fully evaporate and finally the structure is immersed in a bath of a liquid in order to remove the porogen through dissolution. For example, water can be used to remove sodium chloride and saccharose while an aliphatic solvent (hexane) can be used to remove paraffin. The porosity can be controlled through the salt/polymer ratio; moreover, the technique is highly time consuming and certain parameters as pore shape and interconnectivity are not fully controlled. It should be also noted that some of the solvents are toxic and their removal is challenging.<sup>74,75</sup>

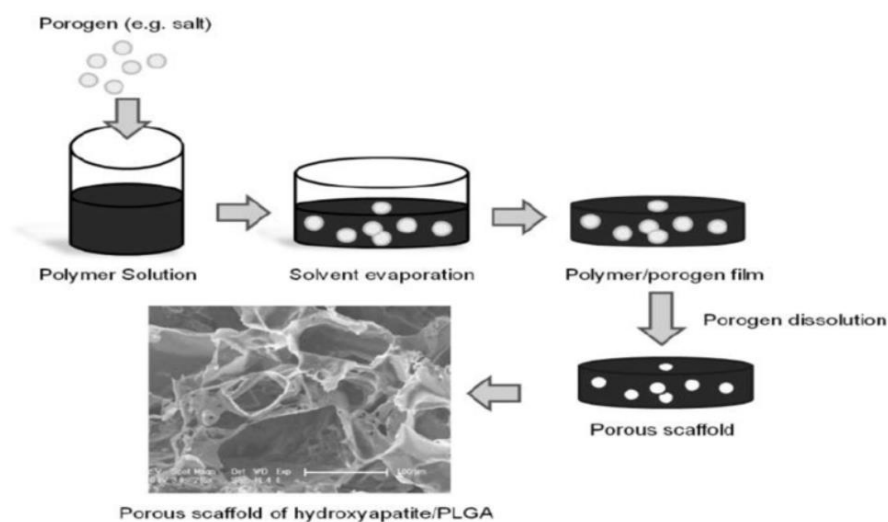


Figure 16: Schematic representation of solvent casting technique.<sup>76</sup>

- Phase separation. Is a technique that can be divided into three main categories depending on the parameters that induce demixing. A) temperature induced phase separation (TIPS): based on changes in the temperature at the interface of the polymer solution, heat will be exchanged and demixing will be induced. B) diffusion induced phase separation (DIPS): contacting a polymer solution with a vapour or a liquid (a non-solvent), diffusional mass exchange will lead to a change in the local composition of the polymer film and demixing can be induced. C) reaction induced phase separation (RIPS): the polymer solution is put into contact with a bath inducing precipitation though either changes in pH or the presence of a crosslinking reagent (covalent or ionic crosslinking).<sup>69</sup>
- Gas foaming. This technique is based in high pressure CO<sub>2</sub> gas dispersed throughout a polymer mixed with a porogen (e.g. sodium chloride), until saturation. The solubility of CO<sub>2</sub> is decreased rapidly until the atmospheric level is reached resulting in nucleation and growth of gas bubbles. After the completion of foaming process, the porogen is removed and a highly interconnected pore structure is created (depending on the amount of gas dissolved in the polymer). The advantages of this technique are that the process does not require high temperatures nor the use of organic solvents.<sup>74</sup>
- Emulsification/Freeze-drying. The main physical mechanism is the sublimation, that is the shift from a solid phase directly into a gas. The polymer is dissolved into a suitable solvent, then water is added to the polymeric solution in order to obtain an emulsion. Before the two phases can separate, the emulsion is cast into a mould and quickly frozen by immersion in liquid nitrogen. The frozen emulsion is finally freeze-dried to remove the dispersed water and the solvent, thus leaving only a solidified porous polymeric structure. The porosity can be controlled by varying freezing time and annealing stage. A crucial advantage is that the technique does not require a porogen and consequently its removal is not a problem, while the main difficulty is associated with structural stability and adequate mechanical properties. The pore size is also often relatively small and irregular.<sup>74</sup>

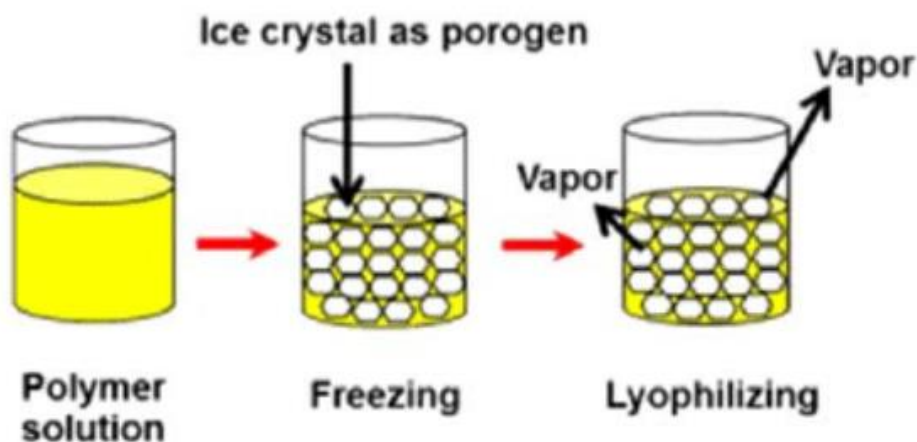


Figure 17: Schematic representation of freeze-drying process.<sup>77</sup>

To compare the previous techniques, Table 9 underlines the different pore sizes and rate of porosity achievable. Described is also the type of attainable microarchitecture and the rate of interconnectivity.<sup>75,78</sup>

*Table 9: Geometrical factors and architecture of some scaffold fabrication technologies.*

<b>Fabrication Technology</b>	<b>Pore size (µm)</b>	<b>Porosity (%)</b>	<b>Architecture</b>
Solvent casting/particulate leaching	30-300	20-50	Spherical pores, salt particles remain in matrix
Thermally induced phase separation	<200	<97	High volume of inter-connected micropore structure
Gas foaming	100	80-90	Spherical pores, low interconnectivity
Emulsion freeze-drying	<200	<97	High volume of inter-connected micropore structure

Other techniques are:

- Spinning methods. There are different approaches based on the physical condition of the polymer. A) melt spinning utilizes a fuse polymer extruded through a die of the desired shape. The advantages are the use of wide variety of polymeric materials, low energy consumption and high mechanical, optical and electrical properties. B) and C) dry spinning and wet spinning utilize polymer solutions and their extrusion through a die of the desired shape. The solvent is removed through evaporation through hot air or inert gas on the polymer (for dry spinning); as for wet spinning, the fibre is immersed in a viscous coagulation bath containing a non-solvent miscible with the solvent but not with the polymer in order to cause polymer's precipitation.<sup>79</sup> It exists one last approach based on spinning process that is the most developed and widely used, it will be described next.
- Electrospinning. Unlike the other techniques, electrospinning can produce fibres with nanometric dimensions, having large surface area and superior mechanical properties. The technique is simple and cost-effective, producing scaffolds with an inter-connected pore structure and quite easily controllable fibre diameters. The process (Fig. 18) is based on the presence of an electric field applied between two electrodes, one placed in the polymeric solution and the other placed in the collector. The polymeric solution is held at a needle tip by surface tension; the electrostatic force opposes the surface

tension, causing the initiation of a jet. As the jet travels, the solvent evaporates, and the nanofibers are deposited in the collector.

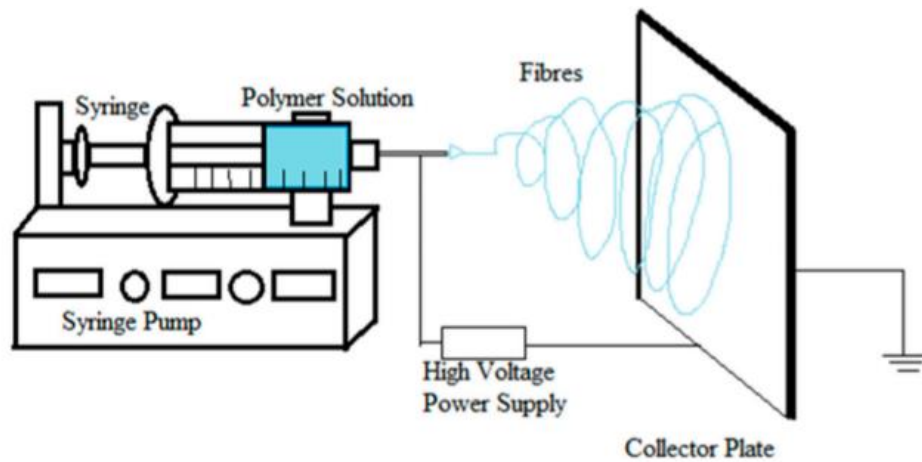


Figure 18: Schematic of electrospinning system.<sup>79</sup>

There are several types of nozzles and collectors, allowing the development of fibres with various characteristics. The nozzles can be a single (spinning a simple polymer or a blend) as presented in figure 19, coaxial (with two different polymer solutions, where the small capillary is within the larger one) or multi-jet (where several capillaries are arranged in circular geometry, to increase the high-throughput and industrial commercialization). As for the collectors, widely used are stationary plated, aluminium foils and rotating plates. The stationary plate permit to obtain random structures, while the rotating plate can give the fibres a certain directionality.<sup>79</sup> Moreover, also tubular structures can be obtained through a rotating cylindrical mandrel.<sup>80</sup>

Table 10 represents the most crucial parameters that affect the resulting fibres. They can be divided into process parameters (based for example on electric field or flow rate) and solution parameters (concentration, conductivity, etc.).<sup>69</sup>

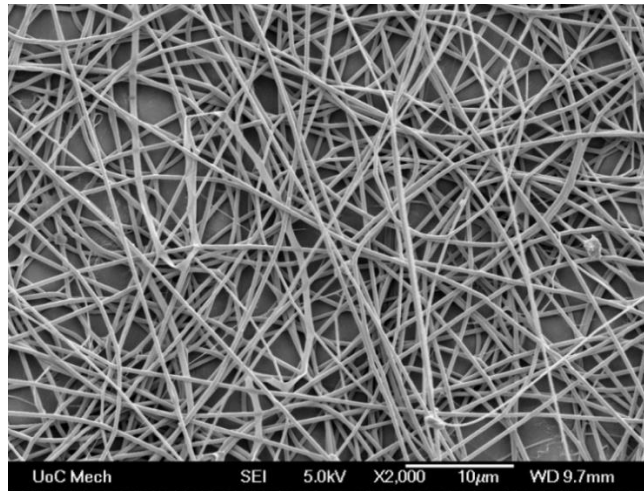


Figure 19: Example of fibres produced from electrospinning.

Table 10: Fibre diameter behaviour as some process or solution parameters change.

Parameter	Fibre morphology
↑ electric field	↓ fibre diameter
↑ volumetric flow rate	↑ fibre diameter
↑ distance nozzle-collector	↓ fibre diameter
↑ polymer concentration	↑ fibre diameter
↑ solution conductivity	↓ fibre diameter
↑ solvent volatility	Fibres with micro/nanopores due to fast solvent evaporation

## 2.2 Scaffold functionalisation strategies

Scaffold surface modification can be useful in order to improve bone/implant contact and, through appropriate signalling, increasing healing speed as well as reducing loosening. A common strategy for polymeric surface modification is the material coating via physical adsorption. The adsorbed layer can be easily removed, especially in case of change in solution pH or because of high shear stresses. Graft polymerization guarantee the desired monomer to be strongly attached to the polymeric surface with strong bonds, such as covalent bonds. An easy approach is introducing functional groups on the surface for chemical reactions between the substrate and the grafted layer.<sup>81</sup> Several components of the extracellular matrix like Type I collagen, chondroitin sulphate (CS), protein containing RGD peptide or growth factors can be grafted and interact with bone cells via integrins or other specific cell surface receptors. Then, the link can directly or indirectly affect migration, cell adhesion, proliferation and differentiation.<sup>82</sup>

Growth factors (GF) are polypeptides that act locally as modulators of cellular activity and are widely used in bone repair, especially bone morphogenetic proteins (MBPs), fibroblast growth factors (FGFs), insulin-like growth factors (IGFs) and vascular endothelial growth factor (VEGF). Those factors are usually stored in the extracellular matrix and have different range of action. In fact, they can be autocrine (GFs affecting cells of the same origin or phenotype), paracrine (affecting neighbouring cells with a different phenotype) or endocrine (affecting cells located in distant sites). GFs bind to target cell receptors and induce an intracellular signal transduction reaching the nucleus and consequently determining a biological response. Some examples are given in Table 11.<sup>83</sup>

*Table 11: Growth factors acting on bone repair.*<sup>83</sup>

<b>GF</b>	<b>Biologic effect</b>	<b>Action on bone</b>
MBP	Chondro-osteogenesis, osteoinduction (MBP-2)	Migration of osteoprogenitors, induction of proliferation, differentiation and matrix synthesis
FGF	Angiogenesis, proliferation of fibroblast	Osteoblast proliferation and differentiation, inhibition of apoptosis of immature osteoblasts, bone resorption
IGF	Regulation of growth hormone effects	Osteoblast proliferation and bone matrix synthesis, bone resorption
VEGF	angiogenesis	Conversion of cartilage into bone, osteoblast proliferation and differentiation

Several working strategies can be developed based on growth factors:<sup>69</sup>

- 1- Release systems: the matrix of the device is loaded with GF, then released gradually;
- 2- Cellular therapy: the matrix is implanted with cells, then able to produce and release the needed growth factors in order to direct the body's reaction.
- 3- Gene therapy: genetic modification of the cells implanted in the device in order to make them able to produce and release specific growth factors.

The release system can be affected by some parameters, as for example GF solubility and diffusion coefficient in the physiological medium, quantity of GF loaded in the device and distance that the load needs to cover. The peptides have a single motif, thus are specific towards a precise cellular receptor; the proteins have plenty of sequences, so the selectivity decreases.

## 2.3 Additive manufacturing (AM) techniques: printing of bone scaffolds

The techniques for scaffold production previously listed have some common drawbacks, as for example their lack of precise control of pore size, phase distribution, bulk interconnectivity and irregularities in the three-dimensional scaffold architecture.<sup>84</sup> To overcome those limitations new technologies were developed, based on AM technologies.<sup>4</sup> According to ASTM definition, additive manufacturing is “a process of joining materials to make objects from 3D model data, usually layer upon layer, as opposed to subtractive manufacturing methodologies”.<sup>85</sup> The additive nature of those technologies ensures minimal waste of expensive materials, offering a great control over the architecture, reproducibility, scale-up and standardization. Conventional methods require a careful and detailed analysis of the geometry to determine the precise order in which the parts need to be fabricated, assembled and what are the additional desirable fixtures to complete the part. In those cases, multiple production stages are required and, when the complexity rises, the time for manufacture significantly increases. AM, instead, requires dimensional details about the part and the necessary materials. Therefore, those technologies can effectively predict the amount of time needed for the model fabrication, despite any possible change in the design. Additionally, the number of processes and their complexity critically decreases.<sup>86</sup>

AM techniques are emerging mould-less fabrication technologies using layer-wise manufacturing strategies to create scaffolds with customised shape and controlled internal architecture. For medical devices, the procedure utilizes the patient's images acquired by computer tomography (CT) data or magnetic resonance imaging (MRI), then converted in a 3D model using computer-aided design (CAD) software.<sup>73</sup> MRI utilises magnetic fields and pulsating radio waves to obtain detailed 2D images of organs and soft tissues; those are then stacked to create a 3D image of the scanned zone. The CT, or computerized axial tomography, is based on X-rays to produce the image of the scanned area. For bone applications, CT scans are preferred as more defined.<sup>87</sup>

CAD is a crucial part of the workflow because it determines the structural properties of the model and guarantees the anatomical conformity, indispensable role for a proper integration in the native tissue. The CAD data is cross sectioned in thin layers. The thinner the layer the higher is the resolution of the process increasing the accuracy of the resulting part geometry. Differences in AM machines are the used materials, how the layers are created and how are linked to one another. Those differences will affect the quality of the part, which material is used and resultant mechanical properties. A major benefit in using CAD design is the easiness and cheapness in the implementation of changes.<sup>86</sup> CAD can be paired with other software providing information regarding stress simulations or topology optimization known as finite element analysis (FEA).<sup>88,89</sup> After this, the basic key steps are: input data (import of the STL file created from a CAD file), part preparation (where support structures and the machine parameters are specified), layer preparation (where the STL model is layered and translated into the machine language) and finally laser scanning.

In various processes the printed ink can be “bioink”, comprising viable cells and biological substances. Those incorporations can help the cell migration and seeding, ensuring their proliferation, differentiation and ECM deposition. Some studies have already developed scaffolds with viable cells in the polymeric structure; it was proven that under certain conditions the cells survived the printing step and showed good ECM development both *in vitro* and *in vivo* experiments.<sup>90</sup> Other studies created scaffolds with the presence of growth factors and/or drug. Their presence helped bone growth and tuned a more controlled drug delivery, reducing the initial burst release and limiting the incorporated drug dose.<sup>88</sup> The incorporation of living cells and biological substances still needs research as the process is complex and various parameters must be selected according to cells’ sensibility (e.g. low temperatures and shear stresses are preferred, while light or UV beam could affect cell viability).

A description of the most frequently adopted AM techniques is presented.<sup>73,91,87</sup>

**Stereolithography (SLA)** is a technology based on the cure of one layer of material over the previous one. SLA operates via photopolymerization, which are based on the use of liquid, radiation-curable resins or photopolymers as primary materials. Usually the utilized radiation is in the ultraviolet range of wavelength, and in some applications in the visible light range. Because of the radiation, the primary material undergoes a chemical reaction and becomes solid.

The three possible configurations are:<sup>86</sup>

- 1- Vector scan, the typical machine commercially available. The laser selectively solidifies a photopolymer resin through the laser, tracing the 2D part contour in a vat. The base platform is then lowered and the vat surface recoated; consequently, the laser can trace the next contour. When the part is complete, it must be cleaned by the material not cured by laser, post-cured and finished.
- 2- Mask projections (MP), where the laser irradiates the entire layer. The main advantage of MP is speed, higher than the other configurations. Some MP machines build parts upside down and the benefit of this approach is threefold the velocity. There is no need for recoating mechanism and the traditional vat can be substituted with a supply-on-demand material feed system. Moreover, the top irradiated surface is a flat window, instead of a free surface, making the process more precise.
- 3- Two-photon, high-resolution point-by-point approaches. Photopolymerization occurs at the intersection of two scanning laser beams because the photoinitiator requires two photons to start the polymerization. The resolution increases, but only in the centre of the beam, where the irradiance is high enough to provide the photon density required for striking the same photoinitiator molecule.

The main advantages of this technology are the increased accuracy of the produced device and surface quality. Moreover, the technology offers great flexibility, supporting various machine configurations and size scales. The disadvantages are the photopolymers, since the chemistries are based only on acrylates and epoxies for commercial products. Other materials have been studied for this application but have not succeeded on the market because of the lower quality, durability and impact strength.<sup>86,73</sup>

**Selective laser sintering (SLS)** was the first commercialized powder bed fusion (PBF) technology. PBF processes have some common characteristics as at least one thermal source for powder particle fusion, a method for the selective control of powder fusion, mechanism for adding and smoothing powder layers. The most utilized thermal source is laser, different for polymeric, metallic, ceramic or composite sintering. Thermoplastic polymers are suitable for this kind of process because of their low melting temperature and low thermal conductivities. As for metals, there are various types of steels (titanium and alloys, nickel-based and aluminium alloys). As for ceramics, commercially available are aluminium and titanium oxides. The process takes place in a chamber filled with nitrogen to minimize oxidation and degradation reactions. The deposited powder is maintained at high temperatures, sometimes using resistive heaters. Essential reasons for high temperature powders are to minimize the laser power and to prevent the part warping due to nonuniform thermal expansion and contraction. Once the powder layer is deposited and heated, a focused CO<sub>2</sub> laser beam lights the powder and moves according CAD design. In this technology supporting material is not needed because the necessary support is given by unsintered material. After the completion of the part, a cool-down period is required to allow the device to homogeneously reach low temperatures. Only after the object cool-down, it can be exposed to external temperature and atmosphere. If this happens before, the powder can degrade because of the oxygen or the part shrink because of thermal contraction. Finally, powder bed is removed, and the part is cleaned. This technique, as well as SL, can be performed in two ways, i.e. bottom-up and top-down, figure 20.<sup>86</sup>

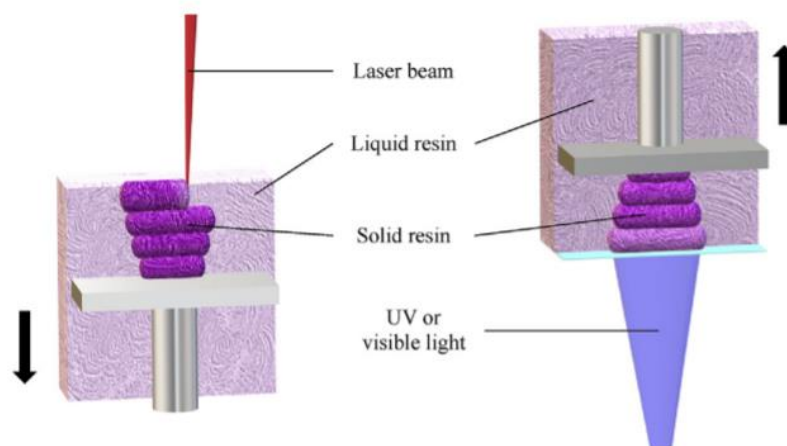


Figure 20: Stereolithography approaches. Left: a bottom-up approach with laser beam. Right: a top-down approach with light projection.<sup>89</sup>

**Extrusion-based technology** is normally used with heat, which melt bulk material in a small chamber. The semisolid material is pushed through by a tractor-feed system that creates the pressure necessary for extrusion. The shape must be maintained during the cool-down and solidification whilst bonding to the already extruded material. If the temperature is extremely high, an additional cooling system is required.

There are two different approaches when dealing with extrusion technology. The first and most common process is based on temperature as a control over the material state. The liquefied material can flow out the nozzle and bond with adjacent material prior to solidification. The alternative approach is based on chemical reactions that cause the solidification. A curing agent or reaction with air is the cause of bonding. After the completion of the part, it must dry to be fully solid.

Some key factors are common for both the processes before described: loading of the material, liquification (caused by heater coils wrapped around the chamber), pressure application for extrusion, plotting according to a predefined pattern, bonding the material to itself or secondary built materials, inclusion of supporting structures (being similar material or secondary material support). The extrusion nozzle will determine the shape and size of the extruded filament. If is larger the material will flow more rapidly but will determine a lower resolution structure. It must be noted that the resolution limit is the nozzle diameter itself, no structure can be smaller than that diameter. The solidification must not change the shape, size or cause the shrinking of the material. Moreover, it must be as much a linear process as possible because can develop a distorted part after cooling.<sup>86</sup>

**Fuse deposition modelling (FDM)** is the most common extrusion-based AM technology and involves the use of a heating chamber to liquify polymer, then pushed onto a solid platform. The nozzles trace the cross-section pattern for every layer and the polymer is let harden before the following step. Like SL, a supporting material might be needed for some models. The crucial advantages of this technology are the elimination of potential toxicity of organic solvents used to solubilize certain polymers and the effective mechanical properties of the extruded part. In fact, parts created with FDM are among the strongest for any polymer-based AM process.<sup>87</sup> The materials mainly used are amorphous polymers, because increasing the temperature lead to a soften and low-viscosity material. Therefore, those polymers are extruded in a viscous paste form, which enable to largely maintain their shape after the extrusion. The main disadvantages are related to speed, accuracy and material density.

**3D Bioplotter** is an extrusion-based technology designed for biopolymers. Lower temperature polymers can be extruded through a compresses gas feed, while the system is usually composed of nonreactive stainless steel. The system can use one extrusion head at a time, which is extremely useful since most TE approaches are based on scaffold with different regions composed of different materials. Bioplotter can use bioink; the main disadvantages are the shear stresses from the nozzles that could impact negatively on cell viability during the printing process.<sup>86</sup>

**Binder Jetting (BJ)** is a technology, first developed at MIT in early 1990s. They called that technology 3D Printing (3DP) and is based on the selective printing of the binder on a layer of loose powders according to CAD file, as presented in figure 21. The layer of powder is spread and levelled by a set of rollers with predetermined thickness and the printhead sprays the binder, organic or water based. The droplets (typically around 80  $\mu\text{m}$  in diameter) form spherical agglomerates of binder liquid and powder particles, while providing bonding to the previously printed layer. Then the platform is lowered, and a new layer of powder is deposited, usually through a counter-rotating rolling mechanism. After the part completion, it is usually left within the powder bed to let the binder to fully set and the part itself to strength. Post-processing involves the removal of the excessive powder via pressurized air, infiltrating the part with an infiltrant to make it stronger and possibly to impart other mechanical properties. Unprinted powders are fully recyclable, therefore can be used to produce other parts. A wanted characteristic of powder is a high packing density (in order for the part to have high volume fraction) and the strength for survive depowdering and cleaning up operations.<sup>86</sup>

Various materials can be used with this kind of application, for example metallic, polymer, composite and ceramics materials (e.g. HA, calcium phosphate, calcium sulphate and bioactive glasses). The process does not need for supporting structures and can be scaled by increasing the printer nozzles, therefore can be considered a scalable, line-wise patterning process. Advantages of BJ are the low energy required, the relatively fast and inexpensive processes. Another advantage of this technology is the wide range of powder-binder solutions available. It must be noted that the binder, especially if organic based, can lead to toxicity if not completely removed from the structure. Other important disadvantages are the complex post processing, poor accuracy and surface quality.<sup>73,87</sup>

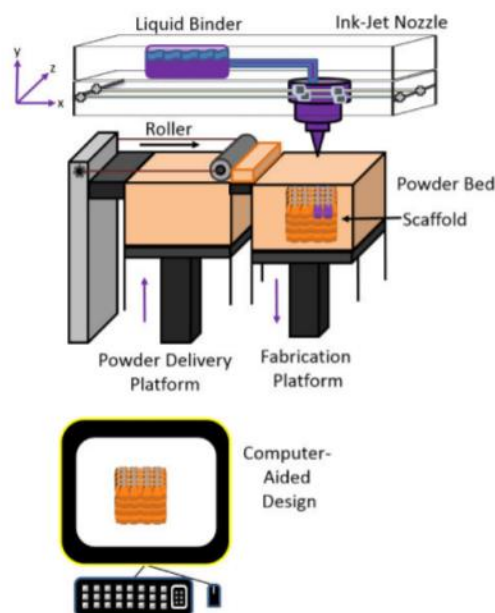


Figure 21: Schematic of direct 3D printing.<sup>87</sup>

Finally, in figure 22 are presented some examples of structures obtained through the AM technologies previously described.

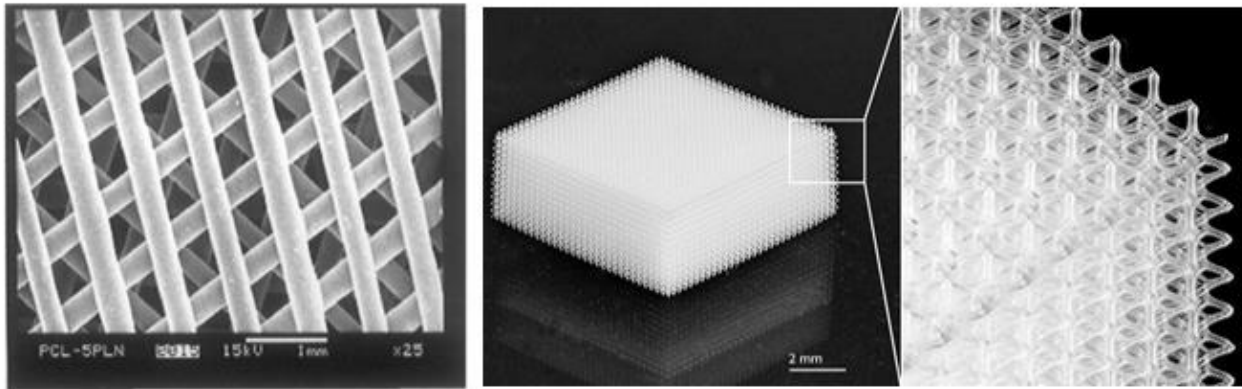


Figure 22: Example of structures obtained by AM. Left: scaffold produced by FDM. Right: scaffold and detail magnification of a structure produced by 3D printing.<sup>75,92</sup>

## 2.4 Composite materials in additive manufacturing

In medical applications, polymeric materials are good selections for soft tissue engineering approaches, while for hard tissue, these materials are not completely appropriate. In fact, single-class materials are not able to currently satisfy all the requirements needed for an implantable device. In case of polymeric materials, the main issues are related to the usually lacking mechanical properties, and the degradation profile difficult to control. To improve the devices' features, several composites or blends can be produced. In a polymeric blend the components are accurately selected to fully accomplish the requested target properties. In a binary structure, usually at least one semicrystalline polymer is included because of its superior mechanical properties. Semicrystalline/semicrystalline polymer blends are more difficult to obtain but show a greater range of investigation on both crystallization behaviour and morphology. The components' miscibility is a crucial parameter in determining the final properties of the blend. Miscible polymers determine homogeneous blends, while immiscible polymers exhibit separated phases and the crystallization depends strongly on the interfacial properties.<sup>93</sup>

Composites are generally manufactured by combining natural polymers, polysaccharides and proteins (highly bioactive and chemically versatile), or bioactive ceramic materials, such as HA, calcium silicate glasses or MBGs.<sup>74</sup> Ceramics are brittle but characterized by higher mechanical properties than polymers, hence can improve the device mechanical properties.<sup>24</sup> The ceramic phase enhances biocompatibility, tissue integration and can buffer the pH decrease associated to by-products of the polymer degradation, hence avoiding the

formation of an unfavourable environment for the cells.<sup>75</sup> Moreover, the ceramic phases can generate nano/microscale topology on the composites, increasing the hydrophilicity of the device.<sup>91</sup> It is foremost important to achieve good compatibility between the phases while keeping the porous structure and the mechanical properties of the device.<sup>74</sup>

Even in the field of AM technologies, despite the advantages regarding the design and geometry complexity freedom, the main issue is related to the limited range of materials compatible with printing technologies. Therefore, there is also a restricted variation in the physical and chemical properties of the printing objects. There is a growing interest in printing composite material through multiple printing heads or, alternatively, pre-blended the materials. In the first case, the machine gains the ability to print layered composite materials, from which objects with variable features and gradient functionality can be produced. In the pre-blend case, the machine prints directly the composite, a printable material with inclusions of fillers. The blend will have diverse physicochemical properties from the original materials and exhibit unique capabilities.<sup>94</sup>

Several improvements in device properties have been reported in the literature when using composite materials in AM processes. The main advantages are expressed in terms of tensile strength, Young's modulus and elongation.<sup>95</sup> Composite materials based on polymers and ceramics gained great attention because of the advantages of the mixed materials. In particular, those advantages are the high strength provided from ceramic phase and toughness and plasticity provided from polymeric phase. FDM printing methods produced scaffolds with promising properties suitable for bone regeneration, with enhanced bioactivity, osteogenic ability and mineralization of mesenchymal stem cells.<sup>94</sup>

Table 12 summarizes some examples of 3D printing for bone tissue engineering based on polymer/ceramic composites. Some of them will be briefly described.

*Table 12: Summary of 3D printers based on printing type, matrix and fillers.*

<b>Printer</b>	<b>Matrix</b>	<b>Additive/fillers</b>	<b>Reference</b>
FDM	PLA	TCP	96
FDM (mini extrusion)	PCL	TCP	97
Direct printing tool	PLA	Bioactive glass	98
Indirect 3D printing	PCL	HA	99
3D printing	PLA	HA	100
3D printing	PLA	Bioglass	101
FDM	PLGA	TCP/HA	102

Senatov et al.<sup>100</sup> developed a composite using PLA as a matrix and HA as ceramic filler. The 3D printing was demonstrated not affecting the overall original PLA structure, also when combined the ceramic phase. The structure was porous and well interconnected, hence supporting bone formation within the matrix.

Serra et al.<sup>101</sup> printed a PLA/Bioglass composite scaffold. The technique allowed a precise and repetitive control over the internal architecture, while the glass particles demonstrated an increased cell adhesion. This was achieved by the increased roughness and hydrophilicity of the scaffold.

Kim et al.<sup>102</sup> printed a PLGA/TCP/HA scaffold, which was then successfully implanted into a rabbit femur. The device was able to support bone deposition and after 12 weeks was completely biodegraded into non-toxic compounds.

Despite the advantages and the successful experiments, some open issues concern the flow properties, the layer thickness and the possible formation of voids and micro-voids. The voids can be caused by poor adhesion between the phases or the volatile compounds vaporization, introduced with the fillers, during the extrusion. The quality of the final product will consequently strongly depend on the quality of the mixing process. Usual problems arising with nanomaterial inclusions are agglomeration and non-uniform dispersion. The geometrical size of the incorporated particles is also important because can generate composites with inconsistent thermo-mechanical properties. A major limitation, especially in melt extrusion printing processes, is the difficult realization of small filaments (the minimum is typically 50-100  $\mu\text{m}$ ). Moreover, several commercial printers are still not able to handle composites with different filler types and loadings.<sup>95</sup>

The composite material will be created using a protocol based on material extrusion to produce composite filaments able to be processed using Fused Filament Fabrication (FFF), an additive manufacturing technique. The filaments produced in the present work are composites, where the polymeric phase guarantees the biodegradability and toughness, whilst the bioceramic phase improves the bioactivity of the material, therefore its bone healing properties.<sup>91</sup> The fabrication of a composite device depends on the preparation and optimization of the composite formulation. In the frame of the project, the focus is to synthesise in Politecnico di Torino, IRIS group, mesoporous bioactive glasses doped with strontium ions, since these have proven abilities towards accelerating bone healing. These phases will be incorporated in a PLLA matrix (FDA approved polymer), which was chosen for its mechanical strength and biodegradability. Other composites are formulated based on nano-hydroxyapatite-PLLA formulations, where nano-HA, synthesised with different degrees of strontium ion substitution, is provided by a partner of GIOTTO consortium. The aim is to investigate the most successful incorporation mechanism, through the evaluation of the compositional and mechanical properties of the filaments. As incorporation method, polymer immersion was chosen, where the pellets are covered with a paste containing the inorganic phase, in different concentrations, and the resultant material used as feedstock for the extrusion of a composite filament. The extrusion process allows the homogenisation of the material allowing for good dispersion of the inorganic phase within the polymer matrix. Once optimised, the

filament size should also be optimised and controlled, reaching a diameter of 1.75 mm. During the printing process, the filament is fed through a temperature-controlled nozzle, where it melts, creating a melt-pool. The material is then extruded and selectively deposited in a layer-by layer fashion, to produce the desired geometry. An insufficient diameter will prevent material deposition, whilst an excessive one will provoke the jamming of the feeding system.

### 3 – Materials and methods

The aim of the present work is to develop and characterize polymeric poly(l-lactic acid), PLLA, filaments incorporating bioactive inorganic phases, both nanometric hydroxyapatite (nano-HA), substituted with different percentage of strontium (0 – 50 – 100%), or mesoporous bioactive glasses, containing 10% molar of strontium.

Pure hydroxyapatite and 100% strontium substituted HA were provided in alkaline water suspension and HA with 50% of strontium have been provided by a company, Fluidinova (Porto, Portugal), one of the partners of GIOTTO consortium.

MBGs have been produced by two different techniques, a basic medium sol-gel synthesis and a spray-drying aerosol-assisted sol-gel procedure, respectively. The HA provided in powder form were directly characterized, the HA provided in form of water suspension was evaporated prior the characterization.

Two different incorporation procedures were tested, one based on alkaline water suspensions provided by Fluidinova, and the other based on produced water suspensions. The aim was to compare the methods and evaluate the best incorporation procedure, in term of powder dispersion and the overall quality of the extruded filament. The provided suspensions (HA\_0%Sr and HA\_100%Sr) or water suspensions produced from the powders (HA\_50%Sr provided by Fluidinova and the synthesised MBG\_SD\_10%Sr and MBG\_SG\_10%Sr), were dispersed over the polymer pellets with different powder concentration (5% for the HA and 2% for the MBGs). The obtained pellets covered with inorganic phases were extruded into a filament, with the final aim of its extrusion through AM technologies into a composite device.

MBG were characterized to confirm the micro and nanostructure and the effective strontium ion inclusion. It was also evaluated the strontium ions release rate, to evaluate the MBGs ability to release the incorporated ions.

The pure and substituted nano-HA were characterized to confirm the HA formation even with strontium ion substitution. Additionally, (Ca+Sr)/P ratio was assessed and compared to the stoichiometric ratio of the non-substituted apatite.

The pure PLLA and composites filaments, obtained through extrusion processing, were characterized to evaluate the effect of the inorganic phase within the polymeric matrix. Then mechanical and rheological assessment were conducted to evaluate the changes in the overall properties of the filament after the inorganic phase incorporation.

## 3.1 Materials

### 3.1.1 Synthesis of MBG containing strontium ions by sol-gel synthesis in basic medium

Mesoporous bioactive glass with 10% molar percentage of strontium ( $\text{Sr/Ca/Si} = 10/5/85$ ) were synthesised similarly as conducted by Wu et al.<sup>103</sup> The utilized reagents were:

- Tetraethyl orthosilicate (TEOS- $\text{C}_8\text{H}_{20}\text{O}_4\text{Si}$ ,  $\geq 98\%$ , Sigma Aldrich);
- Cetyltrimethylammonium bromide (CTAB,  $\geq 98\%$ , Sigma Aldrich, Milan, Italy);
- Ammonium hydroxide solution ( $\text{NH}_4\text{OH}$ , Sigma Aldrich, Milan, Italy);
- Strontium nitrate ( $\text{Sr}(\text{NO}_3)_2$ , Sigma Aldrich, Milan, Italy);
- Calcium nitrate tetrahydrate ( $\text{Ca}(\text{NO}_3)_2 \cdot 4\text{H}_2\text{O}$  -CaNT-, 99%, Sigma Aldrich, Milan, Italy);
- Ethanol (EtOH);
- Deionized water (ddH<sub>2</sub>O).

The procedure is based on the following steps:

- 1- Solution 1 was created dissolving 12 g of CTAB in 25 mL of  $\text{NH}_4\text{OH}$  and 140 mL of EtOH;
- 2- Solution 2 was created dissolving 9.4 g of TEOS in 50 mL of EtOH;
- 3- Both solutions were stirred for 20 minutes;
- 4- Solution 1 was added to solution 2 and stirred for 20 minutes;
- 5- 0.94 g of CaNT and 1.67 g of  $\text{Sr}(\text{NO}_3)_2$  were then added and stirred for 10 minutes;
- 6- 4.7 g of TEOS were then added and stirred for 5 hours.
- 7- The solution was then centrifuged (Hermle Labortechnik Z326, Hermle LaborTechnik GmbH, Wehingen, Germany) at 10,000 rpm for 3 minutes and distilled three times with water, once with 50% ethanol and once with 100% ethanol.
- 8- The solution was dried overnight at 70 °C.
- 9- The powder was finally calcinated at 600 °C in air for 5 hours using a furnace (heating ramp 1 °C/min, Carbolite 1300 CWF 15/5, Carbolite LTD, Hope Valley, UK) to avoid CTAB residues.

### 3.1.2 Synthesis of MBG containing strontium ions by aerosol-assisted spray-drying process

Spray-drying is a widely applied technique for particle production and consists on the transformation of a fluid material into dried spheres, taking advantage of a hot gaseous (often air) drying medium. The process continues until the desired moisture content in the particle is reached, after which the product is separated from the air.<sup>104</sup>

Figure 23 shows the spray-drying mechanism; the technique can be described by three main phases.

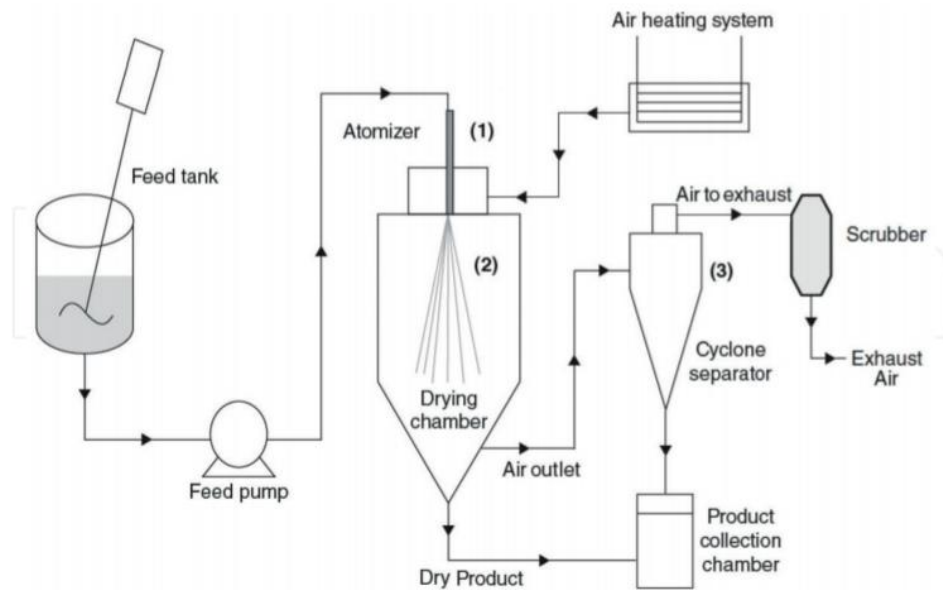


Figure 23: Schematic representation of spray-drying mechanism. 1) Atomization. 2) Droplet-to-particle conversion. 3) Particle collection.<sup>105</sup>

1. Atomization: the solution is atomized in small droplets due to a decrease of surface tension. This process is accompanied by an increase in the surface area of the droplets, therefore optimizing the heat and mass transfers between the heated drying gas and the liquid particles. This process can be performed by pressure, centrifugal, electrostatic or ultrasonic energy.
2. Droplet-to-particle conversion: atomized particles are exposed to a hot gas within the drying chamber, resulting in a rapid moisture evaporation and solute condensation. Consequently, the solvent is removed, and the droplets are transformed into dried particles.
3. Particle collection: this final process implies the separation of the particles from the drying gas. There are two steps in this stage; on first primary separation, where the densest particles are collected at the conical bottom of the chamber. The secondary separation then occurs, where the finest particles are transferred to external devices and separated from the humid air. The equipment can generally combine a cyclone separator, a bag filter and an electrostatic precipitator.<sup>105</sup>

In the present work, the machine used is the Mini Spray-Dryer B-290, Büchi Labortechnik AG, Flawil, Switzerland, figure 24.



Figure 24: Mini Spray-Dryer B-290 Büchi Labortechnik.

The utilized reagents are:

- Tetraethyl orthosilicate (TEOS- $C_8H_{20}O_4Si$ ,  $\geq 98\%$ , Sigma Aldrich);
- Pluronic P123 ( $EO_{20}PO_{70}EO_{20}$ , average Mn  $\sim 5800$ , Sigma Aldrich, Milan, Italy);
- Calcium nitrate tetrahydrate ( $Ca(NO_3)_2 \cdot 4H_2O$  -CaNT-, 99%, Sigma Aldrich, Milan, Italy);
- Strontium chloride ( $SrCl_2$ , Purity, Sigma Aldrich, Milan, Italy);
- Hydrochloric acid (HCl);
- Deionized water (ddH<sub>2</sub>O).

The procedure adopted to produce the spray dried MBG particles implies the following steps:

- 1- Solution 1 is prepared dissolving 2.03 g of Pluronic P123 in 85 mL of deionized water in continuous agitation due to a magnetic agitator;

- 2- Solution 2 is prepared dissolving 10.73 g of TEOS in 5 g of HCl under continuous magnetic stirring, to avoid the hydrolysis of silica precursor;
- 3- Both solutions are held under continuous stirring for about 3 hours, or until the solutions appear clear;
- 4- Solution 2 is added drop by drop to solution 1; the final solution is kept under vigorous stirring for 1 hour;
- 5- 1.62 g of SrCl<sub>2</sub> is added and, when the solution's temperature reached 145 °C, 0.72 g of CaNT was added drop by drop.
- 6- The solution is then sprayed using nitrogen as atomizing agent. The inlet temperature was set 220 °C, feed rate 3.0 mL/min and gas flow 1744L/h.
- 7- The obtained powders were then calcinated using a furnace (Carbolite 1300 CWF 15/5, Carbolite LTD, Hope Valley, UK) at 600 °C for 5 hours, with a heating ramp of 1 °C/min and a cooling ramp of 10 °C/min to remove the template.

### 3.1.3 Incorporation of bioactive inorganic phases in PLLA pellets

The following procedures were developed in “Biofablab” laboratory, Hershel Annex Building, at Newcastle University. The activities conducted at Newcastle University were performed under the supervision of Prof. Kenny Dalgarno.

Medical grade PLLA (Purasorb PL 38, Corbion - Purac Biomaterials) was utilized as polymer matrix for all the performed experiments.

Two incorporation procedures were tested to create the composites, one based on Fluidinova alkaline water suspensions and the other based on water suspension produced from the synthesised or provided powders.

#### *3.1.3.1 Fluidinova suspensions: production of PLLA\_HA\_0%Sr and PLLA\_HA\_100%Sr composites*

Water suspensions of HA, pure and substituted with 100% of strontium ions, were provided by Fluidinova (Porto, Portugal). Both suspensions, named by the producer ‘nanoXIM-Hap100’, were supplied as a package of 40 g at 15 wt% concentration.

In Table 13 will be described some of the product properties, according to the technical data sheet provided from the factory.

Table 13: General specification of the HA suspensions from Fluidinova.

General specifications	Unit	Value
Phase purity of Hydroxyapatite	%	100
Total heavy metals (as Pb)	ppm	≤ 20
Specific surface area	m <sup>2</sup> /g	≥ 80
Particle size	nm	< 50

The pellets were combined with 5 wt% of HA, as generally composites in the literature were produced with a limited amount of powder content.<sup>106</sup> The weights for pellets and suspensions are summarized in Table 14.

Table 14: Weight of the PLLA pellet and provided suspensions in the desired concentration.

Sample	PLLA pellet (g)	Suspension (g)	HA (g)	Final HA concentration (%)
PLLA_HA_0%Sr	15	7.5	1.125	5
PLLA_HA_100%Sr				

The incorporation procedure is the following:

- pellets and suspensions were weighted and carefully mixed to cover the polymer with the HA suspension homogeneously (Fig. 25);
- the product was covered with aluminium foil and let dry under vacuum for complete water evaporation;
- every 12 hours the composites were removed from vacuum and carefully mixed;
- the possible moisture from the leftover suspension was dried in oven 50 °C, overnight. The obtained dried pellets were then extruded.



Figure 25: Pellets production. Left: PLLA mixed with HA suspension. Right: dried pellets.

### 3.1.3.2 Water suspensions produced from powders: production of PLLA\_HA\_50%Sr, PLLA\_MBG\_SD\_10%Sr and PLLA\_MBG\_SG\_10%Sr composites

Aqueous suspensions of HA with 50% of strontium ion content (HA\_50%Sr) and both MBGs samples, (MBG\_SD\_10%Sr and MBG\_SG\_10%Sr), were prepared for proceeding to the incorporation into PLLA pellets. All the suspensions were prepared with a concentration of 15 wt%.

Table 15: Weighted material to prepare water suspensions.

Sample	Powder (g)	Water (g)	Suspension concentration (%)
HA_50%Sr	1.125	6.375	15
MBG_SD_10%Sr	0.346	1.961	15
MBG_SG_10%Sr			

The powders were weighted in a vial, mixed with a *Vortex* mixer for 30 seconds and then moved in a beaker. The beaker was then covered with aluminium foil and put on a stirrer for 20 minutes at room temperature at 300 rpm, to create a homogeneous suspension (Fig. 26).

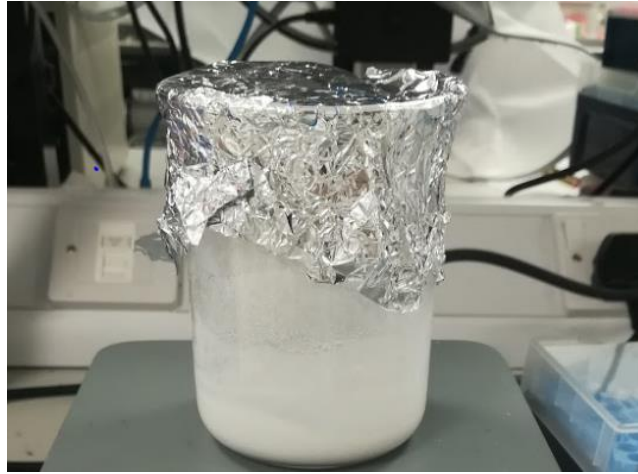


Figure 26: Stirring of MBG\_SG\_10%Sr aqueous suspension.

The needed materials for obtaining the composite pellets are listed in Table 16; the subsequent incorporation procedure was the same as previously described in section 3.1.3.1.

The obtained dried pellets were extruded.

Table 16: Weight of the PLLA pellets and suspensions for each formulation.

<b>Sample</b>	<b>PLLA pellet (g)</b>	<b>Suspension (g)</b>	<b>Powder (g)</b>	<b>Inorganic phase concentration (%)</b>
PLLA_HA_50%Sr	15	7.5	1.125	5
MBG_SD_10%Sr MBG_SG_10%Sr	15	2.307	0.346	2

### 3.1.4 Extrusion process of pure PLLA and hybrid formulations

The machines used are the Rondol 10mm Twin Screw Mini Extruder (for the extrusion of the filaments) and the Rondol Haul-Off Machine (for the control of the filament's dimensions), figure 27.

The following procedures were developed in "Extrusion G30" laboratory, Stephenson Building, at Newcastle University.



Figure 27: Left: Rondol 10mm Twin Screw Mini Extruder. Right: Rondol Haul-Off.

Pure PLLA pellets, with an average diameter of at least 3 mm, were put in the feeder. Once the machine had reached the correct temperature values (Table 17), the extruder and feeder screw can be activated. The melted polymer filled the barrel, then the die and, finally, the pressure pushed out the filament. In this case, the die was 2 mm. The extruded filament was then placed in the Haul-Off machine, between the treads of its conveyor belt. On the left side of the machine (Fig. 28 right), as the filament is freed from the belt, a laser-measuring tool gave a real time analysis of the filament diameter.

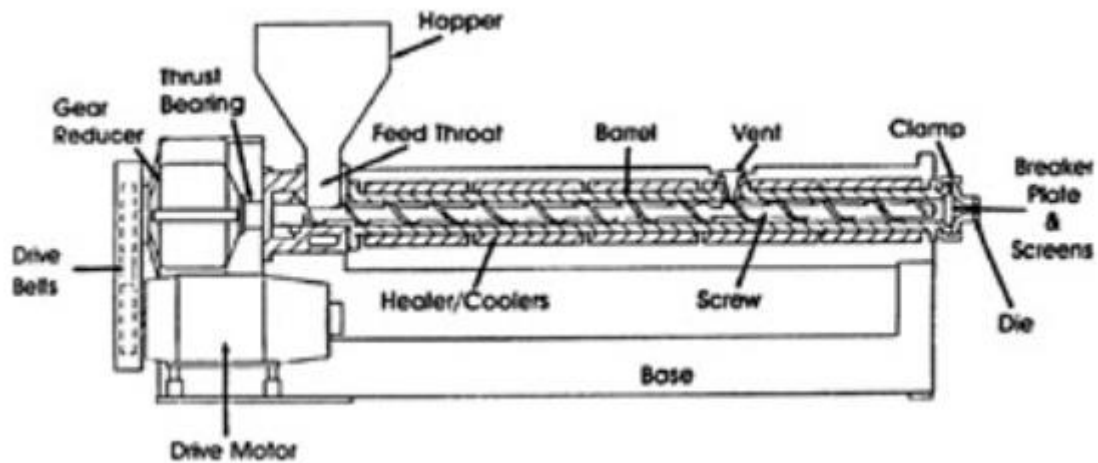


Figure 28: Schematic representation of a single-screw extruder.<sup>107</sup>

Great attention was given over the critical parameters of the process, such as the extruder, feeder screw and Haul-Off speeds, pellet size, temperatures through the barrel and die. As a control, the pressure must be under 100 bar and the torque must not exceed 15 Nm, otherwise damages in the machine could occur. Those values were never reached during the experiments.

### 3.1.4.1 Extrusion of pure PLLA pellets

The first extrusion was performed for the pure medical grade PL 38 PLLA sample. Since the optimal diameter for the FFF machine that will be subsequently used for the fabrication of the final device is around 1.7-1.75 mm, the parameters were optimised to obtain a consistent diameter falling in this range.

Table 17: Parameters used in the extrusion of pure PLLA sample.

<b>Parameter</b>	<b>Data</b>
T1	125 °C
T2	240 °C
T3	240 °C
T4	220 °C
T Die	180 °C
Extruder	30 rpm
Feeder	14 rpm
Haul-Off	1.00 m/min

The following sections describe the parameters set for the extrusion of the composite pellets. The extrusion parameters, as will be discussed, needed to be adjusted to avoid inconstancy of diameters and an uncontrollable increase in machine torque.

### 3.1.4.2 Extrusion of PLLA\_HA\_0%Sr and PLLA\_HA\_100%Sr composites

The temperatures were the same as the previous case to avoid polymer degradation.<sup>108</sup> The optimized parameters are:

Table 18: Parameters used in the extrusion of PLLA\_HA\_0%Sr and PLLA\_HA\_100%Sr samples.

Parameter	Data
T1	125 °C
T2	240 °C
T3	240 °C
T4	220 °C
T Die	180 °C
Extruder	55 rpm
Feeder	17 rpm
Haul-Off	1.00 m/min

### 3.1.4.3 Extrusion of PLLA\_HA\_50%Sr – PLLA\_MBG\_SD\_10%Sr – PLLA\_MBG\_SG\_10%Sr composites

- First extrusion: temperatures and speeds were the same as pure PLLA (Table 18).
- Second extrusion: the filament obtained from the first process was pelletized using a Rondol pelletizer, and re-extruded. The parameters were:

Table 19: Parameters used in the second extrusion of PLLA\_HA\_50%Sr, PLLA\_MBG\_SD\_10%Sr and PLLA\_MBG\_SG\_10%Sr samples.

Parameter	Data
T1	125 °C
T2	200 °C
T3	200 °C
T4	180 °C
T Die	160 °C
Extruder	19 rpm
Feeder	17 rpm
Haul-Off	1.00 m/min

## 3.2 Methods of characterization

### 3.2.1 Nitrogen adsorption-desorption

Adsorption, in general, is defined as the enrichment of molecules, atoms or ions in the vicinity of an interface and can be physical (physisorption) or chemical (chemisorption). The first is a general phenomenon and occurs whenever an absorbable gas is brought in contact with the adsorbent's surface; the second one leads to formation of chemical bonds. In the context of the present analysis method, the process utilized is physisorption.<sup>109</sup>

The amount of adsorbed gas (adsorptive) depends on the exposed surface but also on temperature, gas pressure and strength of solid-gas interaction. In adsorption-desorption analysis, nitrogen (N<sub>2</sub>) is usually utilized because of its availability in high purity and its ability to interact with a great variety of solids (adsorbent). The mechanism is based on gas adsorption (the forces involved are generally weak, e.g. based on Van der Waals forces) at a defined relative pressure ( $p/p_o$ , with  $p$  partial pressure and  $p_o$  saturation pressure). The data obtained from this analysis are presented as an isotherm, plotting the amount of adsorbed gas as a function of the relative pressure.<sup>110</sup>

Among the possible isotherms, type IV isotherm is typical of mesoporous materials (with a diameter between 2 and 50 nm) and is associated with capillary condensation within mesopores due to the confinement effect. Capillary condensation is associated with reproducible, permanent hysteresis loops, which are in the multilayer range of physisorption. The main types of hysteresis loops were identified in the original IUPAC classification of 1985.<sup>109</sup> The type of hysteresis loop that most commonly characterize mesoporous materials is Type H2 loop (generated by a complex pore structure).

From the isotherms, it is possible to obtain information about the specific surface area of the analysed sample. Among the possible methods, the most widely used, also utilized in this work, is based on the Brunauer, Emmett and Teller (BET) equation. BET equation is an extension of the Langmuir theory relating the monolayer adsorption of gas molecules onto a solid surface and is based on two stages. Firstly, the physisorption isotherm needs to be transformed into a BET plot, then from it derive the BET monolayer capacity. In the second stage, the specific surface area is calculated from the monolayer capacity by adopting an appropriate value of the molecular cross-sectional area.<sup>109</sup>

Beside specific surface area, pore size distribution. DFT (Density Functional Theory) and NLDFT (Non-Local Density Functional Theory) are the utilized simulations in this case. These approaches are able to analyse the distribution of adsorbed molecules and therefore provide information about the local fluid structure near the adsorbent surface.



Figure 29: ASAP2020 from Micromeritics for  $N_2$  adsorption-desorption analysis.

In this work, the equipment used is ASAP2020 from Micromeritics (Fig. 29), and the adsorption-desorption isotherms were evaluated with nitrogen as absorbent at  $-196\text{ }^\circ\text{C}$ . Before the analysis, the powders were degassed. The sample was loaded within a glass burette, it was degassed and heated at  $150\text{ }^\circ\text{C}$ . After this process, the sample was exposed to an overpressure of helium gas to avoid contaminations during the shift toward the analysis station. During the measure, the sample underwent an increasing pressure of nitrogen thanks to a *dewar* containing liquid nitrogen. Finally, after the measure is complete, the machine software is able to give back the sample isotherm.

### 3.2.2 Field emission scanning electron microscopy (FESEM)

Field emission scanning electron microscopy (FESEM) provides topographical and elemental information at magnifications from 10x up to 300,00x, with unlimited depth of field. Compared to conventional scanning electron microscopy (SEM), field emission SEM produces cleaner, less electrostatically distorted images with spatial resolution down to 1 nm three to six times better.<sup>111</sup> Some of the application of FESEM technology are measure of the thickness of coatings or films, measure of height and lateral dimensions of nanometre-sized objects, correlation of surface appearance and morphology, electrical conductivity, elemental analysis, as well as fracture, failure and defect analysis.<sup>112</sup>

An example of FESEM system is presented in figure 30. The system utilizes electrons liberated by a wire, generally made of Tungsten, to create the image; the metallic filament functions as a cathode and is placed in front of an anode. The voltage applied between anode and cathode is in the range of 0.5-30 kV, so high that the electrons in the wire can leave the material. As the equipment within the column of the microscope requires an extreme vacuum (around  $10^{-6}$  Pa), a device is present to regularly decontaminate the electron source. The emitted primary electrons are focussed and deflected by a system of lenses to produce a narrow beam that bombards the object. Because of the impact, secondary electrons are emitted from the selected spot. Those electrons are captured by a detector and the event produces an electronic signal; the signal is then amplified, transformed into a video-scan image that can be seen on a monitor and further processed.<sup>112,113</sup>

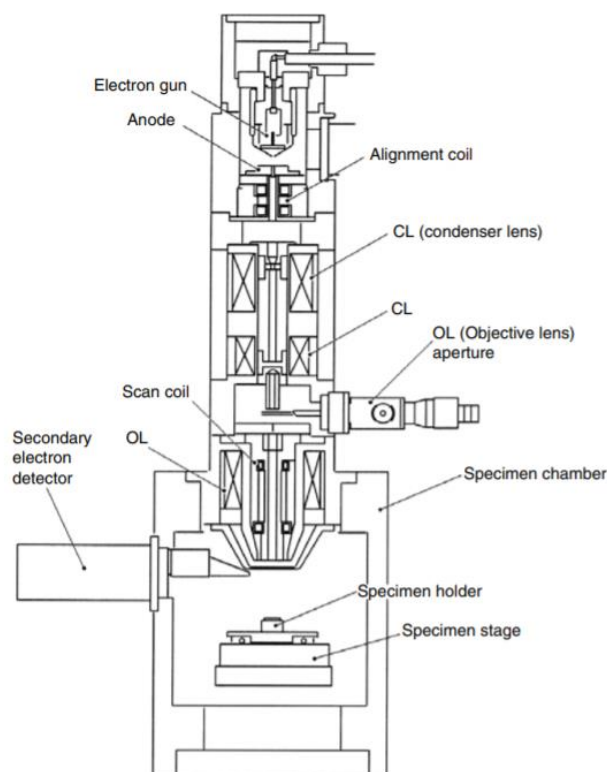


Figure 30: Schematic diagram of FESEM.<sup>114</sup>

The secondary electrons, typically having low energy of 3-5 eV, can only escape from a region within a few nanometres of the material surface. They can accurately give topographic information with good resolution (they can resolve structures of 10 nm or lower). The image quality is dependent on how many of the secondary electrons are physically reaching the detector; those who cannot will create shadows.<sup>114</sup>

The instrument used was a ZEISS MERLIN (ZEISS MERLIN Instrument, Oberkochen, Germany). The same instrument was exploited to perform energy-dispersive X-ray spectroscopy (EDS) analyses in order to confirm the samples composition.

The sample preparation for the analysis is different in case of powders and filaments. Due to the extremely small dimensions of the powders, a suspension with isopropanol was created. 10 mg of powders were put into a glass vial and 3 mL of isopropanol were added. The obtained suspension was sonicated for 10 minutes (Digitec DT 103H, Bandelin). Then, 10  $\mu$ L of the suspension was deposited on carbon-coated copper grid (3.05 mm Diam.200 MESH, TAAB, Aldermaston, Berks, UK). After the isopropanol was dried, the grid was blocked with adhesive tape. The samples were then coated with 7 nm chromium layer.

As for the polymeric filaments, those were cut in 3 mm portions and placed over the stub to expose the cut section. The samples were then metallized as previously described.

### 3.2.3 Energy dispersive X-ray Spectroscopy (EDS)

Energy dispersive X-ray Spectroscopy (EDX or EDS) is often associated to FESEM machines (Fig. 31) and is utilized to identify the elemental composition of the sample. The technique is non-destructive with a sensitivity greater than 0.1 % for elements heavier than carbon. EDS detects the X-rays that are produced by the beam-sample interaction. The energy of X-rays is characteristics of the atoms that produced them, forming peaks in the spectrum.<sup>112</sup>

It must be noted that some elements are represented by more than one peak in the spectrum, therefore it is necessary to consider a possible overlap. The electron beam is precisely controllable, hence EDS analysis can be conducted to a desired area of only few cubic microns; otherwise, the beam can sweep over a selected area of the sample to identify the elements in the whole region.<sup>112</sup> EDS was useful to prove strontium ion incorporation in the bioactive matrices and the inorganic phase incorporation in the extruded filament.



*Figure 31: FESEM ZEISS MERLIN with EDS analyser.*

### 3.2.4 X-ray Diffraction (XRD)

X-ray diffraction (XRD) is a non-destructive technique able to characterize materials, as provides detailed information about the crystallographic structure, chemical composition, physical properties and other structural parameters (e.g. average grain size, crystallinity, strain and crystal defects). The peaks of the diffraction pattern are produced by constructive interference of a monochromatic beam of X-rays scattered at specific angles from each set of lattice planes in a sample.<sup>115</sup> Bragg's law allows to derive lattice spacings:

$$n\lambda = 2d \sin\theta$$

where:

$n$  is an integer called the order of reflection;

$\lambda$  represents the wavelength of X-rays;

$d$  is the characteristic spacing between the crystal planes of a certain material;

$\theta$  is the angle between the incident beam and the normal to the reflecting lattice plane.<sup>116</sup>

The diffracted X-rays, after the collision with the sample, are detected and processed. By scanning the sample through a range of  $2\theta$  angles, all possible diffraction directions of the lattice should be achieved, thanks to the random orientation of the scanned material. The intensity of the peaks is regulated by the atomic positions within the lattice planes. The X-ray pattern is characteristic of the periodic atomic arrangements of a material hence each pattern is unique.<sup>115</sup>

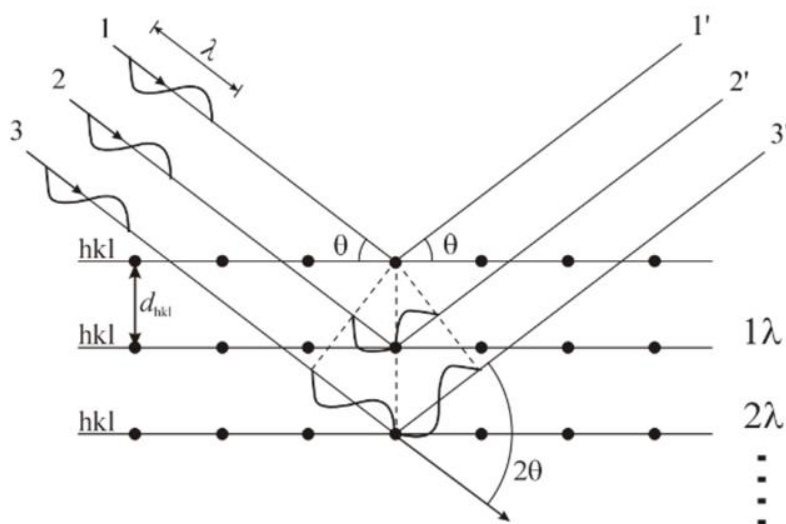


Figure 32: Diffraction phenomenon.

X-rays are generated through the heating of a filament to produce electrons. Those are then accelerated toward the target thanks to an applied voltage and are used to bombard the target material. If those electrons have enough energy to dislodge the electrons of the target material, X-ray spectra are produced. The sample and detector are rotated, the overall constructive interferences are recorded and converted into the signal that is then printed on the computer monitor.<sup>117</sup>

The results are normally presented in a graph presenting peak position at  $2\theta$  and X-ray intensity. The intensity at a specific angle  $\theta$  is recorded as peak intensity ( $I$ ) and most intense peak ( $I_{max}$ ) ratio.

$$relative\ intensity = \frac{I}{I_{max}} \times 100$$

In the frame of this work, the utilized instrument is *X'Pert PRO* from *PANalytical*. The analysis was conducted imposing 40 mA for the current and 40 kV for the voltage. The rotation step was fixed at  $0.0131303^\circ$ , and the range of angles analysed is comprised between  $10$  and  $80^\circ$ . The time required for every measure was 30 seconds. This instrument was used for the HA characterization, to confirm its structure even with the strontium substitution.

### 3.2.5 Strontium ion release test from inorganic phases

The inorganic phases were subjected to release test, to assess the ability to release the strontium ion.

The pattern of Sr<sup>2+</sup> ion release from inorganic phases was investigated by soaking 5 mg of powder in 20 mL of Tris HCl buffer (0.1 M, pH 7.4). The solution was stored in a Falcon and incubated at 37 °C in an orbital shaker (Excella E24, Eppendorf). The continuous shaking was necessary to avoid powder deposition and optimizing the contact with the solution.

The procedure to produce 1 litre of Tris-HCl solution was:

- 1 L of ultrapure water was heated (37 °C);
- it was dissolved 12.114 g of TRIZMA BASE® (Sigma Aldrich) in 800 mL of water, and stirred until completely dissolved;
- it was added HCl (pH 2, 0.1 M) drop by drop and continuously measuring the pH until reached 7.4;
- under continuous stirring, the rest of water was added;
- the pH was controlled and, if necessary, adjusted with HCl as previously done until the pH is 7.4.

For MBGs samples, at every time point (3h, 1 day, 3 days, 7 days), each Falcon was centrifuged for 5 minutes at 10,000 rpm to induce the powder precipitation and allow the collection of 10 mL of supernatant. 10 mL of fresh Tris HCl buffer was then added. For HA samples, instead, the procedure was the same, but the analysed time points were (3h, 1 day, 3 days, 7 days, 14 days, 21 days).

The strontium ion concentration was then measured by the inductively coupled plasma atomic emission spectrometry technique (ICP-AES) (ICP-MS, Thermoscientific, ICAP Q, Waltham, MA, USA) after proper dilutions. Analyses were conducted in triplicate and the results reported as the mean ± standard deviation.

The proposed dilutions were:

*Table 20: Dilutions for ICP analysis.*

Sample	Dilution
MBG_SD_10%Sr MBG_SG_10% Sr	1:2
HA_50%Sr HA_100%Sr	1:2

### 3.2.6 Tensile testing

The tensile test is useful for the determination of tensile properties of the specimens. The utilized machine was the Shimadzu 1kN test machine (Fig. 33) located in “Laboratory G15”, Stephenson Building, at Newcastle University. This test is used for the determination of yield point (load that the material can stand before plastic deformation occurs), tensile strength (maximum load that the material can endure before the break), elongation at break and other properties.<sup>118</sup>



Figure 33: Shimadzu 1kN testing machine in G15 laboratory.

Specimens are subjected to a quasi-static load under increasing uniaxial tensile loading until the fracture. The specimen is clamped and the elongation  $\Delta L$  (on the horizontal axis) is measured as a function of the tensile force  $F$  (on the vertical axis). The data were acquired by *TrapexiumX* software. A curve example is presented in figure 34. Great importance needs to be given to some testing parameters, as deformation rates and specimen dimensions, to obtain reproducible and reliable results.<sup>119</sup>

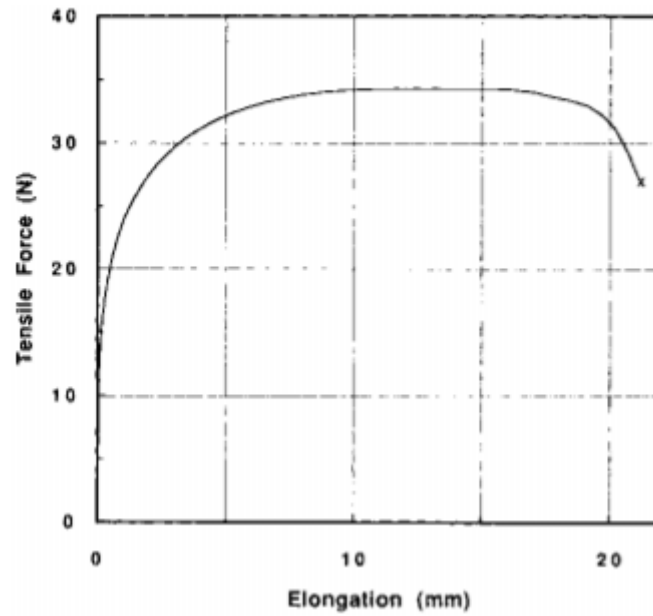


Figure 34: Example of tensile – elongation curve from a tensile test for a ductile material.<sup>120</sup>

Engineering stress,  $\sigma$ , is defined as follows:<sup>120</sup>

$$\sigma = \frac{F}{A_0}$$

where  $A_0$  is the initial cross-sectional area. The sample is cylindrical so, the cross-sectional area can be calculated as:

$$A = \frac{\pi D^2}{4}$$

where  $D$  is the sample diameter, in millimetres.

Engineering strain,  $\varepsilon$ , is defined as:

$$\varepsilon = \frac{\Delta L}{L_0}$$

where  $L_0$  is the initial length and  $\Delta L$  ( $L - L_0$ ) is the change in length.<sup>120</sup>

The linear part of the curve in figure 34, is associated with the elastic deformation, and the slope is a measure of the sample stiffness. This parameter is named elastic modulus,  $E$ , or Young's modulus:

$$E = \frac{\sigma_{el}}{\varepsilon_{el}}$$

The experimental conditions were:

*Table 21: Experimental conditions for tensile test.*

<b>Parameter</b>	<b>Data</b>
Temperature	RT (25 °C)
Speed	30 mm/min
Fibre length	320 mm
Gauge length	25 mm



*Figure 35: Example of the grip used to hold the filaments.<sup>121</sup>*

### 3.2.7 Rheological characterization

Rheology is defined as the study of the flow and deformation of matter which describes the interrelation between force, deformation and time.<sup>122</sup> Rheology relates on the behaviour of complex visco-elastic materials that display both elastic (the material strains when stretched and immediately returns to the original state once the stress is removed) and viscous properties (the material resists shear flow and strain linearly with time). The main parameters that defines rheological studies are viscosity (the measure of the material's resistance to a deformation), complex shear modulus (given by the relation between the complex tension and deformation), and also shear stress, shear strain and shear rate, as will be defined in the next paragraph.

One basic type of flow is defined as shear flow, in which the fluid components past one another with every layer moving faster than the one beneath (Fig. 36). The top layer has the highest velocity, while the bottom layer is stationary. The main relationships between the physical parameters involved (force, unit area and geometry of the sample) are expressed in figure 36:

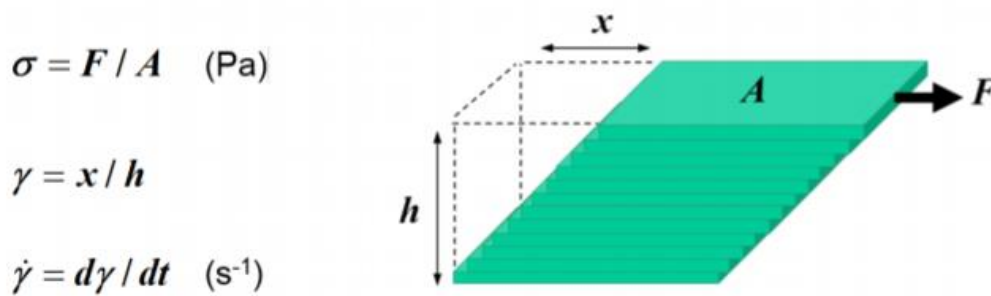


Figure 36: Quantification of shear rate and shear stress for layers of fluids sliding over one another.<sup>122</sup>

where  $\sigma$  is defined as shear stress, the force acting over a unit area,  $\gamma$  is shear strain, the displacement gradient across the sample. The shear rate,  $\dot{\gamma}$ , is the change rate of strain with time. When a shear stress is applied to a fluid, there is a transfer of momentum through the layers of fluids by collisions and interactions with other fluid components. This leads to a reduction in fluid velocity and kinetic energy; the coefficient of proportionality between the shear stress and shear rate is defined as dynamic viscosity ( $\eta$ ).<sup>122</sup>

$$\eta = \frac{\sigma}{\dot{\gamma}} \quad (\text{Pa s})$$

If  $\eta$  is independent from shear rate or shear stress and its value is constant, the fluid is called Newtonian. In this type of fluid, an infinitesimal shear stress will initiate flow and the shear stress is directly proportional to shear rate. The flow curve, at given temperature and pressure, is linear and passes through the origin.<sup>123</sup>

When  $\eta$  depends on shear rate or shear stress, the fluid is called non-Newtonian (Fig. 37). The most common type of non-Newtonian behaviour is shear thinning or pseudoplastic flow, in which the fluid viscosity decreases with increasing shear rate. An infinitesimal shear stress can initiate flow, meaning that the curve passes through the origin. This type of behaviour can be explicated by the micro-structural rearrangements that occur in the fluid when is subjected to an applied shear. In fact, at low shear rates, materials tend to maintain an irregular order caused by the strong interactions between molecules and particles. When the shear rate is high enough, the structure can be rearranged in its orientation, aligning with the flow, hence decreasing the molecular interactions. On the contrary, shear thickening (or dilatant) behaviour exhibits an increase in the viscosity according to the increase in shear rate (Fig. 37). In the case of polymers, usually amphiphilic, at high shear rates the molecular chains may open-up and stretch, exposing parts of the chains able of forming transient intermolecular associations.<sup>122,123</sup> Another example of dilatant system is a highly concentrated suspension: for low applied forces the particles within the material are able to re-organize and adapt according to the flow direction. In such conditions, the viscosity of the material is low. For high forces, instead, the particles tend to create agglomerates, then opposing themselves to the flow, and producing an increase in viscosity.

If a fluid presents a yield stress  $\tau_y$  can be defined as viscoplastic. For stresses below yield stress, the shear rate remains zero, while for higher stresses the fluid flows with a shear rate dependent on the excess stress  $(\tau - \tau_y)$ . Bingham plastic behaviour exhibits a linear relationship between the shear stress in excess of the yield stress  $\tau_y$  and the resulting shear rate. Both the curves described does not pass through the origin of the axis; viscoplastic curve has the same shape of a shear-thinning fluid, while for Bingham plastic behaviour the curve is linear (Fig. 37). Yield stress can be possessed by both polymeric and particulate systems. Polymers show a yield stress in case of cross-linked structures, polymeric gels or filled systems. In the case of suspensions, the yield stress can be explained by particle-particle frictional interactions.<sup>123</sup>

The previous cases are time-independent, meaning that original viscosity can be reached when the shearing force is removed. If the recovery process is time-dependent, the fluid can be considered thixotropic. This type of behaviour is characterized by a hysteresis loop between the up and down curve. On the contrary, the fluid can be considered rheopectic if exhibiting a time-dependent increase in viscosity. As the fluid undergoes shearing forces for longer, the higher becomes the viscosity.<sup>122</sup>

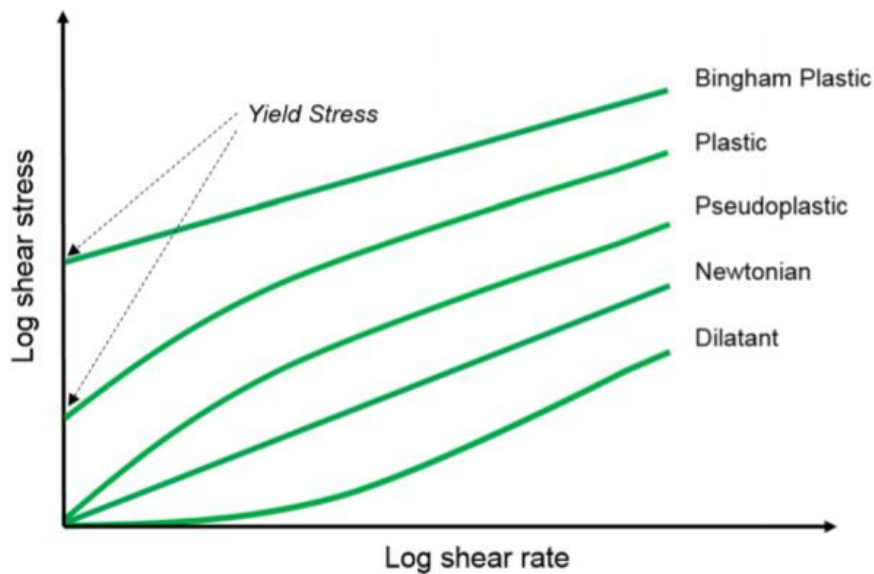


Figure 37: Shear stress/shear rate plots depicting various types of flow behaviours.<sup>122</sup>

It was previously introduced the complex shear modulus. It can be defined as the complex sum of the elastic and viscous components of the material, which will be represented by the elastic modulus ( $G'$ ) and viscous modulus ( $G''$ ). The elastic modulus, also called storage modulus, is calculated as the ratio between the elastic stress and applied strain. The viscous, or loss modulus, represents the relationship between the viscous stress and deformation.

It is important to test the material and assess the previously defined properties within the linear visco-elastic region (LVER), where stress and strain are proportional and that can be defined by means of a stress or strain sweep test. Those tests can detect the point at which the structure begins to yield. Outside the visco-elastic region, non-linearity appears, and the measurements can no longer be easily correlated with microstructural properties. Practically, the excessive strain disrupts the network structure, and non-linearity arises when the moduli are declining, hence the system will become more fluid-like.<sup>122,124</sup>

In this study, the rheological analyses were conducted by using a DHR-2 controlled stress rotational rheometer (TA Instruments, Waters, New Castle, DE, USA), shown in figure 38. Frequency sweep tests were performed on material samples in order to investigate the variation of the visco-elastic properties according to the different stress frequencies applied.

The tests were conducted using a 25 mm diameter parallel plate geometry. A constant temperature of 220 °C was applied during the test thanks to the presence of an environmental test chamber (ETC oven). The temperature was set at 220 °C because it is the chosen temperature for the subsequent extrusion process for the device production. The test was performed at a constant strain of 1 %, while the frequency of the applied sinusoidal stress was varied between 1 and 600 rad/s. Extruded pure PLLA, PLLA\_MBG\_SD\_10%Sr,

PLLA\_MBG\_SG\_10%Sr, PLLA\_HA\_0%Sr, PLLA\_HA\_50%Sr and PLLA\_HA\_100%Sr were all analysed. Before starting the analysis, each sample was cut in 2-3 mm fragments and placed within a metallic guide to avoid material dispersion. After waiting for the polymer melting, the measure gap was properly set (between 500 and 1000  $\mu\text{m}$ ), removing the excess material. Each sample was used for only one test.



Figure 38: Left: DHR-2 rotational rheometer. Right: Detail of the 25 mm parallel plate geometry.

The frequency sweep resulted in the plotted values of  $G'$  and  $G''$  as a function of the variation in the stress frequency. The flow ramp of the material and specifically the variation of material viscosity with increasing shear rates was consequently obtained thanks to the Cox-Merz equation. According to this equation, complex viscosity as a function of frequency can be seen as an analogy between steady and oscillatory shear.<sup>125</sup>

$$\eta(\gamma) = \eta^*(\omega), \quad \gamma = \omega$$

This relation cannot be applied to all systems. In fact, it fails in front of particulate dispersions, cross-linked or gelled systems. Instead, it works for almost all concentrated or semi-dilute solution and polymer melts. At high frequencies, the oscillatory data can either over- or underestimate the steady state data.<sup>126</sup>

The main objective of the rheological measurements is to evaluate through frequency sweep tests the change in material's properties as the stress frequency varies, in order to assess its physical state at a given value of frequency. These tests provide information about the material's strength, also related to the molecular weight of the polymer. Then, from the data of the frequency sweep, applying Cox-Merz equation, it is possible to obtain flow ramps, identifying the relationship between the material's viscosity and shear rates. The results of the flow ramp tests will give information about the material's printability, then allowing to assess the suitable range of viscosity that would guarantee the best results in the extrusion process.

## 4 – Results and discussion

### 4.1 Characterization of mesoporous bioactive glasses containing strontium ions

#### 4.1.1 MBG containing strontium ions: aerosol-assisted spray-drying process (MBG\_SG\_10%Sr)

The particle morphology was evaluated through FESEM (Fig. 39). The particles are spherical, and most appear to have diameters comprised between 0.5 and 5  $\mu\text{m}$ .

The surface is smooth, and the morphology appears not greatly affected by the strontium ions incorporation. This result is in fair agreement with other works in the literature in which the ion substitution was lower (e.g. 2-4%).<sup>127</sup>

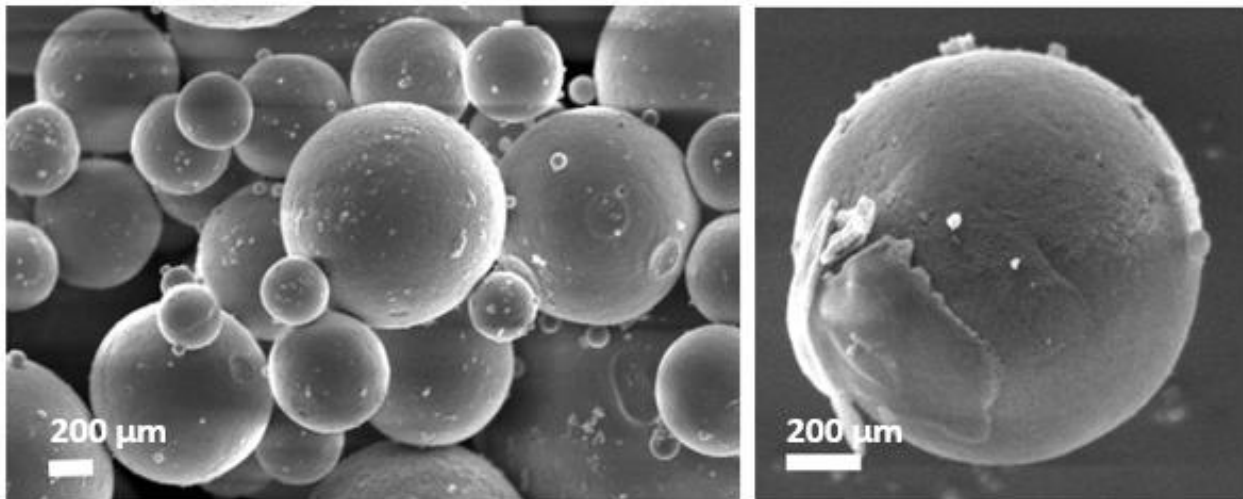


*Figure 39: FESEM micrographs of MBG\_SD\_10%Sr sample.*

The advantages of spray-drying technique are numerous: the process is rapid, fully automated (consenting the control of many parameters simultaneously) and allows high precision control over particle size, bulk density, degree of crystallinity and residual solvents.<sup>128</sup>

Table 22 summarizes the relationships between the spray-drying parameters and their influence over the final result.

Table 22: Relationships between spray-drying parameters.<sup>105</sup>

<b>Parameter</b>	<b>Outlet temperature</b>	<b>Particle size</b>	<b>Final product moisture</b>	<b>Efficiency</b>
> Drying air flow rate	↑↑	--	↓↓	↑↑
> Air humidity	↑	--	↑↑	↓
> Inlet temp	↑↑↑	--	↓↓	↑
> Atomizing air flow	↓	↓↓↓	--	--
> Feed rate	↓↓	↑	↑↑	↑↓
> Solid concentration in feed	↑↑	↑↑↑	↓	↑
Organic solvent (instead of water)	↑↑↑	↓	↓↓↓	↑↑

The EDS analysis (Fig. 40) shows all characteristic peaks of the particle elements (silicon, calcium and strontium), and the estimation of the atomic and weight percentages are recorded in Table 23. Chromium peaks are related to the coating of samples, needed for observation.

The presence of Sr within the sample confirms that the synthesis is successful, and the strontium is incorporated within the matrix.

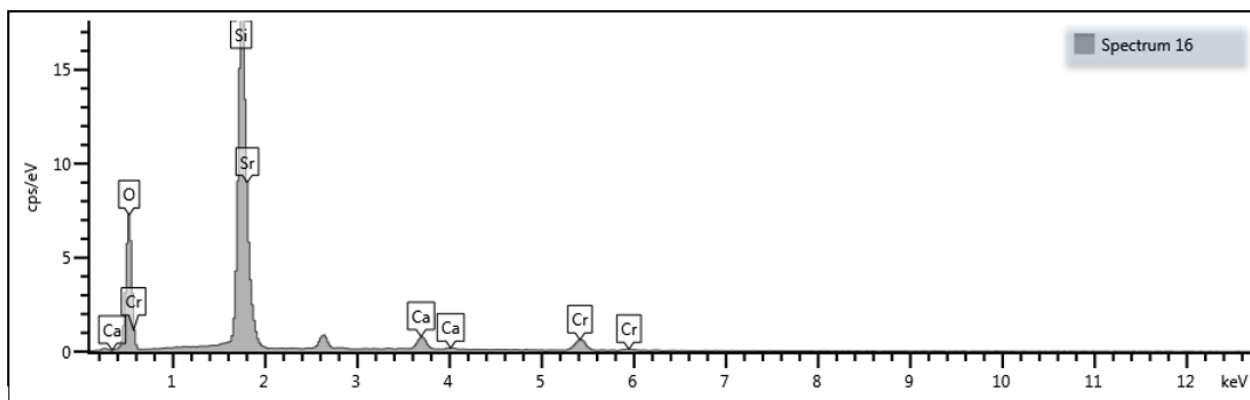


Figure 40: EDS spectrum of MBG\_SD\_10%Sr sample.

Table 23: Weight and atomic percentage of the elements in MBG\_SD\_10%Sr sample.

Element	Wt %	Atomic %
O	48.00	66.14
Si	36.12	28.79
Ca	3.12	1.87
Sr	12.76	3.20
Total:	100.00	100.00

The adsorption-desorption analysis is reported in figure 41, which shows the adsorption curve (blue) and the desorption one (red). The curve represents a Type IV isotherm with a pronounced H2 hysteresis loop, typical of mesoporous materials containing both open and partially blocked mesopores.<sup>109</sup> The hysteresis is pronounced and could be due to the complex pore network experiencing the blocking of the pores connected to the external surface at lower vapour pressures.<sup>127</sup> The spray-drying process is extremely quick, then both the time available for mesophase organization and silica condensation are limited. As a consequence, the mesostructured network appears without long-range organization, nevertheless the obtained isotherm confirms the mesoporous structure of the synthesised particles.

The pore size and size distribution are obtained by performing a DFT algorithm on the desorbing isotherm (Fig. 42), and the estimated values combined in Table 24. The analysis reports a wide range of pores, with diameter ranging from 6 nm to 10 nm. Smaller pores are also observed, mainly around 3 nm. As reported by Yan et al.<sup>39</sup>, the smallest pores can be linked to the size of one-dimensional channels developed within the structure, while bigger pores can be associated to the occurrence of the interconnected meso-channels. Specific surface area is around 220 m<sup>2</sup>/g while pore volume is around 0.3 cm<sup>3</sup>/g. The pore size obtained with this synthesis is coherent with other studies. Wu et al.<sup>31</sup> describes that the structure-directing agents plays an important role in influencing the mesopore structure, mesopore size, surface area and pore volume of the

developed MBGs. The average parameters in case of Pluronic P123 as structure-directing agent are 300-500 m<sup>2</sup>/g for surface area, 3.5-7 nm for pore diameter and 0.4-0.75 cm<sup>3</sup>/g for pore volume.

The particles obtained from this work display lower values than the typical spray-drying synthesis performed with P123, and it could be related to the partial strontium ions substitution. In fact, it is already stated in literature that the substitution of increasing amount of strontium affects the structural properties of the mesoporous particles. Previous studies demonstrated that an increased incorporation of ions as strontium or trivalent elements as Ce, leads to a reduction of specific surface area and pore volume because of the appearance of disorganized non-porous domains.<sup>127</sup> Therefore, an ion substitution of 10% molar could be the reason behind the limited values obtained from the present evaluations.

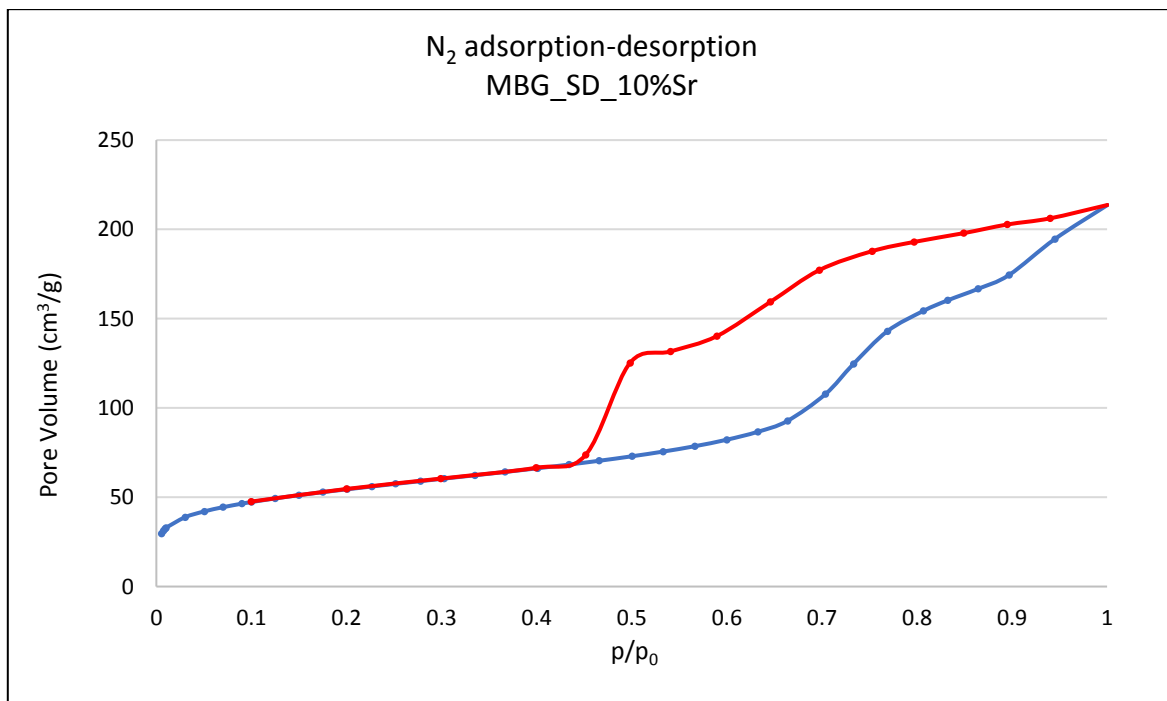


Figure 41: N<sub>2</sub> adsorption-desorption isotherm of MBG\_SD\_10%Sr sample.

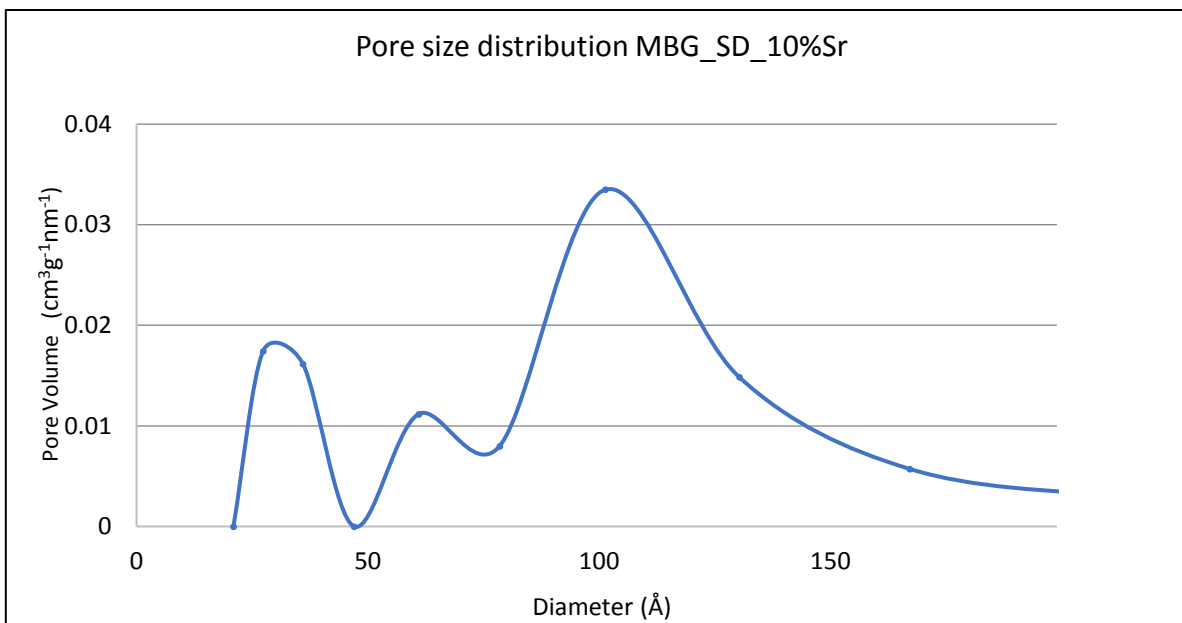


Figure 42: Pore size distribution of MBG\_SD\_10%Sr sample.

Table 24: Results of the BET analysis from MBG\_SD\_10%Sr sample.

<b>MBG_SD_10%Sr</b>	
Specific surface area	217 m <sup>2</sup> /g
Average pore size	6.6 nm
Pore volume	0.3 cm <sup>3</sup> /g

The release test is conducted as described in chapter 3, section 3.2.5, and the results are plotted in figure 43. According to the data obtained, a high amount of strontium is immediately released after 3 hours and is over the 90% of the total incorporated ions. For longer release time, it can be seen that the released ion concentrations are not significantly increasing, and at day 7 the released ions are close to 95%. Then, it can be stated that almost the totality of the ions is released from the mesoporous structure in 7 days. From that data, it can be determined that the release kinetic is limited to an initial ‘burst release’, due to the high specific surface area of the mesoporous particles and the fast ionic exchange reactions occurring at the surface. Theoretically, burst release can be ascribed to low bonds between the matrix and the incorporated load. In this case instead, the bond between the mesopore structure and strontium ions is ionic, then characterized by a high strength. The described release behaviour can be linked to the pore size, larger than the strontium ionic diameter, the high surface area and accessible internal pore volume. Those aspects can then facilitate the diffusion of ions, especially those facing the pore entrance. Only a little percentage of strontium ions remain within the mesoporous structure, probably due to a partial dissolution and re-precipitation of the micellar structure during the synthesis. According to the discussed result, it can be concluded that the developed

mesoporous matrix has an interconnected structure able to quickly release the incorporated ions towards the medium.

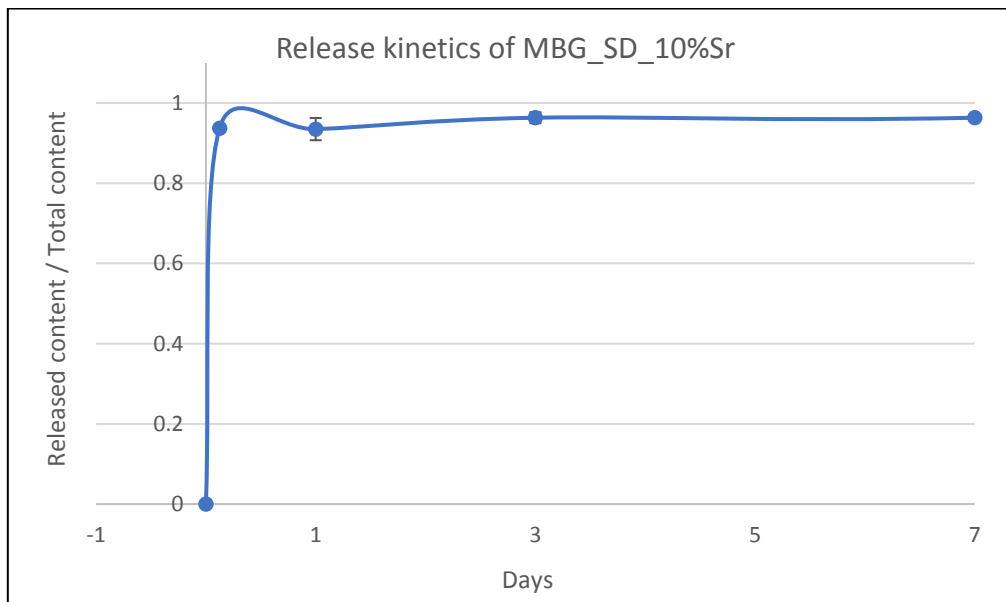


Figure 43: Release kinetics of strontium from the MBG\_SD\_10%Sr in Tris-HCl buffer at 37°C and pH 7.4. The results are expressed as average  $\pm$  standard deviation.

#### 4.1.2 MBG containing strontium ions: sol-gel synthesis in basic medium (MBG\_SG\_10%Sr)

The particles' morphology was evaluated through FESEM (Fig. 44).

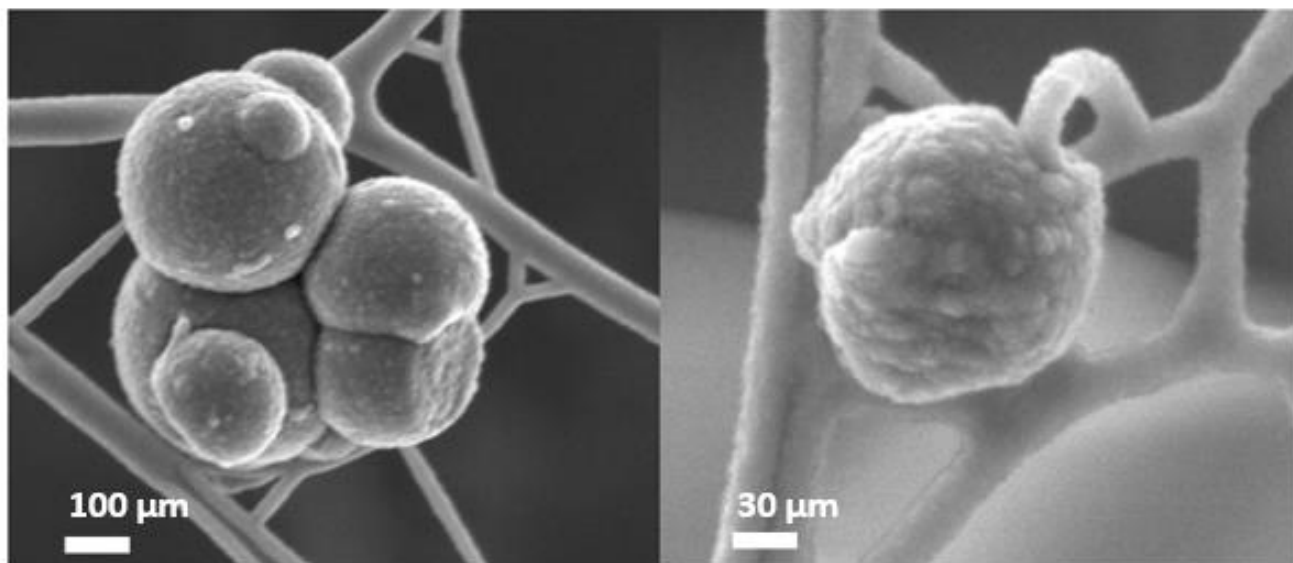


Figure 44: FESEM micrographs of MBG\_SG\_10%Sr sample.

The figure shows the presence of spheroidal particles, in the range of 200 nm and 300 nm and a slight agglomeration can be observed. As before seen for MBG\_SD\_10%Sr sample, the strontium substitution did not affect the particle morphology, if compared to other studies in which the strontium ions were added in lower concentrations or totally absent.<sup>127</sup>

EDS analysis (Fig. 45) presents the characteristic peaks for the particle elements (silicon, oxygen, calcium and strontium), while Table 25 records the estimation of their atomic and weight percentages. Chromium peaks are related to the coating of samples, needed for observation.

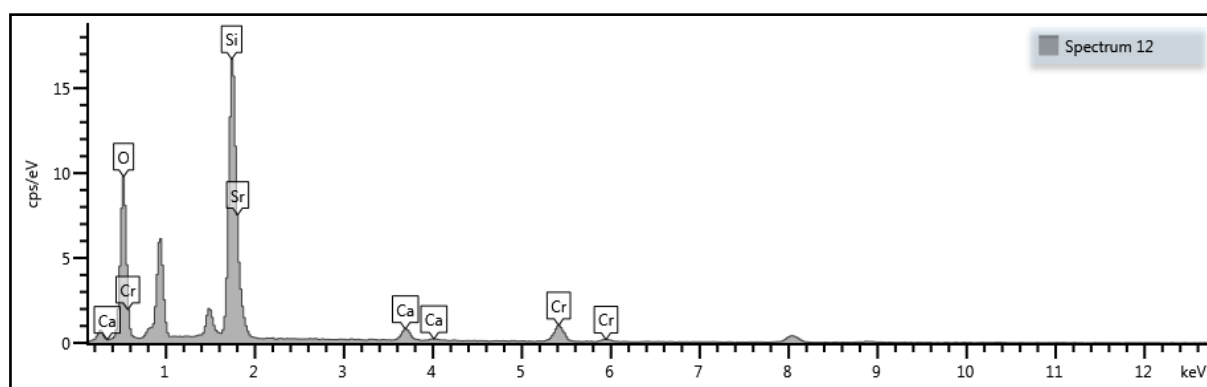


Figure 45: EDS spectrum of MBG\_SG\_10%Sr.

Table 25: Weight and atomic percentage of the elements in MBG\_SG\_10%Sr sample.

Element	Wt%	Atomic %
O	55.07	72.03
Si	32.87	24.49
Ca	2.12	1.11
Sr	9.93	2.37
Total:	100.00	100.00

The presence of Sr in the sample confirms that the synthesis is successful, and the strontium is incorporated within the framework.

The adsorption-desorption analysis is reported in figure 46, which shows the adsorption curve (blue) and the desorption one (red). The curve represents a Type IV isotherm with a H2 hysteresis loop, less pronounced compared to the sample prepared by spray-drying. The reason can be ascribed to smaller pore dimensions, close to the lower limit that can allow the formation of a hysteresis loop. The limit, as stated by Cychoz et al.<sup>129</sup>, is 4 nm, around the average pore diameter of the particles produced with this type of synthesis.

Nevertheless, despite this, the presence of a hysteresis loop still indicates that the obtained structure is mesoporous.

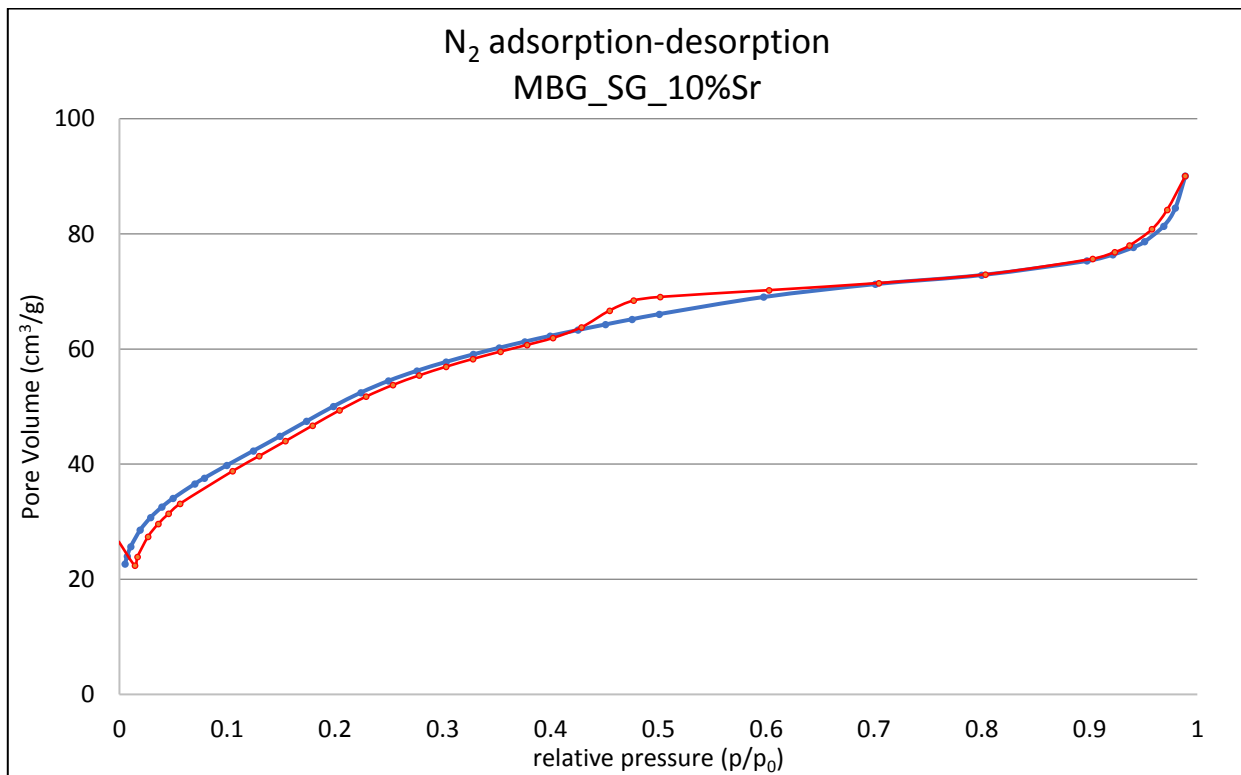


Figure 46: N<sub>2</sub> adsorption-desorption isotherm of MBG\_SG\_10%Sr sample.

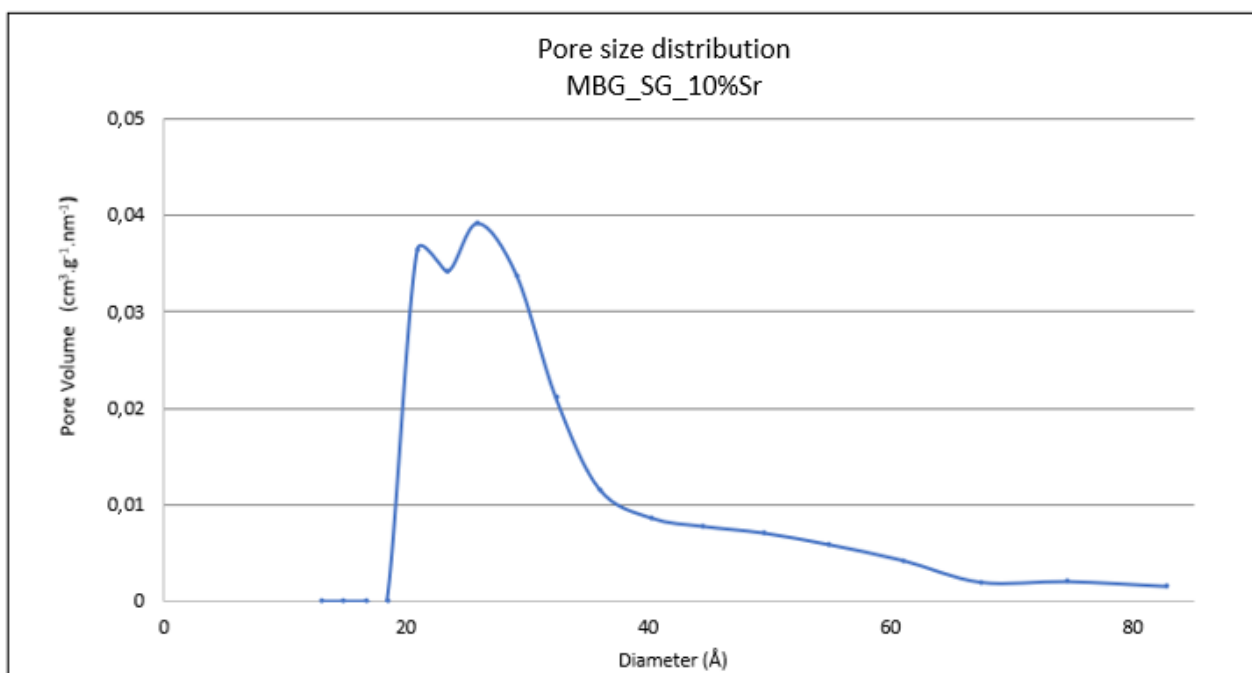


Figure 47: Pore size distribution of MBG\_SG\_10%Sr sample.

The pore size and size distribution are obtained by performing a DFT algorithm on the desorbing isotherm (Fig. 47), and the estimated values combined in Table 26. The analysis reports a wide range of pores with dimension around 2-3 nm. Pores with greater dimensions, until 6 nm, are also present. Specific surface area is around 190 m<sup>2</sup>/g and pore volume is estimated around 0.13 cm<sup>3</sup>/g. The structure-directing agent in this case is CTAB, which generates mesoporous structures with pore size around 2-3 nm.<sup>31</sup> Moreover, the typical values for specific surface area and pore volume of mesoporous structures synthesised by CTAB are averaged at 450 m<sup>2</sup>/g and 0.57 cm<sup>3</sup>/g, respectively, without strontium incorporation. The features obtained in the present work are lower than typical values in case of CTAB-derived MBGs, but in this case the strontium is added within the formulation. As already stated for MBG\_SD\_10%Sr, the presence of additional ions leads to a decrease in the particles' distinctive parameters. Despite this, the obtained values are greatly higher than the conventional sol-gel glasses, determining a higher bioactivity in physiologic environment.<sup>127</sup>

Table 26: Results of the BET analysis from MBG\_SG\_10%Sr sample.

<b>MBG_SG_10%Sr</b>	
Specific surface area	189 m <sup>2</sup> /g
Average pore size	3.3 nm
Pore volume	0.13 cm <sup>3</sup> /g

The release test (Fig. 48) is conducted in Tris-HCl buffer and it is displayed a burst release after 3 hours, followed by a plateau. Compared to MBG\_SD\_10%Sr sample, the ion release in this case is slower. After 3 hours it is released only the 60% of the incorporated ion (deeply lower than the spray-dryer synthesis, where after 3 hours the released ions are above 90%). As time passes, the release continues until the 95% of the incorporated ions leave the network. Similarly, as MBG\_SD\_10%Sr, the burst release can be explicated through the high surface area and the accessibility of medium into the porous structure. The slower release, instead, can be related to the silica dissolution and subsequent re-precipitation, then causing the blocking of the smaller mesopores.

Comparing the release kinetics of MBG\_SD\_10%Sr and MBG\_SG\_10%Sr, it can be said that both are able to release in 7 days almost all of the incorporated ions, displaying an initial burst release. The quantity of strontium ions immediately released is diverse between the two samples, with MBG\_SG\_10%Sr exhibiting a lower release (around 60%), if compared to MBG\_SD\_10%Sr (over 90%). Then, at 7 days, both the samples can release up to 95% of the incorporated ions. In the literature, it was confirmed that the released strontium ions are in amount suitable to exert a pro-osteogenic effect.<sup>127</sup>

In conclusion, MBG\_SG\_10%Sr has a more sustained release of ions, which represents a very attractive feature for an implantable device where the osteogenic effect is desirable to last longer.

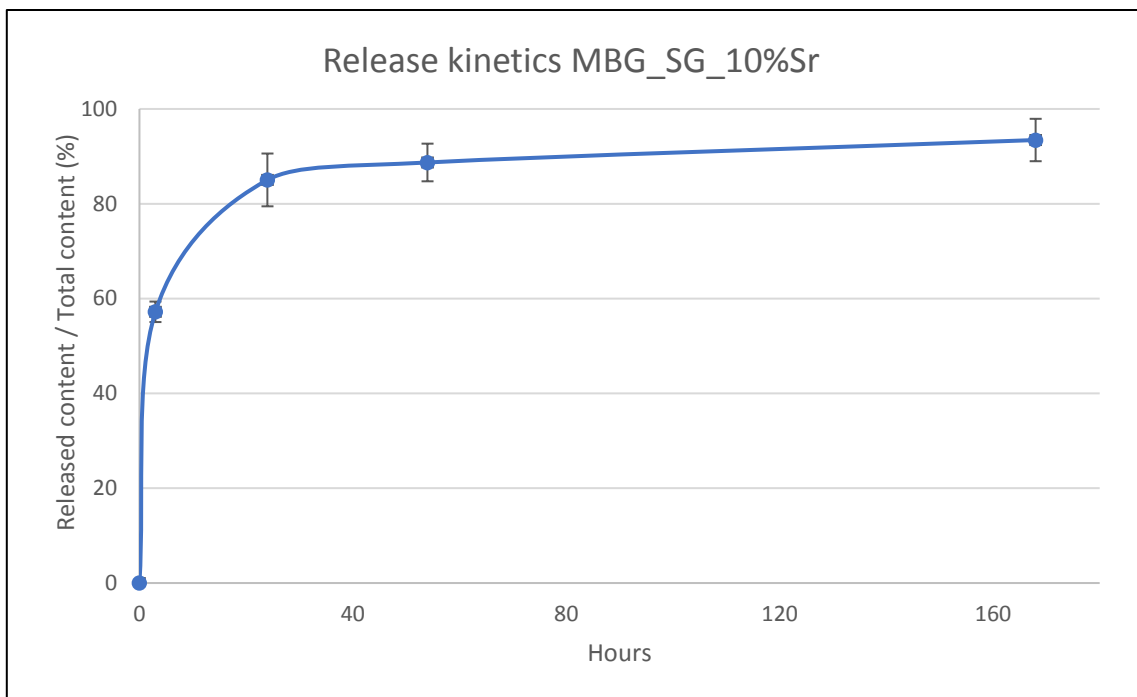


Figure 48: Release kinetics of strontium from the MBG\_SG\_10%Sr in Tris-HCl buffer at 37°C and pH 7.4. The results are presented as average  $\pm$  standard deviation.

## 4.2 Characterization of nano-hydroxyapatites

The hydroxyapatites provided from Fluidinova (Porto, Portugal) are both pure (HA\_0%Sr) and containing different percentages of Sr substitution (HA\_50%Sr and HA\_100%Sr). HA\_50%Sr was provided in powder form, therefore directly characterized. At variance, HA\_0%Sr and HA\_100%Sr were provided in form of water suspension and thus, the evaporation of the solvent was conducted prior the characterization of the powders.

According to the results observed in figure 49, the nano-HA particles appear to be rod-like in shape, with the dimensions increasing proportionally to the amount of strontium content.

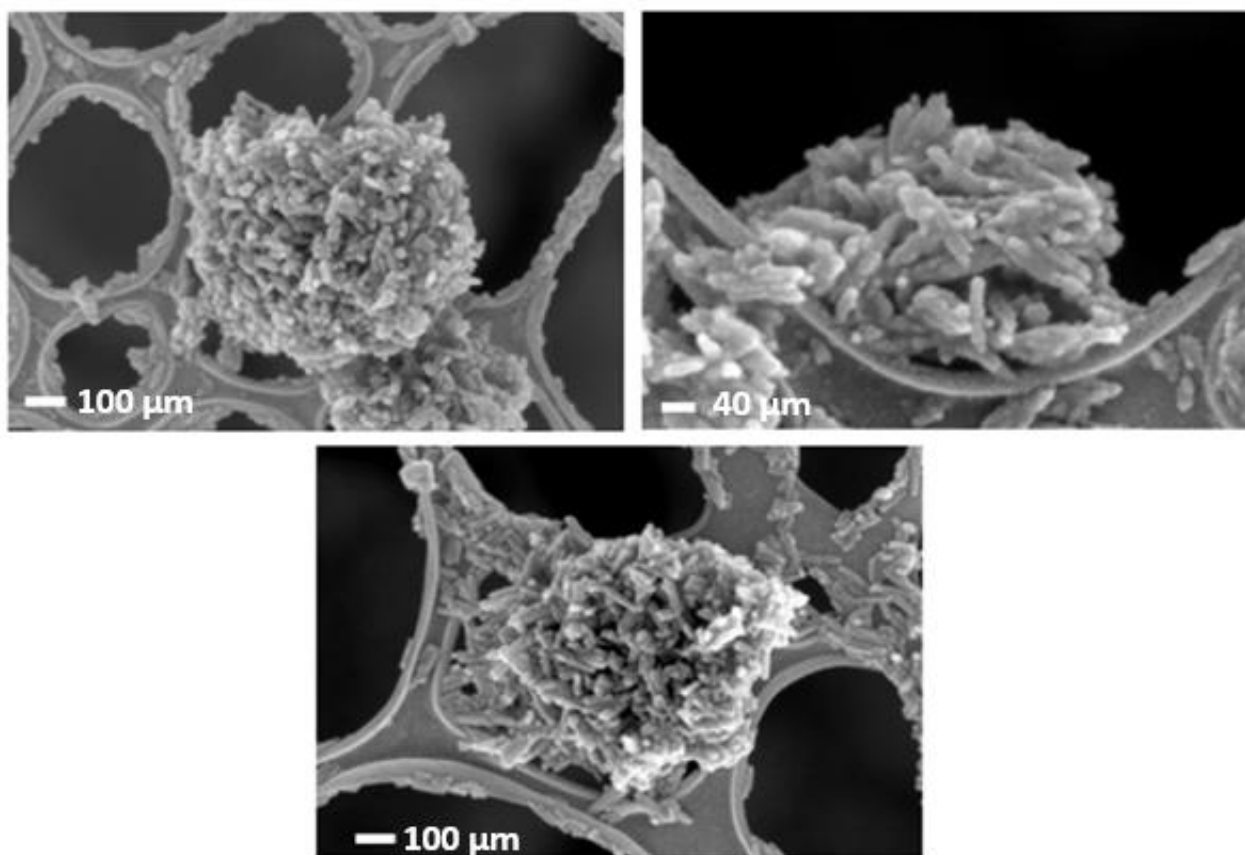


Figure 49: FESEM micrographs of nano-HA. Up left: HA\_0%Sr. Up right: HA\_50%Sr. Down: HA\_100%Sr.

The particles diameter is measured using the software of the instrument, and the dimensions summarized in Table 27. The average dimensions of the nano-HA increases with the higher content in strontium. This increase can be attributed to the larger ionic radius of strontium 1.12 Å, when compared to the calcium ion, 0.99 Å.<sup>130</sup>

The resulting dimensions for pure HA are conforming to other studies, where the obtained needles are 20 - 40 nm in length and 4 - 14 nm in width.<sup>46</sup> Moreover, if compared to human apatite (40 - 60 nm long, 20 nm wide), the dimensions are similar, especially in the case of HA\_100%Sr. This is an indication that the provided HA, in all the presented compositions, are suitable materials for bone tissue engineering approaches.

Table 27: Dimensions of nano-HA samples.

Sample	Length	Width
HA_0%Sr	48 nm	14 nm
HA_100%Sr	65 nm	16 nm

The composition of the different nano-HA is assessed with EDS and the results demonstrate that strontium is effectively incorporated within the framework in HA\_50%Sr and HA\_100%Sr samples. It is investigated the (Ca+Sr)/P ratio and then compared to the stoichiometric ratio in not-substituted hydroxyapatite where the Ca/P ratio is known to be 1.67 (Table 28).<sup>46</sup>

The Ca/P ratio is similar for all samples, with exception of HA\_0%Sr which presents a higher value. For HA\_50% Sr sample the average value is  $1.65 \pm 0.13$ , being the closest one to the stoichiometric apatite.

*Table 28: (Ca+Sr)/P ratio calculated from EDS analysis for HA samples.*

Sample	(Ca+Sr)/P	
	Average	Standard deviation
HA_0%Sr	1.83	0.1
HA_50%Sr	1.65	0.13
HA_100%Sr	1.73	0.08

XRD is performed to assess the formation of HA phase despite the substitution of calcium ion by strontium (Fig. 50). The XRD peaks of pure HA are in the same characteristic positions of bone apatite, meaning that the performed synthesis can allow to obtain HA with similar crystallinity properties.

It can be observed that the peaks appear wider for the HA\_50%Sr sample, if compared to the others. This can be attributed to the heterogeneity of the sample, as both calcium and strontium ions are present in the HA composition. In fact, the wide and not defined peaks of the XRD pattern are the demonstration of a less organized crystalline structure. In the case of HA\_100%Sr, the peaks of the spectrum are in the same positions of the typical bone apatite but are higher and more defined. In this case, the obtained HA is characterized by a higher crystallinity.

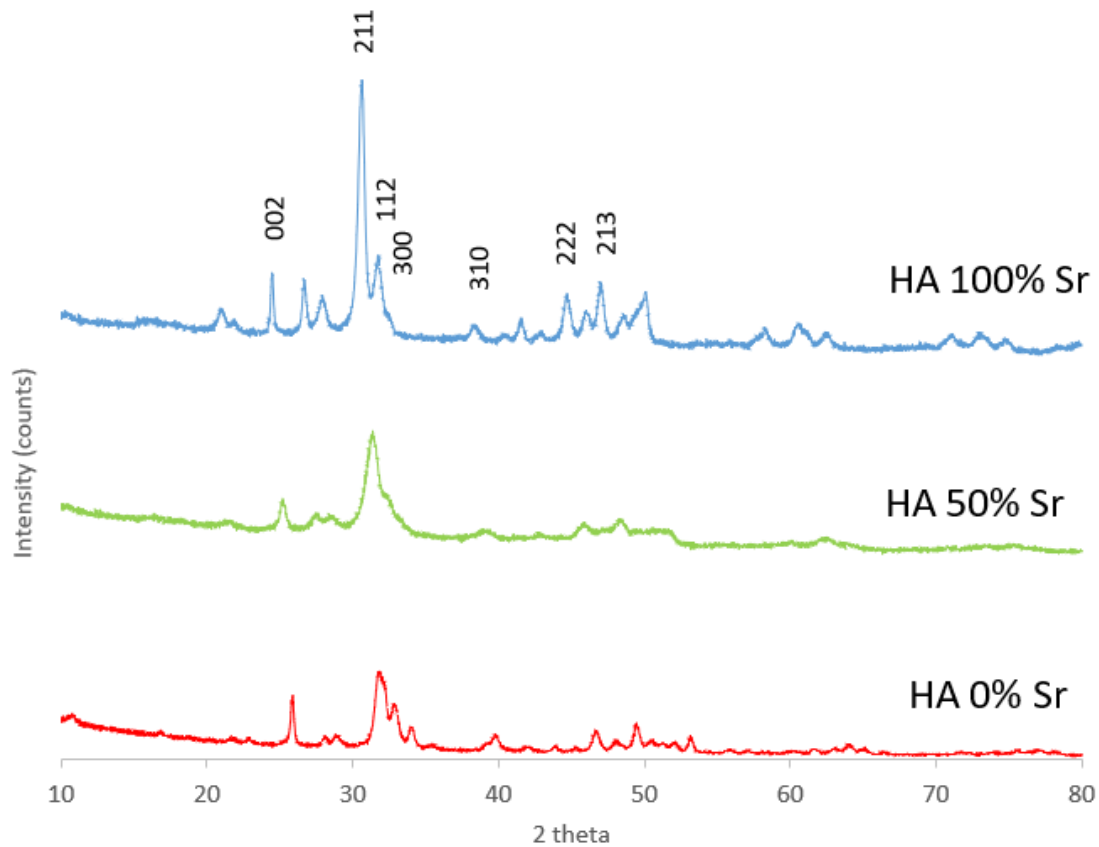


Figure 50: XRD patterns of pure nano-HA (HA\_0%Sr) and substituted HA (50 and 100% Sr ion content).

The release test (Fig. 51) for HA\_50%Sr and HA\_100%Sr is conducted in Tris-HCl buffer and it is displayed a similar behaviour for both samples. In particular, after 1 day, 20% of the incorporated strontium is released from the HA\_50%Sr samples, while the same amounts of ions are released from the HA\_100%Sr sample after 3 days. The release kinetics of strontium ions from the analysed HA particles is relatively slow, as after 21 days, only 45% of strontium is released into the medium. In this case, the slower release rate can be associated with the particle size and the material's heterogeneity. In fact, as a material is characterized by a lower size, it is expected to be more inclined to dissolution because of the high solubility at the interface. This can be main reason behind the lower release of ions in case of HA\_100%Sr sample. Ion release, as already stated, is desired to last as longer as possible to benefit for an extended period of the osteogenic effect of strontium ions, and HA appears to guarantee a controlled release.

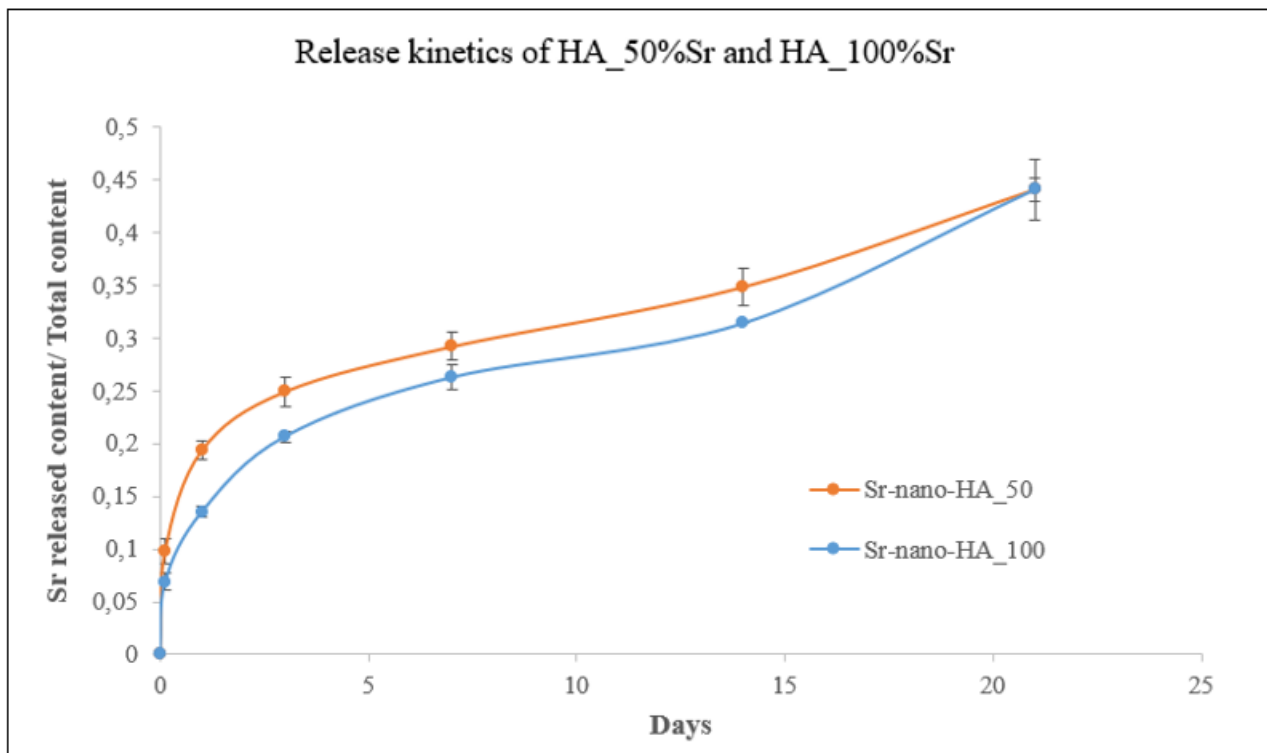


Figure 51: Release kinetics of strontium from HA\_50%Sr and HA\_100%Sr in Tris-HCl buffer at 37°C and pH 7.4. The results are expressed as average  $\pm$  standard deviation.

### 4.3 Characterization of extruded pure PLLA and composite filaments

#### 4.3.1 Morphological assessment of the extruded filaments

Figure 52 presents some of the obtained filaments after the first extrusion process. Figure 52 left presents pure PLLA filament, with average diameter around 1.7 mm. The filaments do not show any impurities or visible defects, presenting a clean surface, smooth and slightly opaque. After the first extrusion, all the tested hybrid formulations appear with a white colouration, sign that the powder incorporation is successful. The formulations based on PLLA\_HA\_0%Sr and PLLA\_HA\_100%Sr are presenting a constant diameter with an average value around 1.6 mm; they appear smooth and without significant defects on the surface. The formulations based on PLLA\_HA\_50%Sr (presented in Fig. 52 right), PLLA\_MBG\_SD\_10%Sr and PLLA\_MBG\_SG\_10%Sr are presenting instead an inconstant diameter and an average value lower than expected, around 1.4 mm. The white colour of the filament suggests that the powder is incorporated within the filament, but the surface is rough. This result can be explained because of the quick melting process that the pellets underwent. In fact, no other thermal processes have been applied to the provided pellets and the molecular weight is extremely high. As the process is quick, it can be supposed that the polymer melting is not

complete and homogeneous in the few minutes spent within the machine's forced path. The extruded material then is not melted enough to leave the die in the desired conditions.

Because of this, the PLLA\_HA\_50%Sr, PLLA\_MBG\_SD\_10%Sr and PLLA\_MBG\_SG\_10%Sr samples were pelletized and underwent a second extrusion process, in order to obtain better quality filaments.

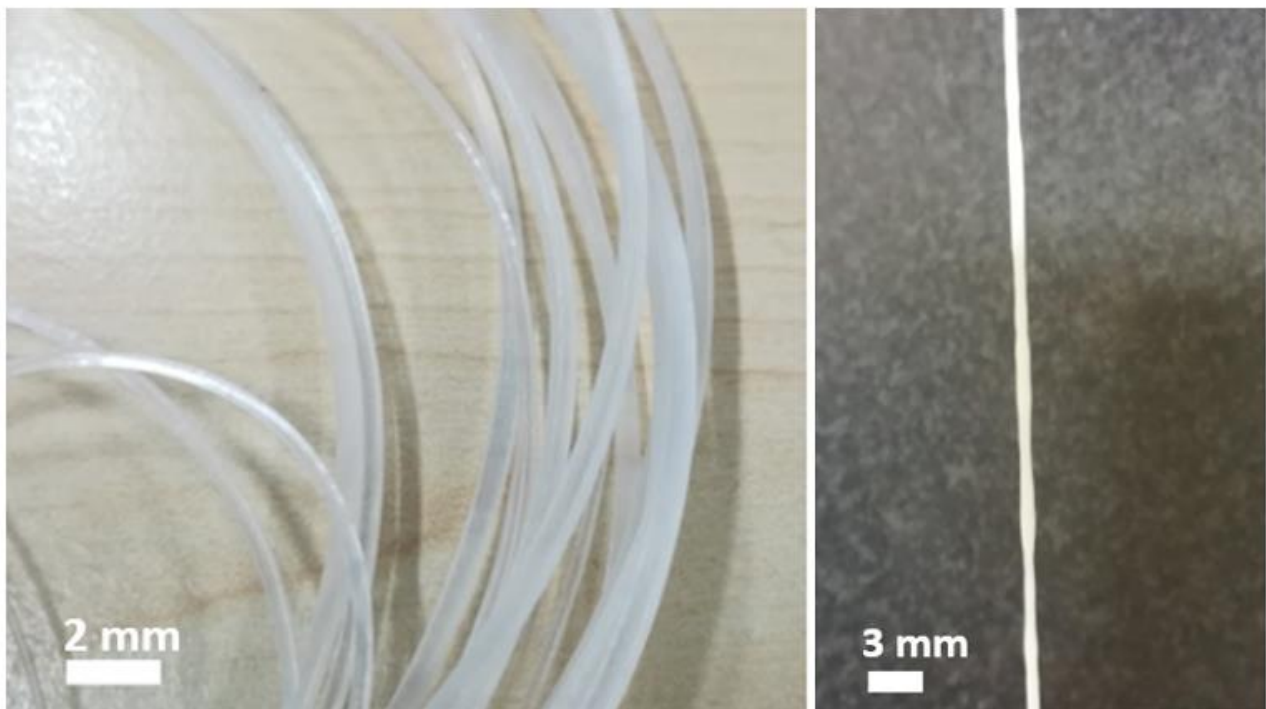


*Figure 52: Left: Pure PLLA filaments after the first extrusion process. Right: Detail of PLLA\_HA\_50%Sr filament after the first extrusion process.*

Figure 53 left presents the PLLA\_MBG\_SD\_10%Sr filaments after the second extrusion process. The average diameter is lower than pure PLLA, around 1.5 – 1.6 mm. The surface appears smooth and without visible defects. PLLA\_HA\_50%Sr and PLLA\_MBG\_SG\_10%Sr samples, which also underwent a second extrusion process, are presenting similar physical features of the displayed PLLA\_MBG\_SD\_10%Sr filaments. All those samples are characterized by a white colouration and an average diameter lower than the desired dimension. The different diameter of the composite filaments (1.5 – 1.6 mm compared to 1.7 mm obtained from pure PLLA sample) is due to the inorganic phase incorporated within the polymeric matrix, as it increases the forces required in the process and increases the melt viscosity. As a consequence, the imposed velocities of the extruder and Haul-Off, despite being adjusted, are too high and the extruded is excessively strained. Other experiments are needed to assess the best working conditions to obtain the desired diameter.

Moreover, the PLLA\_HA\_50%Sr filament, displayed in figure 53 right, presents a slightly brown colouration, sign that the temperatures were too high and burned material can be noticed.

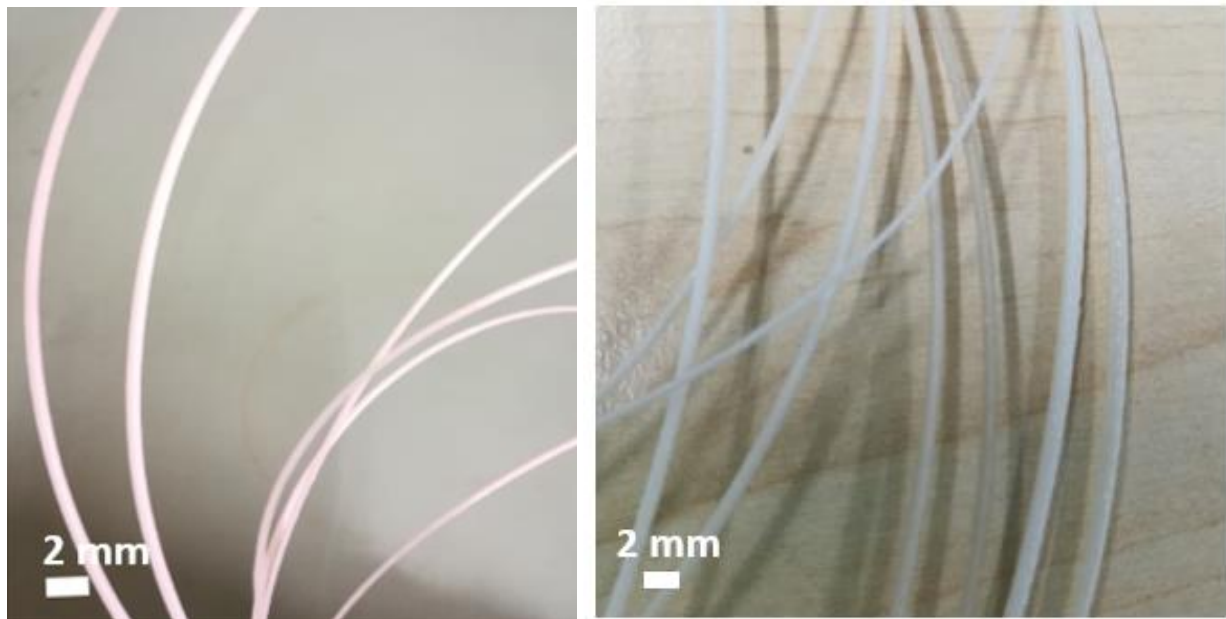


Figure 53: Left: PLLA\_MBG\_SD\_10%Sr filaments after the second extrusion process. Right: PLLA\_HA\_50%Sr filaments after the second extrusion process.

Figure 54 displays the SEM micrographs of the sections of all the performed experiments, pure PLLA and hybrid formulations. All the composites present the inorganic phase within the polymeric matrix, with a homogeneous dispersion. Then, it can be affirmed that both incorporation procedures based on provided and produced HA water suspensions resulted successful. EDS assessments are needed to effectively confront the samples, as will be discussed in the next section.

It can be observed that the dimension of the dispersed inorganic phase appears different, with bigger agglomerates in case PLLA\_HA\_0%Sr and PLLA\_HA\_100%Sr samples and smaller in case of PLLA\_HA\_50%Sr, PLLA\_MBG\_SD\_10%Sr and PLLA\_MBG\_SG\_10%Sr samples. The diverse phase dispersion observable in the filament section can be ascribed to the different processing steps of the composites. In fact, PLLA\_HA\_0%Sr and PLLA\_HA\_100%Sr are extruded once, whilst PLLA\_HA\_50%Sr, PLLA\_MBG\_SD\_10%Sr and PLLA\_MBG\_SG\_10%Sr are extruded twice. The processing can then affect the powder distribution within the polymeric matrix and its accumulation. As already stated, the agglomerates appear smaller in the composites extruded twice, and it can be due to the second processing step, which allows a more uniform powder dispersion and reduces the size of the incorporated phase. To confirm if the processing is the mechanism that mainly affects powder distribution, more studies are needed, to assess the spreading conditions depending on the processing of the material.

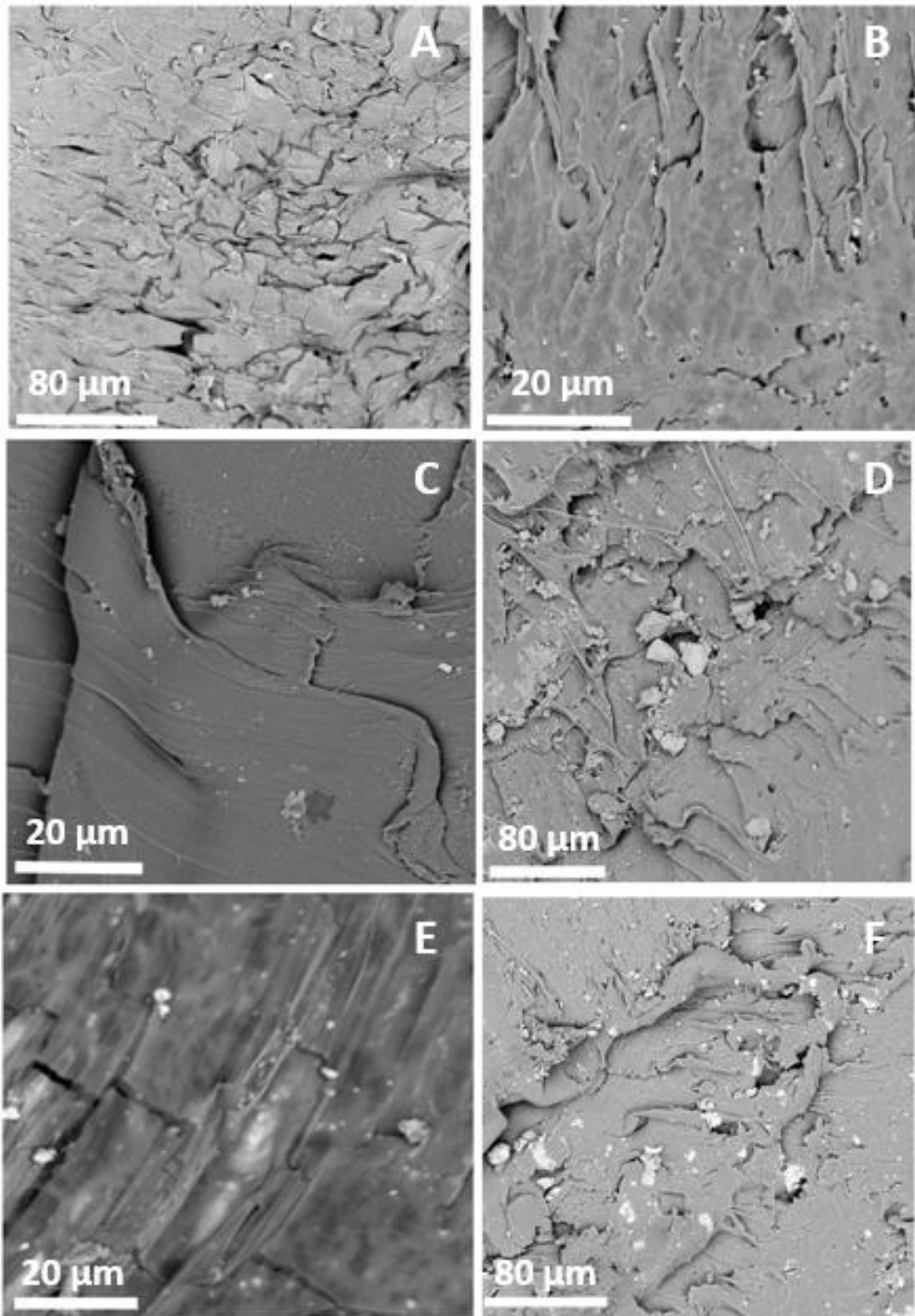


Figure 54: SEM micrographs of the cross-sections of the performed experiments. A: PLLA. B: PLLA\_MBG\_SD\_10%Sr. C: PLLA\_MBG\_SG\_10%Sr. D: PLLA\_HA\_0%Sr. E: PLLA\_HA\_50%Sr. F: PLLA\_HA\_100%Sr.

### 4.3.2 Compositional assessment of the extruded filaments

EDS mapping of the cross-section of pure PLLA filament (Fig. 55) allows to confirm the absence of impurities. As the graph shows, only carbon and oxygen are detected, as expected. The atomic and weight concentration are displayed in Table 29.

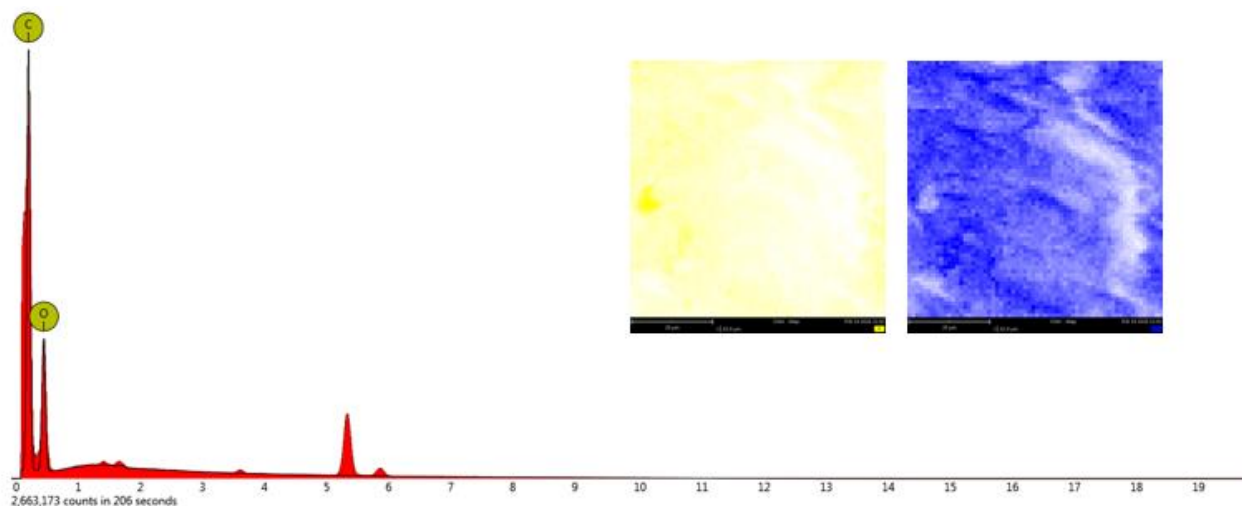


Figure 55: EDS spectrum of PLLA filament. Insert: detail of the element distribution. Yellow represent oxygen and blue represents carbon.

Table 29: Atomic and weight concentration of PLLA sample.

Element	Atomic %	Wt%
O	69.89	75.57
C	30.11	24.43

EDS mapping of PLLA\_MBG\_SD\_10%Sr and PLLA\_MBG\_SG\_10%Sr is performed to assess the presence of the inorganic phase and estimate its distribution (Fig. 56). It can be seen that the inorganic phase distribution is homogeneous within the polymeric matrix, as the uniform colour of silicon and strontium suggest. The uniform colouration over the analysed cross-sectional area confirms that the incorporation is successful for the prepared suspensions. The different powder dispersion between the samples may be directly linked to the utilized inorganic phase. In fact, PLLA\_MBG\_SD\_10%Sr is presenting a paler colour for silicon and strontium, with some dots greatly coloured, indicating in a specific area the presence of higher amount of those elements. PLLA\_MBG\_SG\_10%Sr, instead, is presenting a more intense colour for silicon and strontium over all the analysed area, indicating a more uniform dispersion without excessive differences from one area to another.

Then, the different powder distribution could be attributed to particles' size and surface properties, making the PLLA\_MBG\_SD\_10%Sr particles more disposed to creating agglomerates.

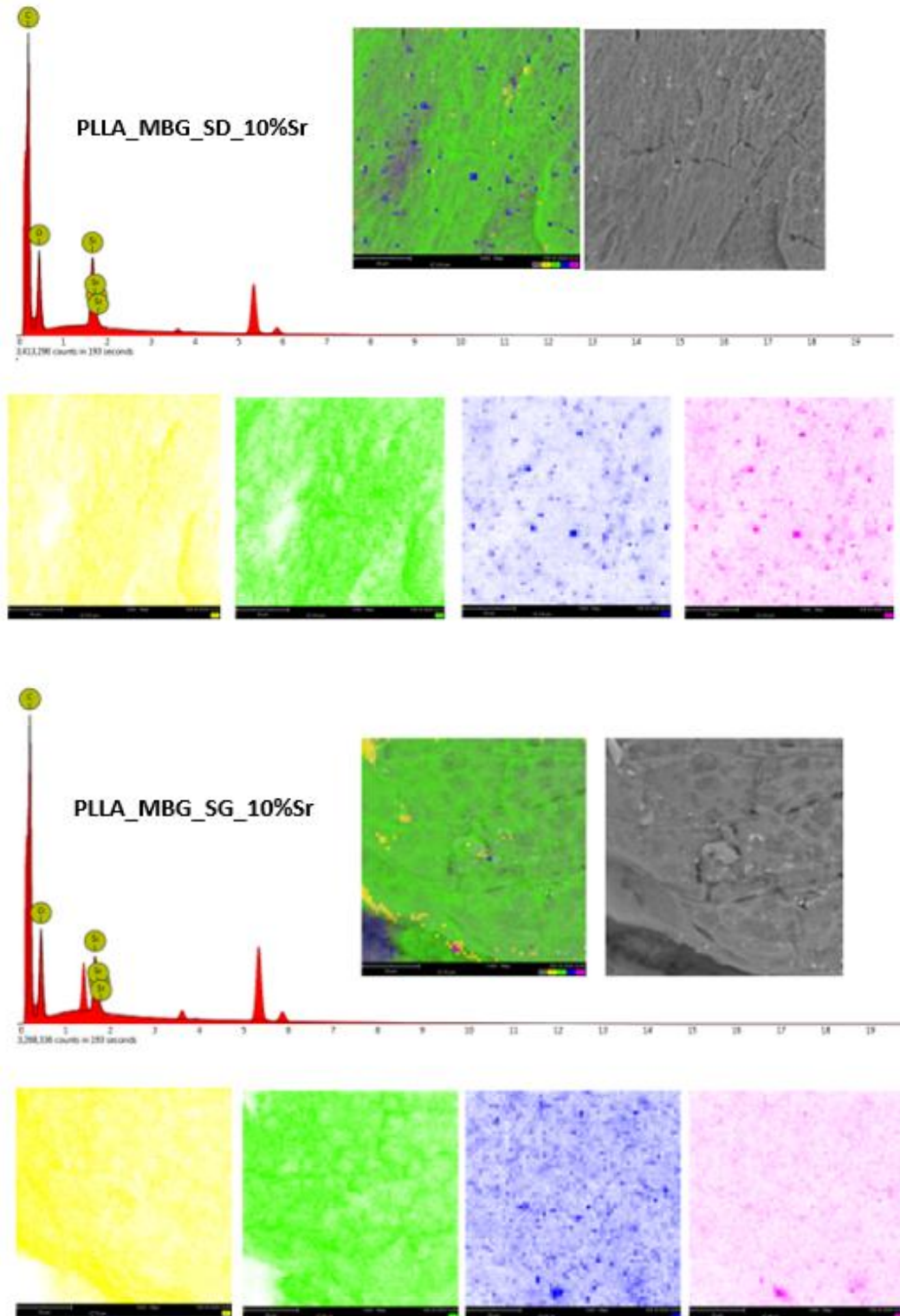


Figure 56: Up: EDS spectrum of PLLA\_MBG\_SD\_10%Sr sample. Insert: detail of the scanned zone. Elemental distribution. Down: EDS spectrum of PLLA\_MBG\_SG\_10%Sr sample. Insert: detail of the scanned zone. Elemental distribution. Yellow represents oxygen, green is carbon, blue is silicon and pink is strontium.

Table 30 presents the atomic and weight concentration of PLLA\_MBG\_SD\_10%Sr and PLLA\_MBG\_SG\_10%Sr sample.

*Table 30: Atomic and weight concentration of PLLA\_MBG\_SD\_10%Sr and PLLA\_MBG\_SG\_10%Sr samples.*

Element	PLLA_MBG_SD_10%Sr		PLLA_MBG_SG_10%Sr	
	Atomic %	Wt%	Atomic %	Wt%
O	55.49	55.93	58.98	59.71
C	36.77	27.82	34.89	26.52
Si	7.06	12.49	5.36	9.53
Sr	0.68	3.77	0.76	4.24

Figure 57 presents the EDS mapping of the cross-sectional area of PLLA\_HA\_0%Sr, PLLA\_HA\_50%Sr and PLLA\_HA\_100%Sr. In the three cases it can be seen that the powder distribution is uniform, as expected from the observations of SEM micrographs (Fig. 54). Some agglomerates are present within the polymeric matrix, as are suggesting the dots displayed in strontium, calcium and phosphorous mapping. It can be supposed that in case of PLLA\_HA\_0%Sr and PLLA\_HA\_100%Sr the powder dispersion seems less uniform, is compared to the previous MBGs cases, as the agglomerates appear bigger. Despite PLLA\_MBG\_SD\_10%Sr also presents more coloured areas, delineating a spot more concentrated in powder content, those seems smaller than PLLA\_HA\_0%Sr and PLLA\_HA\_100%Sr samples. Also, directly confronting PLLA\_HA\_50%Sr and PLLA\_HA\_100%Sr, it can be seen that the colour representing strontium is more uniform over all the detected cross-sectional area in the first case, and not displaying significant differences. As before, this can be linked to the different working process that the samples underwent (one extrusion for PLLA\_HA\_100%Sr and two extrusions for PLLA\_HA\_50%Sr). In fact, as already supposed, the second extrusion process causes a more uniform powder distribution. From the analysed filaments, the greatest uniformity in powder distribution seems to belong to PLLA\_MBG\_SG\_10%Sr sample.

Comparing the alteration in powder content for filaments which underwent the same processing, there is no visible difference between the PLLA\_MBG\_SD\_10%Sr, PLLA\_MBG\_SG\_10%Sr and PLLA\_HA\_50%Sr samples. Despite a higher content in case of HA sample (5%, if compared to 2% of MBG specimens), no significant difference in powder dispersion over the filament section can be noted.

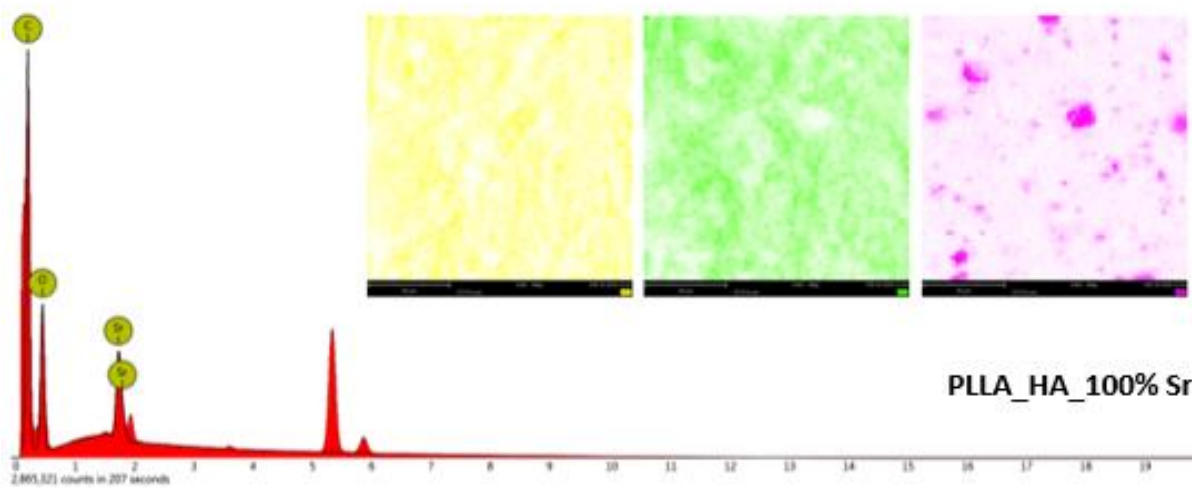
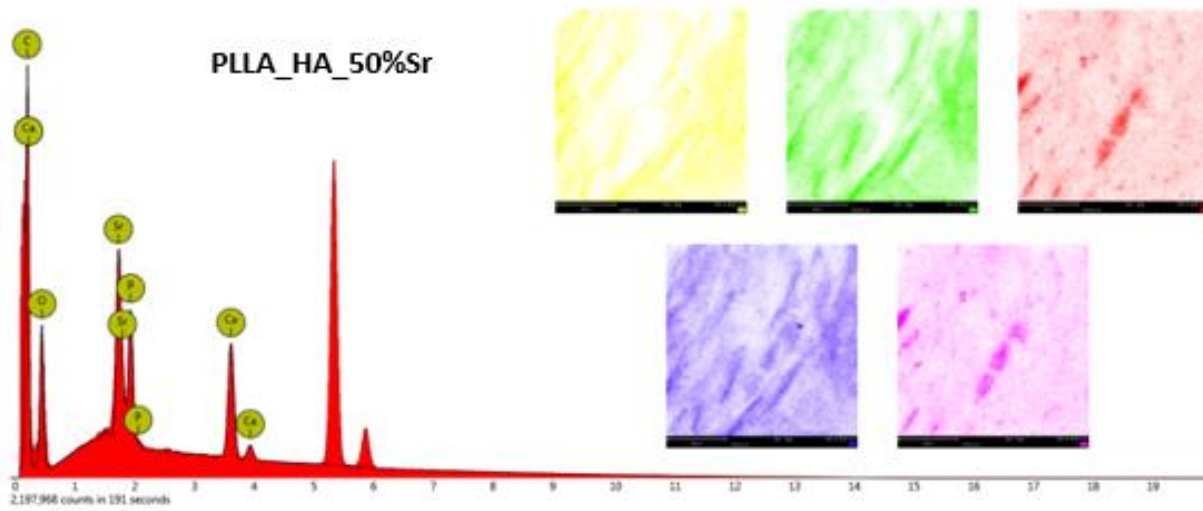
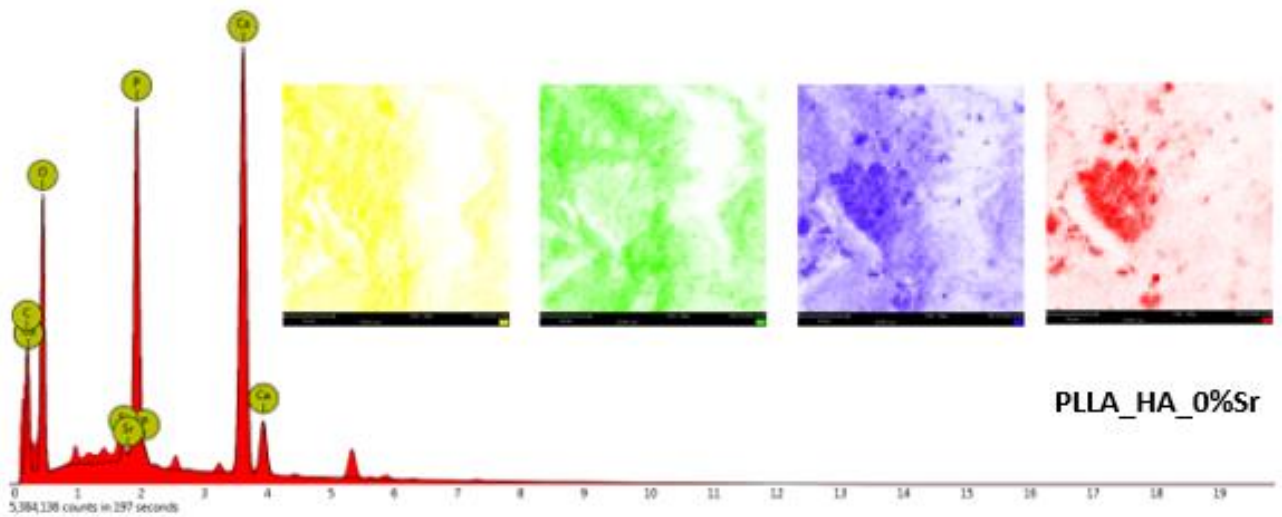


Figure 57: Up: EDS spectrum of PLLA\_HA\_0%Sr sample. Insert: detail of the scanned zone. Elemental distribution. Middle: EDS spectrum of PLLA\_HA\_50%Sr sample. Insert: detail of the scanned zone. Elemental distribution. Down: EDS spectrum of PLLA\_HA\_100%Sr sample. Insert: detail of the scanned zone. Elemental distribution. Yellow represents oxygen, green is carbon, red is phosphorous, blue if presented is calcium and pink if presented is strontium.

Table 31 presents the atomic and weight concentrations for the PLLA\_HA\_0%Sr, PLLA\_HA\_50%Sr and PLLA\_HA\_100%Sr samples. As expected, the composition of the filament is coherent to the characteristic elements of the type of HA utilized. PLLA\_HA\_0%Sr does not comprehend strontium, PLLA\_HA\_50%Sr comprehends both strontium and calcium, while PLLA\_HA\_100%Sr lacks calcium. Calcium content decreases from HA\_0%Sr to HA\_50%Sr, and the atomic and weight concentrations are exhibiting a lower content for the HA\_50%Sr. On the contrary, strontium increases from HA\_50%Sr and HA\_100%Sr and this behaviour is reflected in the filament composition.

*Table 31: Atomic and weight concentration of PLLA\_HA\_0%Sr, PLLA\_HA\_50%Sr and PLLA\_HA\_100%Sr samples.*

Element	PLLA_HA_0%Sr		PLLA_HA_50%Sr		PLLA_HA_100%Sr	
	Atomic %	Wt%	Atomic %	Wt%	Atomic %	Wt%
O	71.29	61.06	54.16	41.13	58.21	31.59
C	14.48	9.31	26.74	15.24	11.57	4.71
Ca	8.71	18.69	7.47	10.99	--	--
P	4.92	8.15	6.96	13.24	13.60	14.29
Sr	--	--	4.67	19.41	16.62	49.40

Finally, to summarize the obtained results from the morphological and compositional assessment, it can be said that:

- inorganic phase is incorporated within the PLLA matrix, independently from the different nature, quantity and processing step of the filaments;
- agglomerates are present in all the composites;
- bigger agglomerates are present in the samples extruded once;
- a more homogeneous dispersion can be seen in the filaments extruded two times.

### 4.3.3 Mechanical properties of the extruded filaments

Stress–strain measurements are performed to reveal the effects of the inorganic phases on the mechanical properties of PLLA filaments (Fig. 58). It can be observed that the inorganic phases are not greatly changing the shape of the stress-strain curves.

Pure PLLA shows a brittle behaviour, as after the ultimate tensile strength is reached, the material fractures. The inorganic phase causes an increased brittleness, which is an expected behaviour. In fact, other studies demonstrates that an increase in glass powder content enhances the brittleness and decreases resistance to crack propagation.<sup>131</sup>

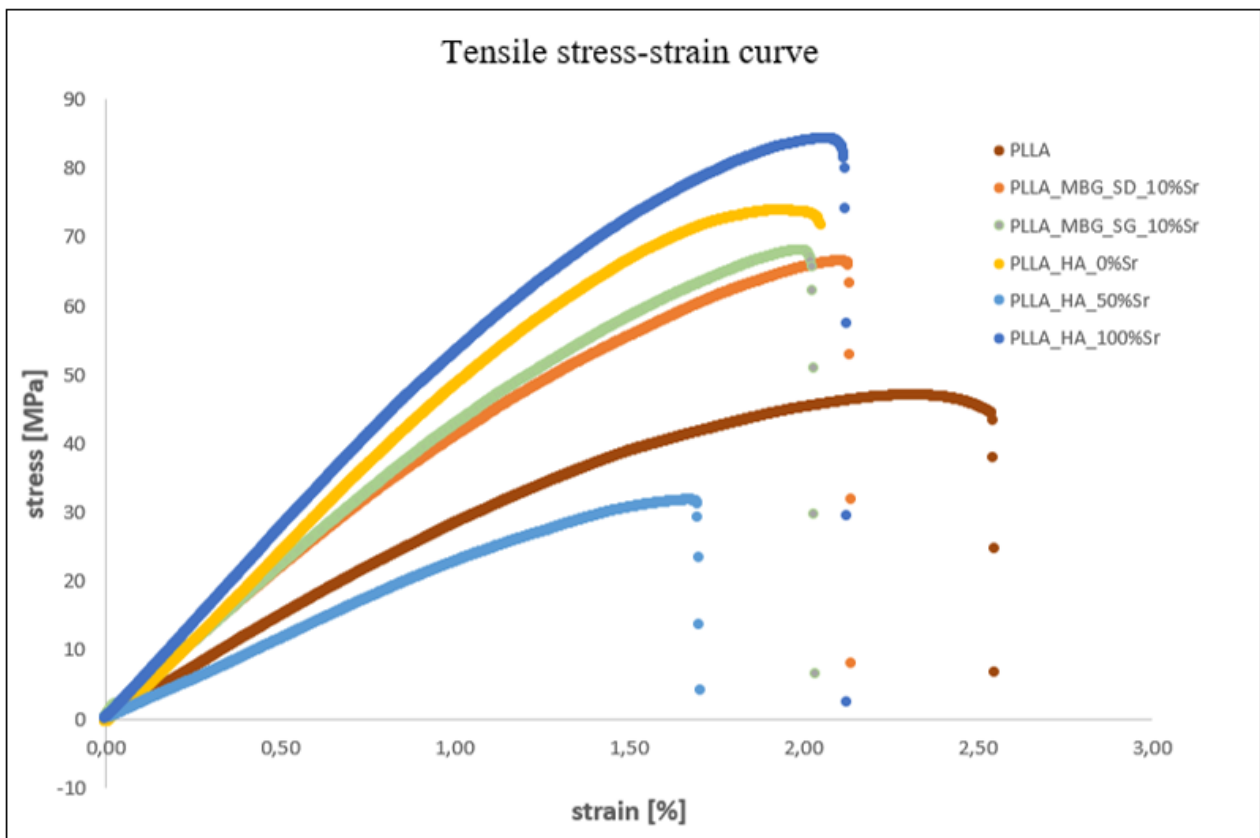


Figure 58: Stress-strain curves for the extruded filaments.

Table 32 presents the tensile strength and Young's modulus for the performed experiments, pure PLLA and composites filaments, compared to human bone. Compared to pure PLLA, the composite filaments exhibit higher tensile strength. This behaviour can be linked to the strong interactions between the polymeric matrix and the incorporated inorganic phase, then causing the increased strength of the composites. It can be seen that the only exception is PLLA\_HA\_50%Sr, which is instead showing an opposite behaviour. This can be

explained because it was the first composite which underwent the second extrusion process. The temperature adjustment in this case was not optimal, leading to partial material degradation.

As for the other composites, it appears that the behaviours are similar, despite the powder content and the number of extrusions subjected. PLLA\_HA\_0%Sr, PLLA\_HA\_100%Sr and pure PLLA are extruded once, and the average values for tensile strength are, respectively,  $65.2 \pm 8.2$  MPa,  $80.8 \pm 3.6$  MPa and  $49.6 \pm 5.5$  MPa. This confirms that the inorganic phase is able to improve the polymer's mechanical strength. In the case of the composites extruded twice, it can also be seen an improvement in the polymer's tensile strength. In fact, despite the second extrusion, the average tensile strength is  $64.1 \pm 10.3$  MPa and  $52.3 \pm 4.2$  MPa, for the samples PLLA\_MBG\_SD\_10%Sr and PLLA\_MBG\_SG\_10%Sr, respectively. The PLLA\_MBGs samples are expected to have a decreased molecular weight because of the second thermal treatment. Nevertheless, it is already stated in literature that properties as tensile strength and Young's modulus are not significantly dependent over the molecular weight of the polymer.<sup>132</sup> Because of this, as the molecular weight is not affecting the composite performance, it means that the prevalent behaviour is the strengthening effect of the inorganic phase inclusion.

Moreover, it can be confronted the powder content over the general trend of the tensile curve. As the curves depict, and the tensile strength value suggests, there is no great dependence on the powder content over the composites' performance. The strongest composites appear to be PLLA\_HA\_100%Sr and PLLA\_HA\_0%Sr, followed by both PLLA\_MBGs samples. This can be linked to the fact that, to a certain extent, a higher amount of powder is able to impair the strength of the composite. As stated in literature, inorganic phase is able to improve the mechanical properties of the matrix. At the same time, other works detailed that the inorganic phase is not able to strongly adhere to the polymer, therefore causing an early failure at the polymer-powder interface.<sup>133</sup> Despite those studies, the results of the present work seem to be in accordance to the theory affirming that its addition promotes the composites' strength.

The increased strength can be linked to the increased Young's modulus. Other studies also showed an increased modulus of elasticity of the composite, effectively improved with higher filler content.<sup>134</sup> As can be seen from figure 59, all the curves, except for PLLA\_HA\_50%Sr, present a higher slope, if compared to the pure PLLA filament. The slope of stress-strain curve displays the Young's modulus, and a higher value is associated with an increased resistance to subject deformations. The higher value is recorded for the PLLA\_HA\_100%Sr, once more, confirming the effect of strengthening of the inorganic phase.<sup>135</sup>

Table 32: Tensile strength and Young's modulus of the filaments in comparison to bone tissue values.

Sample	Tensile strength (MPa)	Modulus (GPa)
PLLA	49.6 ± 5.5	3.055 ± 0.036
PLLA_MBG_SD_10%Sr	64.1 ± 10.3	4.064 ± 0.228
PLLA_MBG_SG_10%Sr	52.3 ± 4.2	4.215 ± 0.023
PLLA_HA_0%Sr	65.2 ± 8.2	4.591 ± 0.381
PLLA_HA_50%Sr	35.6 ± 2.7	2.472 ± 0.103
PLLA_HA_100%Sr	80.8 ± 3.6	5.448 ± 0.171
Cortical bone	100 ± 50	15 ± 5
Trabecular bone	3 ± 2	2.5 ± 2

Table 33 presents the strain for the performed experiments, pure PLLA and composites filaments. It can be observed that PLLA filament exhibits the higher value of strain among all the filaments. This can be linked to a higher elongation prior the break. The behaviour of the composites can be explained considering that the inorganic phase reduces the possibility for the polymeric chains to re-organize and, consequently, reducing the amount of tolerable deformation prior the rupture.

As before, the PLLA\_HA\_50%Sr is presenting a lower performance than the other composites because of the partial degradation due to the excessive temperatures utilized. As for the other composites, they all display a similar average strain value, comprised between 2.04 and 2.19%. This means that the number of extrusion processes the composite underwent (two for PLLA\_MBG\_SD/SG\_10%Sr and one for PLLA\_HA\_0%Sr and PLLA\_HA\_100%Sr samples) or the powder content (2% in case of MBGs and 5% in case of HA composites) are not significantly affecting the composites' performance.

Table 33: Strain of the extruded filaments. The results are presented as average ± standard deviation.

Sample	Strain (%)
PLLA	2.73 ± 0.22
PLLA_MBG_SD_10%Sr	2.14 ± 0.03
PLLA_MBG_SG_10%Sr	2.04 ± 0.27
PLLA_HA_0%Sr	2.09 ± 0.49
PLLA_HA_50%Sr	1.73 ± 0.27
PLLA_HA_100%Sr	2.19 ± 0.21

From the overall results of the mechanical properties of the extruded filaments, it can be stated that:

- the inorganic phase is able to improve the strength of the polymer and increasing the brittle behaviour of the composite;
- the composites are presenting higher Young's modulus;
- the inorganic phase reduces the possibility for the polymeric chains to re-organize, indicating that are less inclined to strain as a stress is applied;
- filaments stress-strain curves are similar for all the performed experiments, indicating that either the number of processing steps or the amount of powder content do not influence the behaviour of the composites;
- the presented performances are indicating that the provided and produced dispersions are able to produce filaments with the similar mechanical properties under tension, better than those of pure PLLA.

The developed device has not a structural purpose, but it needs to have certain strength to be fixed to bone by metallic screws. After the printing process other tests are needed to ensure the desired mechanical properties are obtained; otherwise, changes will be applied accordingly.

#### 4.3.4 Rheological properties of the extruded filaments

Rheological assessment is fundamental for understanding the response of the material when subjected to a specific test. A sinusoidal stress was applied in a range of frequency varying from 1 to 600 rad/s, with a constant strain of 1%, to test the variance in visco-elastic properties of the material as the frequency changes. The results of the frequency sweep tests will give information about the samples' physical strength and cohesiveness, specifying which is the physical state of the material at a given value of frequency. From the data of the frequency sweep tests, applying Cox-Merz equation, it is possible to obtain flow ramps, which can specify the relationship between the material's viscosity and shear rates. The main objective of the rheological assessment was to evaluate and compare the composites' behaviour, discriminating the effect of the inorganic phase within the polymeric matrix.

In this work, it is reasonable to expect a different behaviour from pure PLLA and composites samples, being them more rigid because of the inorganic phase added to the polymeric matrix. Then, as for the viscosity, it is expected a decreased value for the samples which underwent more processing steps.

#### 4.3.4.1 Frequency sweep tests

Figures 59 and 60 present the results of the frequency sweep tests performed on the different material samples: pure PLLA and composites, PLLA\_MBG\_SD\_10%Sr, PLLA\_MBG\_SG\_10%Sr, PLLA\_HA\_0%Sr, PLLA\_HA\_50%Sr and PLLA\_HA\_100%Sr. When the material is subjected to a shear strain, the resulting stress can be written in terms of storage and loss modulus. The first,  $G'$ , represents the elastic contribution, whilst the latter,  $G''$ , represents the viscous contribution.  $G'$  is the component of stress in phase with the strain and its value represents purely elastic materials, where the maximum stress occurs at maximum strain.  $G''$  is the component of the stress  $90^\circ$  out of phase with the strain and describes purely viscous materials, where the maximum stress occurs at minimum strain rate. In a visco-elastic material, the behaviour can be either solid-like or liquid-like, based on the prevalent component, elastic or viscous, respectively.<sup>122</sup>

The results of a frequency sweep test display the variation of the previously introduced moduli ( $G'$  and  $G''$ ) according to an applied stress, when stress frequency increases within a defined range. When the storage modulus is predominant compared to loss modulus, the material presents a solid-like behaviour, and thus a higher ability to store energy. On the contrary, when loss modulus is higher than storage modulus, the material is defined as liquid-like, with higher tendency to dissipate energy through heat and permanent deformations.

In this study, the material samples were subjected to a constant strain of 1% varying the frequency between 1 and 600 rad/s, while the test temperature was set at 220 °C, constant during all the measures. The test was performed at 220 °C because it is the chosen temperature for the subsequent extrusion process for the device production. As this test can give information about the material's physical state at a defined frequency, it is important to characterize its behaviour at the chosen processing temperature, to obtain valuable and useful results for the next steps.

In the graphs reported in figures 59 and 60, loss modulus and storage modulus are plotted in green and blue respectively.

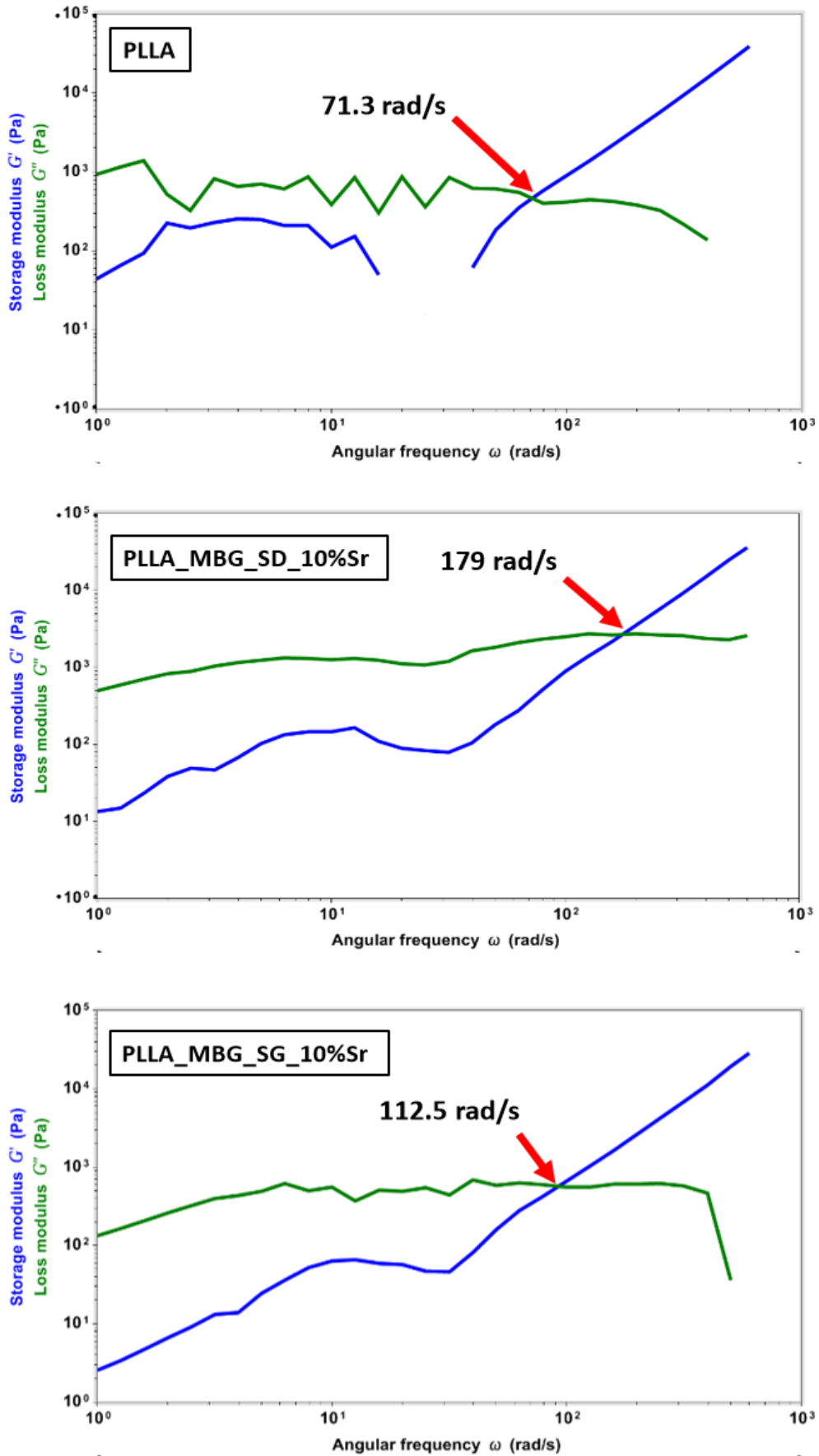


Figure 59: Frequency sweep tests of PLLA, PLLA\_MBG\_SD\_10%Sr and PLLA\_MBG\_SG\_10%Sr samples.

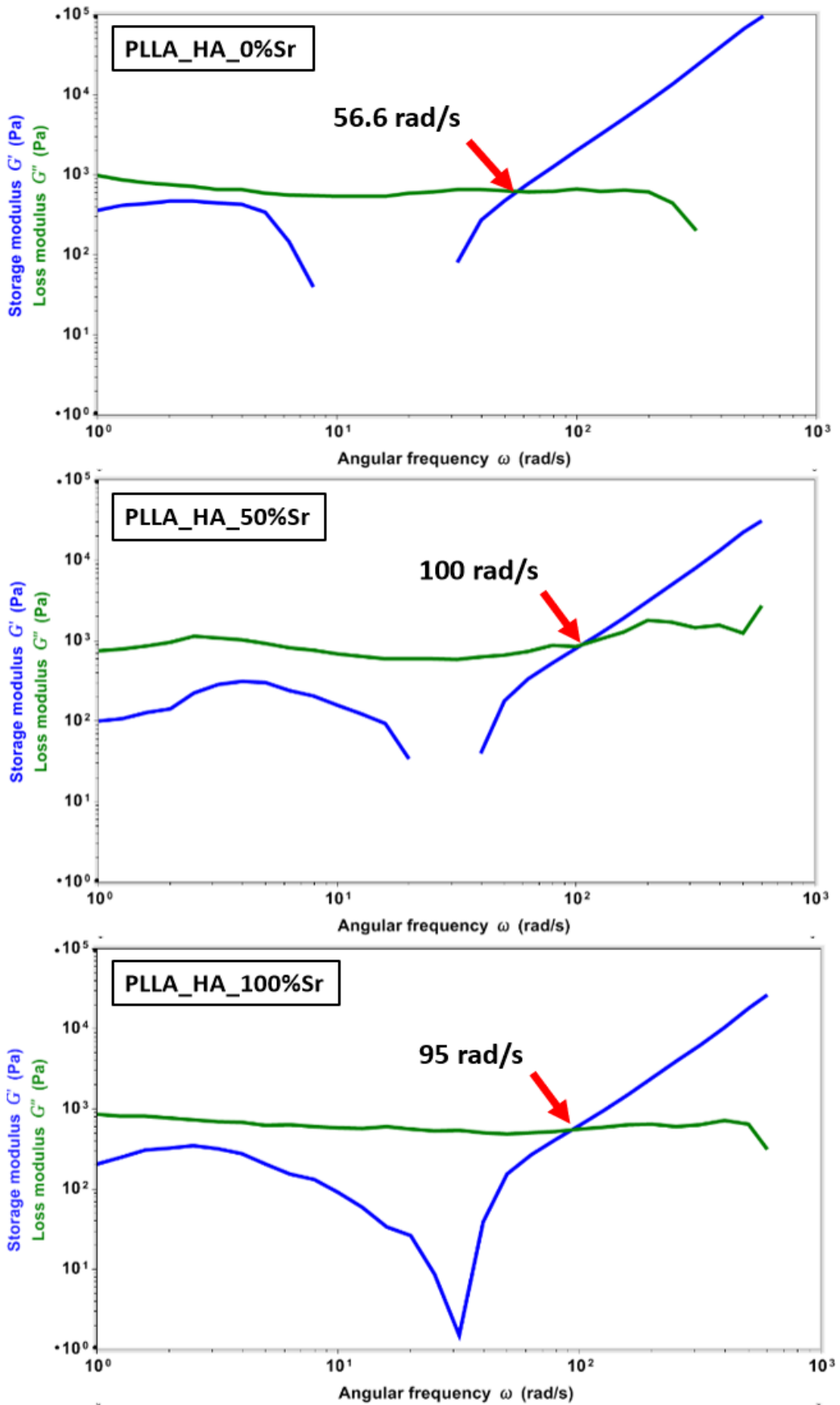


Figure 60: Frequency sweep tests of PLLA\_HA\_0%Sr, PLLA\_HA\_50%Sr and PLLA\_HA\_100%Sr samples.

Figure 59A represents the variation of  $G'$  and  $G''$  of PLLA filaments with increasing frequencies. It can be seen that loss modulus is higher than storage modulus for low frequencies. This implies that the sample is in a liquid-like state and thus the viscous behaviour prevails over the elastic one. The lack in some points related to the curve of storage modulus could be due to either the non-homogeneity of the sample or the presence of an air bubble. As a consequence, the machine is unable to correctly measure those points and the values are under its range of sensibility. The analysis shows that it is possible to identify a characteristic frequency beyond which the sample shifts to a solid-like behaviour and the elastic component prevails over the viscous one. In the case of PLLA filaments we can detect the change in the visco-elastic behaviour at a frequency of about 71.3 rad/s. All crossover frequencies are summarized in Table 34.

Figure 59B and 59C present the behaviour of PLLA\_MBG\_SD\_10%Sr and PLLA\_MBG\_SG\_10%Sr samples, respectively. Both the samples are behaving in a liquid-like state at low frequencies, as loss modulus is higher than storage modulus. As the frequency increases the elastic modulus increases its importance, until the crossover point is reached. Then, the samples behave like a solid. The crossover point is found at higher frequencies compared to pure PLLA, at 179 rad/s and 112.5 rad/s respectively. Loss modulus ( $G''$ ) in both cases is presenting an almost constant trend, while storage modulus ( $G'$ ) is presenting in both cases an increasing trend. At low frequencies loss modulus is significantly higher than storage modulus, indicating that the viscous component is greatly prevailing over the elastic component.

Figure 60A, 60B and 60C display the behaviour of PLLA\_HA\_0%Sr, PLLA\_HA\_50%Sr and PLLA\_HA\_100%Sr samples, respectively. At low frequencies the samples are in a liquid-like form, with loss modulus higher than storage modulus. The values of the two components are similar, sign that the viscous component is not as prevalent over the elastic component, similarly to what observed for MBG-based composites. The crossover frequencies are reached at 56.6 rad/s, 100 rad/s and 95 rad/s, respectively. Above those frequency values, storage modulus is prevailing over loss modulus and consequently, the behaviour of the samples is solid-like. At frequencies between 10 and 30 rad/s, storage modulus is not represented or is characterized by some points deeply underrated, and this is due to non-homogeneity in the sample's structure. All three HA-based composites show a constant trend for loss modulus ( $G''$ ), while storage modulus ( $G'$ ) presents a sharp increase after the frequency reaches 60 – 70 rad/s.

Table 34: Crossover frequencies of the performed samples.

Sample	Crossover frequency (rad/s)
PLLA	71.3
PLLA_MBG_SD_10%Sr	179
PLLA_MBG_SG_10%Sr	112.5
PLLA_HA_0%Sr	56.6
PLLA_HA_50%Sr	100
PLLA_HA_100%Sr	95

From the analysed graphs, it can be seen that at low frequencies both PLLA and the different composites behave as liquid-like systems. In fact, the viscous component prevails over the elastic one, meaning that the polymeric chains are able to re-organize and adapt themselves to the applied stresses. On the contrary, when the frequency of the applied stress increases, the polymeric chains are not able to re-organize. The consequence is the change in the overall material's behaviour, as the elastic component, in correspondence of a specific frequency, becomes higher than the viscous one, leading to a solid-like response. The material is still a fuse, but as the chains are blocked, it behaves like an elastic solid material. The abovementioned behaviours are similar for all the performed samples, meaning that the inorganic phase is not greatly affecting the general performance of the polymer. The frequency sweep test is also able to indirectly provide information about the molecular weight of the polymer. In fact, as the molecular weight increases, the polymeric chains are longer with more potential entanglements. Chains' length can directly affect the overall performance of the material because, if longer and characterized by increasing entanglements, their flow is hindered even at lower frequencies. On the contrary, shorter and less entangled chains are more able to re-organize and adapt to the applied stresses, and the material can thus keep a liquid-like behaviour at higher stress frequencies.

Table 35 summarizes the values of loss and storage modulus of all samples at the lowest frequency, 1 rad/s. Loss modulus for pure PLLA sample is displaying a constant trend but is characterized by an indented curve. Therefore, the value of the loss modulus at low frequencies cannot be precisely defined. From the trend of the curve, the average value of storage modulus at low frequencies for pure PLLA can be settled more correctly at  $10^2$  Pa s.

Table 35: Storage and loss modulus of the performed samples at 1 rad/s.

Sample	Storage modulus at 1 rad/s	Loss modulus at 1 rad/s
PLLA	44.04	920.97
PLLA_MBG_SD_10%Sr	13.39	497.67
PLLA_MBG_SG_10%Sr	2.53	132.26
PLLA_HA_0%Sr	363.28	982.39
PLLA_HA_50%Sr	100.07	757.46
PLLA_HA_100%Sr	206.38	866.07

To briefly summarize the samples production processes, PLLA, PLLA\_HA\_0%Sr and PLLA\_HA\_100%Sr were produced with one processing step (were extruded one time), while PLLA\_MBG\_SD\_10%Sr, PLLA\_MBG\_SG\_10%Sr and PLLA\_HA\_50%Sr were extruded two times because of the inconsistency of the filament obtained after the first extrusion process.

Comparing PLLA, PLLA\_HA\_0%Sr and PLLA\_HA\_100%Sr, a similar change in the visco-elastic properties according to the increase of frequency can be observed. This is a sign that, for samples which underwent the same working steps, the inorganic phase is not directly affecting the general properties of the polymer. Then, the main influence remains related to the molecular weight. As evidenced by the plotted values in Table 35, storage and loss modulus of the PLLA\_HA\_0%Sr and PLLA\_HA\_100%Sr composites are higher than pure PLLA. Comparing those behaviours, it can be said that the inorganic phase is able to increase the overall rheological properties of the material, as reported by several authors in the literature. Barnes et al.<sup>136</sup>, defined that the overall complex modulus of the material is always increased with the addition of ‘fillers’ to the polymeric matrix.

PLLA\_MBG\_SD\_10%Sr, PLLA\_MBG\_SG\_10%Sr and PLLA\_HA\_50%Sr were extruded two times and it can be observed that those cases have higher crossover frequency, if compared to the previously analysed samples. This behaviour can be clarified by the decrease in molecular weight due to the second melting process. Indeed, extrusion causes polymer melting, reducing the length of the polymeric chains and consequently leading to a decreased molecular weight. Consequently, as already commented, shorter chains can adapt more easily to the applied stresses, even at higher oscillation frequencies, showing a more prolonged liquid-like behaviour. In addition, as described by Barnes et al., the effect of powder incorporation becomes more relevant as more filler is added.<sup>136</sup> The reinforcement effect of filler can be analysed for the samples extruded twice, PLLA\_HA\_50%Sr, PLLA\_MBG\_SD\_10%Sr and PLLA\_MBG\_SG\_10%Sr, as the composite made by HA has a 5% of powder content, while the composites developed with MBGs have a 2% of powder content. Comparing the samples’ storage and loss modulus it can be seen that the values are higher in HA composite. It is then confirmed that the increase in powder content improves the reinforcement effect. Moreover, directly comparing MBGs-containing samples (both extruded twice and with the same powder content), it can be seen that the PLLA\_MBG\_SD\_10%Sr has greater values of storage and loss modulus. It is already discussed that

MBG\_SD\_10%Sr particles (0.5-5  $\mu\text{m}$  in diameter) are bigger than MBG\_SG\_10%Sr (200-300 nm). Then, the difference can be directly linked to the existing interactions between the polymeric matrix and the added inorganic phase. The higher values in storage and loss moduli are then linked to the greater particles' dimensions, as would further impact over the polymeric chains' mobility.

It can be concluded that the difference in the overall values of storage and loss moduli are an indication of the structure of the polymer. If the difference between storage and loss modulus is higher, the viscous component is greatly prevalent over the elastic one; this indicates that the system is less structured and less able to store energy. In the frame of this work, the higher differences and lower values of storage moduli can be found in the composites extruded twice (PLLA\_HA\_50%Sr, PLLA\_MBG\_SD\_10%Sr and PLLA\_MBG\_SG\_10%Sr). These results thus indicate that the molecular weight has been affected by the manufacturing process, presenting more fluid melted samples. Those results can be also confirmed by the trend of viscosity at different shear rates, as discussed in the next section.

#### *4.3.4.2 Flow ramps*

One of the most important aspects to investigate in this study concern the material printability, as further studies will decide which is the best printing condition for the tested composites. In this frame, a flow ramp can give evidences about the viscosity of the material at a given shear rate. However, due to the nature of the investigated material, it was not possible to directly perform a flow test on material samples. This is directly related to complex nature of thermoplastic polymers, which present high values of viscosity once melted. In fact, since flow tests are based on a 360° rotation of the geometry, the high shear rates applied could greatly damage the sample structure, finally measuring non valuable results. In the case of thermoplastic-based materials, mathematical equations can help to obtain correct information about the visco-elastic properties of the fused samples.

The flow ramps presented in figures 61 and 62 are the results of the application of the Cox-Merz equation applied to the data obtained from the frequency sweep tests. Cox-Merz equation is an empirical mathematical rule able to convert the relationship between  $G'$  and  $G''$  and the oscillation frequencies in the one occurring between the material viscosity with the different values of shear rate.

The graphs display a decreasing trend of the viscosity as the shear rate increases for all the tested materials. The shear thinning behaviour is favourable for the desired application and could guarantee material's printability. In fact, printing machines usually have dies with limited dimensions. This is associated with an increased shear rate applied, and therefore a shear thinning character is preferable in order to obtain lower values of viscosity. Future investigations will be required in order to define the optimal range of viscosity that can guarantee the best printing results. In the present work the rheological studies aimed at analysing and

comparing the visco-elastic properties of the different materials at 220 °C (the chosen temperature for the extrusion process during the scaffold production step), especially discriminating the effect of the inorganic phase within the polymeric matrix.

The graphs are presented with a range of shear rates between 1 and 100 s<sup>-1</sup>, as the shear rates generally employed in an extrusion process based on AM technologies resides within this range. Figure 61A presents the PLLA viscosity with increasing shear rates, characterized by a non-regular decreasing trend. The highest viscosity value can be found at the lowest shear rate, while the lowest value of viscosity is found at the highest shear rate. All the values of viscosity registered at 1 and 100 s<sup>-1</sup> are summarized in Table 36.

Figure 61B and 61C present the viscosity trend for PLLA\_MBG\_SD\_10%Sr and PLLA\_MBG\_SG\_10%Sr samples, respectively. The trend is decreasing, as observed for pure PLLA sample, but with a more limited reduction.

Figure 62A, 62B and 62C present the viscosity trend for PLLA\_HA\_0%Sr, PLLA\_HA\_50%Sr and PLLA\_HA\_100%Sr samples, respectively. All three cases present a decreasing trend for the viscosity, with a plateau for PLLA\_HA\_50%Sr and PLLA\_HA\_100%Sr composites. PLLA\_HA\_0%Sr sample, instead, is presenting a slightly increasing trend at higher shear rates. This trend can be linked to the increasing strength of the material because the polymeric chains are not able to re-organize when the stress is applied too rapidly, phenomenon already analysed in the previous section.

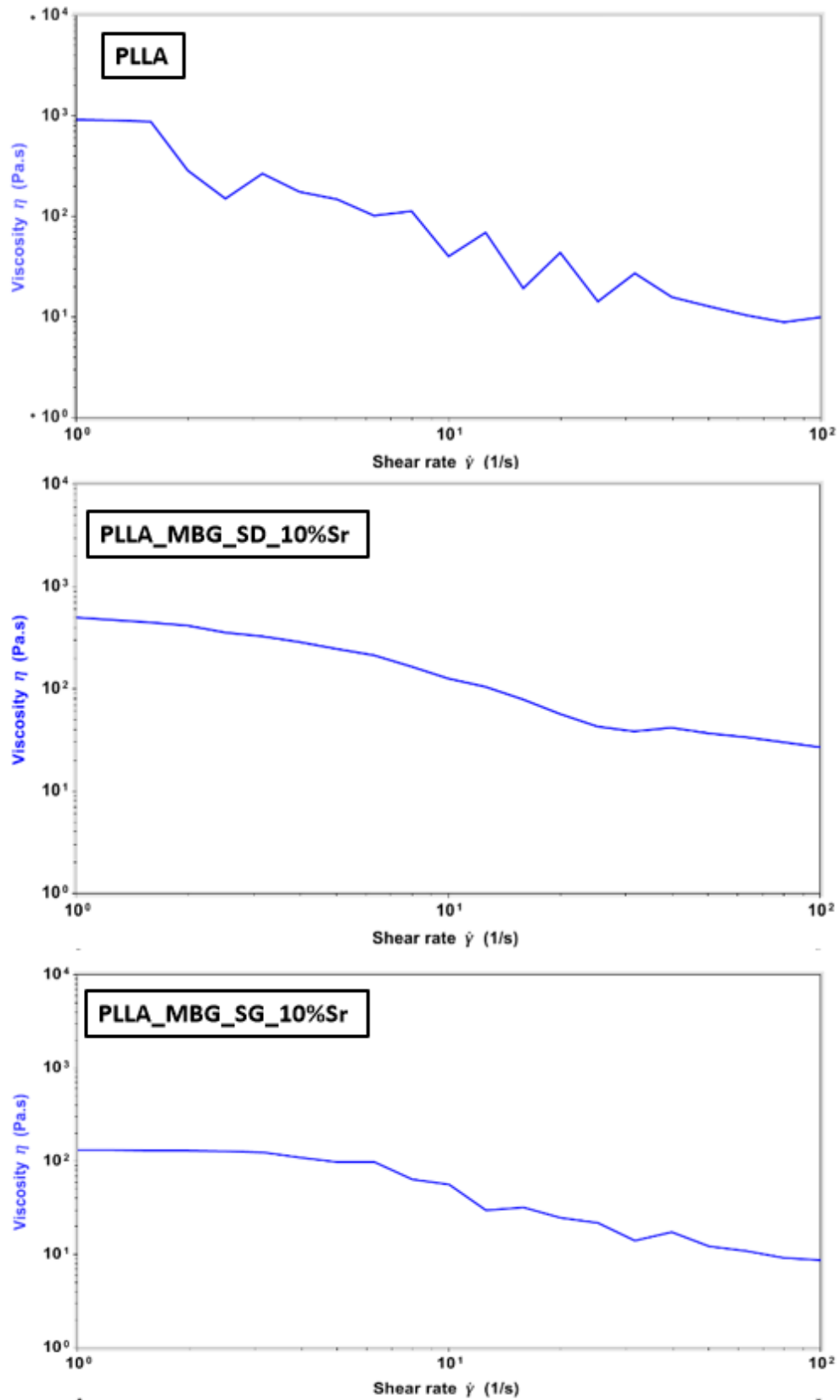


Figure 61: Flow ramps of PLLA, PLLA\_MBG\_SD\_10%Sr and PLLA\_MBG\_SG\_10%Sr samples.

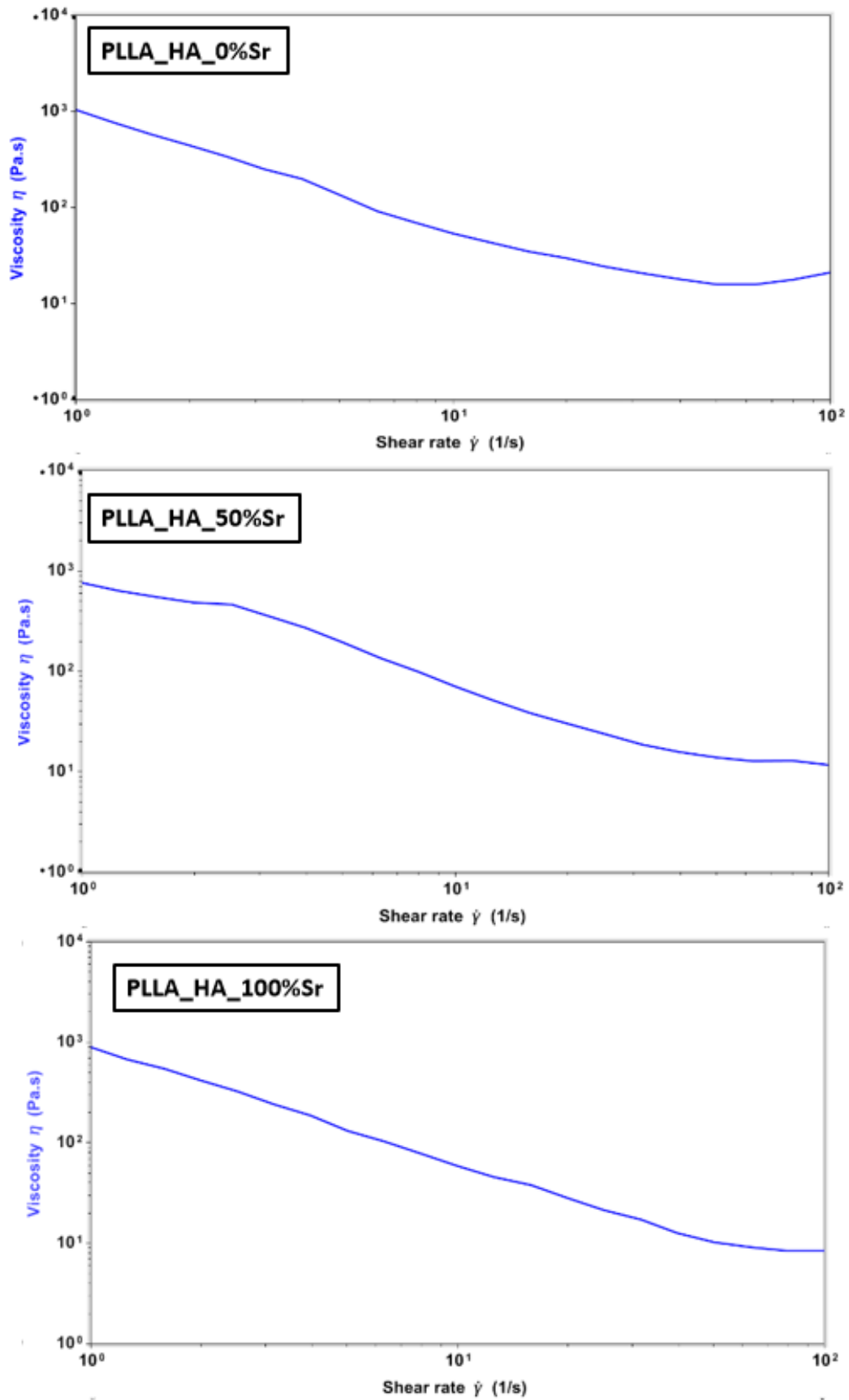


Figure 62: Flow ramps of PLLA\_HA\_0%Sr, PLLA\_HA\_50%Sr and PLLA\_HA\_100%Sr samples.

Table 36: Viscosity parameters of the performed samples at 1 and 100 s<sup>-1</sup>.

Sample	Viscosity at 1 s <sup>-1</sup>	Viscosity at 100 s <sup>-1</sup>
PLLA	922.02	9.90
PLLA_MBG_SD_10%Sr	497.85	27.75
PLLA_MBG_SG_10%Sr	132.29	8.68
PLLA_HA_0%Sr	1047.40	21.24
PLLA_HA_50%Sr	764.04	11.73
PLLA_HA_100%Sr	890.32	8.39

The data presented in Table 36, generally indicate that the values of viscosity at 1 s<sup>-1</sup> are generally higher, according to the structural and chemical composition of the polymer. Compared to PLLA, the PLLA\_HA\_0%Sr and PLLA\_HA\_100%Sr composites (all of them extruded once) display similar or higher viscosities, demonstrating once more that the inorganic phase is able to strength the material. For the materials extruded two times at high temperatures, PLLA\_MBG\_SD\_10%Sr, PLLA\_MBG\_SG\_10%Sr and PLLA\_HA\_50%Sr, the values of viscosity at 1 s<sup>-1</sup> are lower than the previous samples. This can be linked to the second extrusion process, that potentially break the polymeric chains, hence favouring their movements. Among those three samples, the higher value of viscosity at lower shear rates belongs to PLLA\_HA\_50%Sr, where the powder content is higher. Similar to the previous discussion, the higher powder content (5% for HA samples and 2% for MBGs composites) led to an increase in material's strength, as the chains are more restricted in their movements. This is directly connected to the increase in viscosity, as it quantitatively measures the internal fluid friction. Higher viscosity is associated to higher friction and less tendency to movement.

At higher shear rates, all the performed samples display viscosities varying in a limited range (from 8.39 Pa s to 27.75 Pa s). This similarity can be linked to the fact that, at higher shear rates, the powder effect is less significant, if compared to lower shear rates. This phenomenon is described by Kashi et al.<sup>106</sup>, who observed that at higher shear rates, the rheological properties reflect the mechanical resistance of the polymers' chains, being them less affected by the presence of the nanoparticles. Instead, at low shear rates, the visco-elastic properties reveal information about the microstructure and the interactions within the system, comprehending the polymer-nanoparticle connection. That is the main reason behind the higher range in values at low shear rates while, at high shear rates, the behaviours are similar for all the developed composites.

To sum up the overall results of the rheological assessment, it can be concluded that:

- all the tested materials exhibit a similar behaviour, liquid-like at lower frequencies and solid-like at higher frequencies;
- the inorganic phase is able to strength the PLLA matrix, consequently increasing storage and loss moduli as well as viscosity values;
- starting from the same processing conditions, a higher powder content more significantly increases the visco-elastic properties of the polymer;
- the second extrusion process, used in preparation of PLLA\_HA\_50%Sr and MBG-containing composites, causes a decrease in the polymer molecular weight, therefore increasing chains' mobility resulting in the presence of a liquid-like behaviour at higher frequencies and lower values of viscosities at low shear rates;
- the powder content affects the viscosity especially at lower frequencies or shear rates.

## 5 – Conclusions and future perspectives

The work described in the previous chapters can be divided into 5 phases:

- 1- Synthesis and characterization of mesoporous bioactive nanoparticles produced through batch sol-gel synthesis in basic medium with SiO<sub>2</sub>-CaO base composition and modified with strontium ions at predefined concentration (10% molar), to impair bone forming abilities and reduce osteoclasts bone resorption;
- 2- Synthesis and characterization of mesoporous bioactive microparticles produced through spray-drying aerosol-assisted sol-gel procedure and combined with strontium ions at the same molar concentration as before (10% molar);
- 3- Characterization of nano-hydroxyapatites provided from Fluidinova, project partner in the GIOTTO consortium, and substituted with different concentrations of strontium ions (0 – 50 – 100%), to impair bioactivity and bone forming abilities;
- 4- Dissolution of inorganic phases within a matrix of PLLA from water suspensions and subsequent extrusion into a consistent filament with defined diameter;
- 5- Characterization of the produced filaments, with mechanical and rheological assessments.

The subsequent sections will briefly comprise the results obtained from the previous characterizations, including the conclusions that could be done and, finally, the future perspectives.

### 5.1 Conclusions

The present work is framed in the H2020 GIOTTO project where the general aim is to develop medical devices with the ability to affectively treat osteoporotic fractures. Specifically, the aim of the work is the synthesis and fabrication of hybrid formulations based on PLLA and osteoinductive inorganic phases (MBGs and HA), that will then be used to fabricate a customized and bioactive device.

The goal of the first part of the work was to produce and characterize bioactive inorganic phases that will be included into the PLLA matrix, to create and extrude hybrid formulations suitable for the subsequent printing step though Filament Fusion Fabrication processes. The chosen phases are nano-hydroxyapatite and mesoporous bioactive glasses, already known for their bioactivity and biocompatibility. MBGs were produced through two different synthesis methods, able to generate particles with different dimensions and structural properties. HA is provided by Fluidinova, Porto, Portugal. In order to impart a more pronounced osteoinductive effect, both the inorganic phases incorporated strontium ions, well known for the pro-osteogenic and anti-

clastogenic potential. In particular, strontium ion is incorporated with a 10% molar amount into MBGs while HA is substituted with strontium at increasing percentages (0 – 50 – 100%).

The mesoporous phases containing strontium ions produced through sol-gel and spray-drying synthesis are characterized morphologically via FESEM, structurally via N<sub>2</sub> adsorption-desorption isotherms, EDS for the compositional characterization and ICP-AES for the ions release kinetics.

Based on the techniques previously described, for spray-drying samples it is possible to summarize the following results:

- the particles, despite the presence of strontium show a spherical morphology, with low rate of agglomeration;
- the particles' dimensions are micrometrical, with diameters comprised between 0.5 - 5 μm;
- strontium ion is effectively incorporated within the particles, as seen on EDS;
- N<sub>2</sub> adsorption-desorption analysis demonstrates that the particles have a mesoporous structure, as the presented isotherm is a characteristic type IV isotherm, with a type H2 hysteresis loop. Pore diameter and volume are, respectively, 6.6 nm and 0.3 cm<sup>3</sup>/g, in the distinctive range of mesoporous materials;
- specific surface area is around 217 m<sup>2</sup>/g, lower than the typical sol-gel synthesis because of the presence of strontium ions but higher than non-mesoporous glasses.

For sol-gel samples, the main results are:

- the particles have dimensions comprised between 200 - 300 nm with spherical morphology;
- strontium ion is successfully incorporated within the particles, as confirmed by EDS analysis;
- N<sub>2</sub> adsorption-desorption analysis demonstrates the mesoporous structure of the particles;
- specific surface area and pore volume are, respectively, 189 m<sup>2</sup>/g and 0.13 cm<sup>3</sup>/g, while pore size resulted of about 3 nm. The values are lower than the characteristic sol-gel samples, and it is linked to the presence of strontium ions, as already proved in literature.

Both the matrices are subjected to ion release tests, to evaluate their ability to effectively release the incorporated ions. Both of them display a burst release, but spray-drying samples release more ions in the first 3 hours. Sol-gel samples exhibit a limited pore dimension; the reduced diameter allows the connection with aqueous environment but slowing ion exit, which is therefore more controlled.

From the abovementioned results, it can be said that both synthesis of MBGs are able to incorporate strontium ion, not affecting the overall structure of the particles. A decrease in properties as specific surface area, pore dimensions and pore volume are observed, because of the appearance of disorganized non-porous domains. A crucial feature is the ion release rate, as it must be as controlled as possible. MBGs display a burst release, more pronounced in case of MBG\_SD\_10%Sr, where up to the 90% of the incorporated strontium ions are released within 3 hours. MBG\_SG\_10%Sr displays a burst release (limited to the 60% of the incorporated strontium ions), but the release kinetic is more sustained.

The nano-hydroxyapatite characterization was performed, and the envisioned conclusions are:

- the particles dimensions are nano-metrical, as expected from the synthesis protocol. The particles appear rod-like in shape and the typical features of hydroxyapatite are still reproduced, even with strontium ion substitution. In fact, (Ca+Sr)/P ratio is close to the stoichiometric ratio of typical non-substituted hydroxyapatite;
- the HA\_50%Sr sample is characterized by a higher variability. In fact, both strontium and calcium ions are present within this formulation, then the system complexity increases and difficulties in establishing structural order arise;
- XRD pattern reveals that HA\_100%Sr shows higher crystalline structure;
- the ion release kinetic is similar for HA\_50%Sr and HA\_100%Sr samples, with limited release even after 21 days.

From the abovementioned results, it can be said that nano-HA is able to incorporate strontium ion, not affecting the overall structure and properties of the particles. Nano-HA increases its dimensions as strontium content increases, due to the ionic dimension of strontium ion, bigger than calcium. As concerning the ion release kinetics, HA\_50%Sr and HA\_100%Sr display a controlled release, being it an attractive feature for an implantable device where the osteogenic effect is desirable to last longer.

The second part of the work focused on the inorganic phase incorporation within the PLLA matrix. The incorporation phase is based on powder deposition on the polymeric pellets of an aqueous suspension containing the inorganic phase powders. As for pure nano-HA and totally substituted (HA\_0%Sr and HA\_100%Sr), the water suspension is provided by a project partner, then the incorporation is based on the mixing of PLLA with the suspension. As for nano-HA partially substituted (HA\_50%Sr) and both MBGs (MBG\_SD\_10%Sr and MBG\_SG\_10%Sr), the suspensions are produced by mixing water and powder under continuous mechanical agitation. All the suspensions, provided and produced, have a 15%wt concentration. The pellets are then mixed with the suspensions and the water is let dry, prior to the extrusion.

The tested powder concentrations within the PLLA matrix are:

- 5% for PLLA\_HA\_0%Sr, PLLA\_HA\_50%Sr and PLLA\_HA\_100%Sr;
- 2% for PLLA\_MBG\_SD\_10%Sr and PLLA\_MBG\_SG\_10%Sr.

General comments concerning the extrusion of the pure PLLA and hybrid formulations are:

- pure PLLA the filament is smooth, slightly opaque and without any visible defect.
- the PLLA\_HA\_0%Sr and PLLA\_HA\_100%Sr samples are not problematic during the extrusion, and consistent filaments with constant diameters are produced. The surface is quite smooth, and no visible defects are observed.
- the PLLA\_HA\_50%Sr, PLLA\_MBG\_SD\_10%Sr and PLLA\_MBG\_SG\_10%Sr samples needed a second extrusion as the first process is not permitting the production of consistent samples. The filaments are re-pelletized and extruded, but the temperatures used for the first sample (PLLA\_HA\_50%Sr) were too high. As a consequence, part of the resulting filament is degraded.

Pure PLLA displays an average diameter around 1.7 mm, similar to the desired value of 1.7 – 1.75 mm, typical of the machine, based on Fused Filament Fabrication technique, that will be then utilized for the scaffold production. The composites, instead, are presenting a white colour and a lower diameter. This aspect, common in all the developed composites can be explicated by the presence of the inorganic phase and the quick melting process. The quick processing leads to an incomplete polymeric fusion, while the presence of the inorganic phase leads to an increased friction within the machine's screws. As the powder is not strongly adhered to the polymers' pellets, some loss is unavoidable, then inevitable are also the increased friction and increased torque.

The produced filaments are then characterized morphologically with SEM and compositionally with EDS, to confirm powder incorporation. From the obtained results, it can be said that the powder incorporation is successful in all the tested composites. The dispersion seems more uniform in the case of PLLA\_MBG\_SD/SG\_10%Sr and PLLA\_HA\_50%Sr samples, because of the lower quantity and dimensions of the agglomerates, present in all the performed experiments. It is not possible, in the frame of this work, to confirm if the cause of the apparent more uniform distribution resides within the second extrusion process.

EDS analysis confirms the presence of the typical ions characterising the incorporated phases. Those elements (strontium, calcium, phosphorous and silicon) are uniformly present over the filament section, sign that the incorporation is successful despite the different nature, concentration and incorporation mechanism.

Mechanical properties, evaluated through tensile testing, are not negatively affected by the inorganic phases. In fact, the shape of the stress-strain curve is not dissimilar to the pure PLLA curve. The incorporated inorganic phase causes an increase in brittle behaviour of the filament and increases their strength. This behaviour is confirmed by the reported graphs and tables; the composites display an increased Young's modulus for all the tested samples (except for PLLA\_HA\_50%Sr sample, due to the polymer degradation). The brittleness is underlined by the limited strain, and the shape of the curve. In fact, as soon as the ultimate tensile strength is reached, the filament fails. Also, it can be concluded that the mechanical properties of the composites are improved because of the inorganic phase incorporation, but the increased properties are not affected by the different nature, concentration and suspension production mechanism.

Rheological assessment proved that the pure PLLA and composites exhibit a similar behaviour, liquid-like at low frequencies and solid-like at high frequencies. The composite is strengthened by the presence of the inorganic phase, as is able to increase the viscosity (indicating a higher internal friction and lower tendency to movement) as well as storage and loss moduli. At the same working conditions, an increased powder content causes a higher enhancement in visco-elastic properties while, if the composite undergoes through more thermal processes, the viscosity tends to decrease. This is linked to the lower molecular weight of the polymer, associated to shorter polymeric chains, then more able to move and adapt to the applied stresses.

The results of the second part of the work will give information about the material's printability; then supplementary studies will decide which are the most suitable conditions for the scaffold production. That aspect is not part of the thesis, but its main objective is related to the composite synthesis and extrusion, to investigate and confront the material's properties.

From the abovementioned results, it can be said that both incorporation mechanisms (Fluidinova commercial products or produced suspensions), both utilized inorganic phases (nano-HA and MBGs) and each phase concentration (5% for nano-HA and 2% for MBGs composites) are successful. The first mechanical assessment done in the frame of the work is useful in determining the properties of the filaments, but a second characterization needs to be performed after the printing process to ensure the desired mechanical properties. As for the rheological assessment it can be said that the composites that demonstrated a more reproducible behaviour are the composites made from MBGs. This could be due to either the limited amount of powder or the nature of the incorporated phase. Further studies are needed to explain the reasons behind the lack of point or the severely underrated ones in frequency sweep graphs for pure PLLA and PLLA\_HA\_0%Sr, PLLA\_HA\_50%Sr and PLLA\_HA\_100%Sr.

In conclusion, it can be said that the incorporation method based on produced suspensions is efficient and the best filament quality can be found in the PLLA\_MBGs filaments. The powder distribution seems homogeneous, and the present agglomerates appear to have limited dimensions. Mechanical properties are acceptable, as tensile strength is comparable to PLLA\_HA filaments, characterized by a greater amount of powder content. Moreover, the rheological assessment proved a shear thinning and a continuous behaviour over all the analysed frequencies.

## 5.2 Future perspectives

From the obtained results, it is necessary to optimize the powder incorporation, to improve stronger bonds with polymer pellets and reduce powder loss as well as its adhesion over the internal surfaces of the extrusion machine. It is necessary to work on extrusion process to assess the optimal parameters for extruder and Haul-Off velocities to obtain a consistent filament with the desired diameter (1.7 – 1.75 mm), in range with the machine, based on Fused Filament Fabrication, that will then be utilized. Another aspect to consider is the control over the temperatures, to avoid polymer degradation, as seen for PLLA\_HA\_50%Sr sample, and the significant decrease in its mechanical properties.

More studies are needed to control the powder dispersion over the polymeric matrix, to avoid agglomerates and obtain a uniform distribution. In fact, as seen for rheological assessment, the measures present holes or underrated points as the material is not effectively homogeneous in the totality of its parts. Then, despite SEM micrographs and EDS mapping display a uniform distribution, the spreading is not optimal within the totality of the polymeric matrix.

Ion release tests are needed to evaluate the ion release kinetics of the inorganic phase once incorporated within the PLLA matrix. It is reasonable to expect a slower release kinetic, due to the presence of the polymeric matrix that embraces the inorganic phase and therefore delaying the ion exit.

Finally, as the present work is incorporated within H2020 GIOTTO project, the next step is the optimization of the extrusion printing process. From the data registered from the rheological analysis it will be decided the optimal range of shear rates for material's extrusion, to obtain a consistent filament able to sustain the growing structure. Studies are required on the final device to assess mechanical properties (load bearing is not required, but it is essential a certain strength of the device to the fixed with screws to the bone), strontium ion release kinetics (it is imperative to tune the ion release according to bone growth and device's degradation, to allow a prolonged osteoinductive effect), degradation and bioactivity tests (to control the device behaviour once implanted in the body).

## Bibliography

1. Hoppe, A., Güldal, N. S. & Boccaccini, A. R. A review of the biological response to ionic dissolution products from bioactive glasses and glass-ceramics. *Biomaterials* **32**, 2757–2774 (2011).
2. Florencio-Silva, R., Sasso, G. R. D. S., Sasso-Cerri, E., Simões, M. J. & Cerri, P. S. Biology of Bone Tissue: Structure, Function, and Factors That Influence Bone Cells. *Biomed Res. Int.* **2015**, (2015).
3. Zaccheo D., Trattato di Anatomia Umana, Edi Ermes, 4th edition, ISBN 88-7051-285-1
4. Alghazali, K. M. *et al.* Bone-tissue engineering: Complex tunable structural and biological responses to injury, drug delivery, and cell-based therapies. *Drug Metab. Rev.* **47**, 431–454 (2015).
5. Vernè E., Slides "Ortopedia" lecture from "Materiali per la Bioingegneria" course, Politecnico di Torino, a.y. 2018-2019.
6. Viguet-Carrin, S., Garnero, P. & Delmas, P. D. The role of collagen in bone strength. *Osteoporos. Int.* **17**, 319–336 (2006).
7. Marotti G, Muglia MA, Palumbo C (1994) Structure and function of lamellar bone. *Clin Rheumatol* 13 Suppl 1:63–68
8. Bhattacharjee, A. & Bansal, M. Collagen structure: The Madras triple helix and the current scenario. *IUBMB Life* **57**, 161–172 (2005).
9. Ramachandran, B. P. G. N. & Kartha, G., Structure of Collagen, September 24, NATURE 593. 593–595 (1955).
10. Gelse, K., Pöschl, E. & Aigner, T. Collagens - Structure, function, and biosynthesis. *Adv. Drug Deliv. Rev.* **55**, 1531–1546 (2003).
11. Gilbert SF, *Developmental Biology*, 6th edition, Sunderland (MA): Sinauer Associates; 2000.
12. Sims, N. A. & Gooi, J. H. Bone remodeling: Multiple cellular interactions required for coupling of bone formation and resorption. *Semin. Cell Dev. Biol.* **19**, 444–451 (2008).
13. Golden, B. D. The prevention and treatment of osteoporosis. *Arthritis Rheum.* **11**, 124–134 (1998).
14. Assessment of fracture risk and its application to screening for postmenopausal osteoporosis, WHO technical report series 843, Geneva 1994.
15. Hernlund, E. *et al.* Osteoporosis in the European Union: Medical management, epidemiology and economic burden: A report prepared in collaboration with the International Osteoporosis Foundation (IOF) and the European Federation of Pharmaceutical Industry Associations (EFPIA). *Arch. Osteoporos.* **8**, (2013).
16. Pisani, P. *et al.* Major osteoporotic fragility fractures: Risk factor updates and societal impact. *World J. Orthop.* **7**, 171–181 (2016).
17. Piscitelli, P. *et al.* Ten years of hip fractures in Italy: For the first time a decreasing trend in elderly women. *World J. Orthop.* **5**, 386–391 (2014).

18. Bleibler, F., Rapp, K., Jaensch, A., Becker, C. & König, H. H. Expected lifetime numbers and costs of fractures in postmenopausal women with and without osteoporosis in Germany: A discrete event simulation model. *BMC Health Serv. Res.* **14**, 1–18 (2014).
19. Cauley, J. A. Public health impact of osteoporosis. *Journals Gerontol. - Ser. A Biol. Sci. Med. Sci.* **68**, 1243–1251 (2013).
20. <https://www.mayoclinic.org/diseases-conditions/osteoporosis/diagnosis-treatment/drc-20351974>
21. Rahaman, M. N. *et al.* Bioactive glass in tissue engineering. *Acta Biomater.* **7**, 2355–2373 (2011).
22. Kokubo T., Takadama H., “How useful is SBF in predicting in vivo bone bioactivity?”, *Biomaterials*, 2006, 27, 2907-2915
23. Hench, L. L. Bioceramics, *Stress Int. J. Biol. Stress* **28**, 1705–1728 (1998).
24. Chen, X. & Hu, Q. *Bioactive Glasses. Frontiers in Nanobiomedical Research* vol. 3 (2017).
25. Wu, C. *et al.* Bioactive SrO-SiO<sub>2</sub> glass with well-ordered mesopores: Characterization, physiochemistry and biological properties. *Acta Biomater.* **7**, 1797–1806 (2011).
26. Albrektsson, T. & Johansson, C. Osteoinduction, osteoconduction and osseointegration. *Eur. Spine J.* **10**, S96–S101 (2001).
27. European patent US8158543B2, Matthew John Dejenka, Sinue Gomez, Apr 2012; <https://patents.google.com/patent/US8158543B2/en>
28. Kargozar, S., Baino, F., Hamzehlou, S., Hill, R. G. & Mozafari, M. Bioactive Glasses: Sprouting Angiogenesis in Tissue Engineering. *Trends Biotechnol.* **36**, 430–444 (2018).
29. Nandi S.K., Mahato A., Kundu B., Mukherjee P., Zorzi A., De Miranda J., “Doped Bioactive Glass Materials in Bone Regeneration”, Zorzi A.R., De Miranda J.B., “Advanced Techniques in Bone Regeneration”, London, In Tech, 2016
30. Brauer, D. S. & Möncke, D. Chapter 3: Introduction to the Structure of Silicate, Phosphate and Borate Glasses. *RSC Smart Mater.* **2017-Janua**, 61–88 (2017).
31. Wu, C. & Chang, J. Mesoporous bioactive glasses: Structure characteristics, drug/growth factor delivery and bone regeneration application. *Interface Focus* **2**, 292–306 (2012).
32. Erol, M. & Boccaccini, A. R. Nanoscaled bioactive glass particles and nanofibres. *Bioact. Glas.* 129–161 (2011) doi:10.1533/9780857093318.2.129.
33. Baino, F., Fiorilli, S. & Vitale-Brovarone, C. Composite biomaterials based on sol-gel mesoporous silicate glasses: A review. *Bioengineering* **4**, 1–18 (2017).
34. Vallet-Regí, M. & Salinas, A. J. Chapter 17: Mesoporous Bioactive Glasses in Tissue Engineering and Drug Delivery. *RSC Smart Mater.* **2017-Janua**, 393–419 (2017).
35. [https://www.vcbio.science.ru.nl/public/pdf/amfifielen\\_eng.pdf](https://www.vcbio.science.ru.nl/public/pdf/amfifielen_eng.pdf)

36. Zhao, D., Wan, Y. & Zhou, W. Ordered Mesoporous Materials. *Ordered Mesoporous Mater.* **27**, 131–149 (2013).
37. Hoffmann, F., Cornelius, M., Morell, J. & Fröba, M. Silica-based mesoporous organic-inorganic hybrid materials. *Angew. Chemie - Int. Ed.* **45**, 3216–3251 (2006).
38. Vallet-Regí, M. Ordered mesoporous materials in the context of drug delivery systems and bone tissue engineering. *Chem. - A Eur. J.* **12**, 5934–5943 (2006).
39. Yan, X. X. *et al.* Mesoporous bioactive glasses. I. Synthesis and structural characterization. *J. Non. Cryst. Solids* **351**, 3209–3217 (2005).
40. Miguez-Pacheco, V., Gorustovich, A. A., Boccaccini, A. R. & Roether, J. A. Chapter 15: Bioactive Glasses for Soft Tissue Engineering Applications. *RSC Smart Mater.* **2017-Janua**, 336–361 (2017).
41. Montalbano, G., Fiorilli, S., Caneschi, A. & Vitale-Brovarone, C. Type I collagen and strontium-containing mesoporous glass particles as hybrid material for 3D printing of bone-like materials. *Materials (Basel)*. **11**, (2018).
42. J.H. Shepherd, D.V. Shepherd, S.M. Best, Substituted hydroxyapatites for bone repair, *J. Mater. Sci. Mater. Med.* **23** (2012) 2335–2347, <https://doi.org/10.1007/s10856-012-4598-2>
43. Jiang, Y., Yuan, Z. & Huang, J. Substituted hydroxyapatite: a recent development. *Mater. Technol.* **00**, 1–12 (2019).
44. Yan, X., Yu, C., Zhou, X., Tang, J. & Zhao, D. Highly ordered mesoporous bioactive glasses with superior in vitro bone-forming bioactivities. *Angew. Chemie - Int. Ed.* **43**, 5980–5984 (2004).
45. Montazerian, M. & Zanolto, E. D. *Bioactive Glass-ceramics : Processing , Properties and Applications.* (2017).
46. Kalita, S. J., Bhardwaj, A. & Bhatt, H. A. Nanocrystalline calcium phosphate ceramics in biomedical engineering. *Mater. Sci. Eng. C* **27**, 441–449 (2007).
47. Yilmaz, B., Alshemary, A. Z. & Evis, Z. Co-doped hydroxyapatites as potential materials for biomedical applications. *Microchem. J.* **144**, 443–453 (2019).
48. A. Nawawi, N., S.F. Alqap, A. & Sopyan, I. Recent Progress on Hydroxyapatite-Based Dense Biomaterials for Load Bearing Bone Substitutes. *Recent Patents Mater. Sci.* **4**, 63–80 (2011).
49. Cox, S. C. Synthesis Method of Hydroxyapatite. *Ceram* (2015).
50. Sōmiya, S. & Roy, R. Hydrothermal synthesis of fine oxide powders. *Bull. Mater. Sci.* **23**, 453–460 (2000).
51. Choudhury, P., Assembly, A. & Ka, T. oo dh ea d Pu bl is Li d. (2012) doi:10.13140/2.1.1858.8809.
52. Vlasea M, Shanjani Y, Basalah A, Toyserkani E, Additive Manufacturing for Tissue Engineering of Bone and Cartilage, *IJAMS* Volume 13, Issue 1, 2011
53. Vinny R. Sastri, 9 - Other Polymers: Styrenics, Silicones, Thermoplastic Elastomers, Biopolymers, and Thermosets, doi.org/10.1016/B978-1-4557-3201-2.00009-4.
54. Grigore, M. E. Methods of recycling, properties and applications of recycled thermoplastic polymers. *Recycling*

- 2, 1–11 (2017).
55. Anderson, J. M. & Shive, M. S. Biodegradation and biocompatibility of PLA and PLGA microspheres. *Adv. Drug Deliv. Rev.* **64**, 72–82 (2012).
  56. Niaounakis M., *Biopolymers: Applications and trends, 2 Properties.* (2015). doi:10.1016/B978-0-323-35399-1.00002-8.
  57. Niaounakis, M. *Definitions of Terms and Types of Biopolymers. Biopolymers: Applications and Trends* (2015). doi:10.1016/b978-0-323-35399-1.00001-6.
  58. Ciardelli, F., Bertoldo, M., Bronco, S. & Passaglia, E. *Polymers from Fossil and Renewable Resources. Polymers from Fossil and Renewable Resources* (2019). doi:10.1007/978-3-319-94434-0.
  59. Elsayy, M. A., Kim, K. H., Park, J. W. & Deep, A. Hydrolytic degradation of polylactic acid (PLA) and its composites. *Renew. Sustain. Energy Rev.* **79**, 1346–1352 (2017).
  60. Lopes, M. S., Jardini, A. L. & Filho, R. M. Synthesis and characterizations of poly (lactic acid) by ring-opening polymerization for biomedical applications. *Chem. Eng. Trans.* **38**, 331–336 (2014).
  61. Rincon Lasprilla, A. J. *et al.* Synthesis and characterization of poly (Lactic Acid) for use in biomedical field. *Chem. Eng. Trans.* **24**, 985–990 (2011).
  62. Shenoy A.V., Saini D.R., *Thermoplastic Melt Rheology and Processing*, Founding editor, CRC Press, 1996.
  63. E. Alfredo Campo, 2 - Mechanical Properties of Polymeric Materials, In *Plastics Design Library, Selection of Polymeric Materials*, William Andrew Publishing, 2008, Pages 41-101, ISBN 9780815515517, <https://doi.org/10.1016/B978-081551551-7.50004-8>.
  64. John R. Wagner, Eldridge M. Mount, Harold F. Giles, 21 - Testing Properties, , In *Plastics Design Library, Extrusion (Second Edition)*, William Andrew Publishing, 2014, Pages 241-253, ISBN 9781437734812, <https://doi.org/10.1016/B978-1-4377-3481-2.00021-1>.
  65. Pape, H. C., Evans, A. & Kobbe, P. Autologous bone graft: Properties and techniques. *J. Orthop. Trauma* **24**, 36–40 (2010).
  66. Sachlos, E., Czernuszka, J. T., Gogolewski, S. & Dalby, M. Making tissue engineering scaffolds work. Review on the application of solid freeform fabrication technology to the production of tissue engineering scaffolds. *Eur. Cells Mater.* **5**, 29–40 (2003).
  67. Mao, A. S. & Mooney, D. J. Regenerative medicine: Current therapies and future directions. *Proc. Natl. Acad. Sci. U. S. A.* **112**, 14452–14459 (2015).
  68. Agrawal, C. M. & Ray, R. B. Biodegradable polymeric scaffolds for musculoskeletal tissue engineering. *J. Biomed. Mater. Res.* **55**, 141–150 (2001).
  69. Chiono V., Slides "Scaffold - Tecniche convenzionali" lecture from "Ingegneria per la medicina rigenerativa" course, Politecnico di Torino, a.y. 2017-2018.
  70. Qiang F, Bioactive glass scaffolds for bone tissue engineering: state of the art and future perspectives, *Mater Sci*

71. Frost Harold M., Wolff's law and bone's structural adaptations to mechanical usage: an overview for clinicians, *The angle orthodontist*, Vol. 64, No. 3, (1994). .
72. Gerhardt, L. C. & Boccaccini, A. R. Bioactive glass and glass-ceramic scaffolds for bone tissue engineering. *Materials (Basel)*. **3**, 3867–3910 (2010).
73. Baino, F., Novajra, G. & Vitale-Brovarone, C. Bioceramics and scaffolds: A winning combination for tissue engineering. *Front. Bioeng. Biotechnol.* **3**, 1–17 (2015).
74. Pina S., Oliveira J.M., Reis R.L. (2016) Biomimetic Strategies to Engineer Mineralized Human Tissues. In: Antoniac I. (eds) *Handbook of Bioceramics and Biocomposites*. Springer, Cham.
75. Hutmacher, D. W. Scaffolds in tissue engineering bone and cartilage. *Biomater. Silver Jubil. Compend.* **21**, 175–189 (2000).
76. [https://www.researchgate.net/figure/fig-23-Schematic-representation-of-solvent-casting-particulate-leaching-SCPL\\_fig3\\_283724828](https://www.researchgate.net/figure/fig/figure/fig-23-Schematic-representation-of-solvent-casting-particulate-leaching-SCPL_fig3_283724828).
77. [https://www.researchgate.net/figure/Scheme-explaining-the-differences-between-the-freeze-drying-and-salt-leaching\\_fig1\\_275407391](https://www.researchgate.net/figure/Scheme-explaining-the-differences-between-the-freeze-drying-and-salt-leaching_fig1_275407391).
78. E.M. Prieto, S.A. Guelcher, 5 - Tailoring properties of polymeric biomedical foams, Editor(s): Paolo A. Netti, *Biomedical Foams for Tissue Engineering Applications*, Woodhead Publishing, 2014, Pages 129-162, ISBN 9780857096968.
79. Bhattarai, R. S., Bachu, R. D., Boddu, S. H. S. & Bhaduri, S. Biomedical applications of electrospun nanofibers: Drug and nanoparticle delivery. *Pharmaceutics* **11**, (2019).
80. Zhou, J., Cao, C. & Ma, X. A novel three-dimensional tubular scaffold prepared from silk fibroin by electrospinning. *Int. J. Biol. Macromol.* **45**, 504–510 (2009).
81. Cheng, Z. & Teoh, S. H. Surface modification of ultra thin poly ( $\epsilon$ -caprolactone) films using acrylic acid and collagen. *Biomaterials* **25**, 1991–2001 (2004).
82. Förster, Y. *et al.* Surface modification of implants in long bone. *Biomatter* **2**, 149–157 (2012).
83. Devescovi, V., Leonardi, E., Ciapetti, G. & Cenni, E. Growth factors in bone repair. *Chir. Organi Mov.* **92**, 161–168 (2008).
84. Alizadeh-Osgouei, M., Li, Y. & Wen, C. A comprehensive review of biodegradable synthetic polymer-ceramic composites and their manufacture for biomedical applications. *Bioact. Mater.* **4**, 22–36 (2019).
85. ASTM International. F2792-12a - Standard Terminology for Additive Manufacturing Technologies. *Rapid Manuf. Assoc.* 10–12 (2013) doi:10.1520/F2792-12A.2.
86. Gibson Ian, *Additive Manufacturing Technologies*, 2nd edition, *Springer*, ISBN 978-1-4939-2112-6.
87. Do, A. V., Khorsand, B., Geary, S. M. & Salem, A. K. 3D Printing of Scaffolds for Tissue Regeneration

- Applications. *Adv. Healthc. Mater.* **4**, 1742–1762 (2015).
88. Bose, S., Vahabzadeh, S. & Bandyopadhyay, A. Bone tissue engineering using 3D printing. *Mater. Today* **16**, 496–504 (2013).
  89. Semba, J. A., Mieloch, A. A. & Rybka, J. D. Introduction to the state-of-the-art 3D bioprinting methods, design, and applications in orthopedics. *Bioprinting* **18**, e00070 (2020).
  90. Yousefi AM, Gauvin C, Sun L, DiRaddo RW, Fernandes J. *Polymer Engineering & Science.* (2007); 47:608.
  91. Wang, X., Jiang, M., Zhou, Z., Gou, J. & Hui, D. 3D printing of polymer matrix composites: A review and prospective. *Compos. Part B Eng.* **110**, 442–458 (2017).
  92. <https://www.3dnatives.com/en/nanoscribe-3d-printing-170620194/>
  93. Jiang, N. & Abe, H. Miscibility and morphology study on crystalline/crystalline partially miscible polymer blends of 6-arm Poly(l-lactide) and Poly(3-hydroxybutyrate-co-3-hydroxyvalerate). *Polymer (Guildf)*. **60**, 260–266 (2015).
  94. Kalsoom, U., Nesterenko, P. N. & Paull, B. Recent developments in 3D printable composite materials. *RSC Adv.* **6**, 60355–60371 (2016).
  95. Valino, A. D. *et al.* Advances in 3D printing of thermoplastic polymer composites and nanocomposites. *Prog. Polym. Sci.* **98**, 101162 (2019).
  96. J-H Shim, J.-Y. Won, S.-J. Sung, D.-H. Lim, W.-S. Yun, Y.-C. Jeon and J.-B. Huh, *Polymers*, 2015, 7, 2061–2077.
  97. J. L. Davila, M. S. Freitas, P. I. Neto, Z. C. Silveira, J. V. L. Silva and M. A. d'Avila, *J. Appl. Polym. Sci.*, 2016, 133, 9
  98. T. Serra, J. A. Planell and M. Navarro, *Acta Biomater.*, 2013, 9, 5521–5530..
  99. D. Puppi, C. Mota, M. Gazzarri, D. Dinucci, A. Gloria, M. Myrzabekova, L. Ambrosio and F. Chiellini, *Biomed. Microdevices*, 2012, 14, 1115–1127.
  100. Senatov FS, Niaza KV, Zadorozhnyy MY, Maksimkin AV, Kaloshkin SD, Estrin YZ. Mechanical properties and shape memory effect of 3D-printed PLA-based porous scaffolds. *J Mech Behav Biomed Mater* 2016; 57:139–48
  101. Serra T, Planell JA, Navarro M. High-resolution PLA-based composite scaffolds via 3-D printing technology. *Acta biomater* 2013;9(3):5521e30.
  102. Kim J, McBride S, Tellis B, Alvarez-Urena P, Song Y-H, Dean DD, Sylvia VL, Elgandy H, Ong J, Hollinger JO. Rapid-prototyped PLGA/b-TCP/hydroxyapatite nanocomposite scaffolds in a rabbit femoral defect model.
  103. Wu, C., Chang, J. & Fan, W. Bioactive mesoporous calcium-silicate nanoparticles with excellent mineralization ability, osteostimulation, drug-delivery and antibacterial properties for filling apex roots of teeth. *J. Mater. Chem.* **22**, 16801–16809 (2012).
  104. Büchi Labortechnik AG. Training Papers Spray Drying, 1–19 (2002).

105. Santos Daniel, Spray Drying: an overview, Chapter 2, *Biomaterials - Physics and Chemistry - New edition* 2018.
106. Kashi, S., Gupta, R. K., Baum, T., Kao, N. & Bhattacharya, S. N. Phase transition and anomalous rheological behaviour of polylactide/graphene nanocomposites. *Compos. Part B Eng.* **135**, 25–34 (2018).
107. Harper Charles A., Handbook of plastics, elastomers and composites, Fourth edition, McGraw-Hill
108. D.W. Van Krevelen, K. Te Nijenhuis, Chapter 21 - Thermal Decomposition, Editor(s): D.W. Van Krevelen, K. Te Nijenhuis, Properties of Polymers (Fourth Edition), Elsevier, 2009, Pages 763-777, ISBN 9780080548197, <https://doi.org/10.1016/B978-0-08-054819-7.00021-2>.
109. Thommes, M. *et al.* Physisorption of gases, with special reference to the evaluation of surface area and pore size distribution (IUPAC Technical Report). *Pure Appl. Chem.* **87**, 1051–1069 (2015).
110. Nina Hwang, BET Surface Area Analysis of Nanoparticles, 2011
111. <https://photometrics.net/field-emission-scanning-electron-microscopy-fesem>
112. Jena, B. P. et al. 4.1 Field Emission Scanning Electron Microscopy (FE-SEM) & Electron Dispersion X-Ray Spectroscopy (EDX or EDS). *Instrumentns Struct. Optimcal, Electr. Charact.* 65–92 (2014).
113. Information on the FESEM, *Radboud University Nijmegen*.
114. Zhou, W., Apkarian, R., Wang, Z. L. & Joy, D. Fundamentals of scanning electron microscopy (SEM). *Scanning Microsc. Nanotechnol. Tech. Appl.* 1–40 (2007) doi:10.1007/978-0-387-39620-0\_1.
115. Kohli Rajiv, *Chapter 3 - Methods for Monitoring and Measuring Cleanliness of Surfaces*, Developments in surface contamination and cleaning, 2012, Pages 107-178.
116. Chatterjee A.K., *8- X-Ray diffraction*, Handbook of Analytical Techniques in Concrete Science and Technology, 2001, Pages 275-332.
117. [https://serc.carleton.edu/research\\_education/geochemsheets/techniques/XRD.html](https://serc.carleton.edu/research_education/geochemsheets/techniques/XRD.html).
118. <https://www.zwickroell.com/en/materials-testing/tensile-test..>
119. <https://www.tec-science.com/material-science/material-testing/tensile-test/>.
120. Davis, J. R. Introduction to Tensile Testing. *Tensile Test.* 1–13 (2004).
121. <https://www.shimadzu.com/an/test/universal/index.html>
122. Malvern Instruments Worldwide. Malvern Instruments White Paper - A Basic Introduction to Rheology Shear Flow. 1–20 (2016).
123. De Vicente J., *Rheology* (2012). doi:10.5772/35145.
124. Understanding Rheology of Structured Fluids, TA instruments, <http://www.tainstruments.com/>
125. Bair, S. *et al.* Oscillatory and steady shear viscosity: The Cox-Merz rule, superposition, and application to EHL friction. *Tribol. Int.* **79**, 126–131 (2014).

126. The Principles And Applications Of The Cox-Merz Rule, TA instruments, Thermal analysis & Rheology.
127. Fiorilli S, Molino G, Pontremoli C, et al. The Incorporation of Strontium to Improve Bone-Regeneration Ability of Mesoporous Bioactive Glasses. *Materials (Basel)*. 2018;11(5):678. Published 2018 Apr 26. doi:10.3390/ma11050678.
128. Kulkarni, P., Dixit, M., Kulkarni, P. K., Kini, A. G. & Shivakumar, H. G. Spray drying: A crystallization technique : A review. *Int. J. Drug Formul. Res.* **1**, 1–29 (2010).
129. Cychoz K.A., Guillet-Nicolas R., Garcia-Martinez J., “Recent advances in the textural characterization of hierarchically structured nanoporous materials”, *Chemical Society Reviews*, 2017, 46:389-414
130. <https://www.lennotech.it/periodica/elementi/ca.htm>.
131. Karunanayake, L. The effects of glass powder on some mechanical properties of engineering thermoplastics. *J. Natl. Sci. Found. Sri Lanka* **35**, 13–17 (2007).
132. Nicholson, L. M., Whitley, K. S., Gates, T. S. & Hinkley, J. A. How molecular structure affects mechanical properties of an advanced polymer. *Int. SAMPE Symp. Exhib.* **44**, 1–15 (1999).
133. Fu C, Bai H, Zhu J, Niu Z, Wang Y, Li J, et al. (2017) Enhanced cell proliferation and osteogenic differentiation in electrospun PLGA/hydroxyapatite nanofibre scaffolds incorporated with graphene oxide. *PLoS ONE* 12(11): e0188352. <https://doi.org/10.1371/journal.pone.0188352>.
134. Kasuga, T., Ota, Y., Nogami, M. & Abe, Y. Preparation and mechanical properties of polylactic acid composites containing hydroxyapatite fibers. *Biomaterials* **22**, 19–23 (2000).
135. Bonfield, W., Grynblas, M. D., Tully, A. E., Bowman, J. & Abram, J. Hydroxyapatite reinforced polyethylene - a mechanically compatible implant material for bone replacement. *Biomaterials* **2**, 185–186 (1981).
136. Barnes, H. A. a Review of the Rheology of Filled Viscoelastic Systems. *Rheol. Rev.* **2003**, 1–36 (2003).

## Acknowledgments

First of all, I would like to thank Prof.ssa Chiara Vitale Brovarone and Prof.ssa Sonia Fiorilli for asking me to join their research group. Working on these themes was inspiring, and I can't wait to face the new challenges this path will bring.

I would like to profoundly thank Prof.ssa Sonia Fiorilli, for introducing me to this world and giving me the opportunity to live this experience.

I would like to thank Prof. Kenny Dalgarno, for your kind presence in Newcastle. You welcomed me as one of your students and when the inspiration was gone, your words and advices helped me.

Thanks to Priscila and Giorgia, for your infinite patience in correcting my work, never failing to help when something was not clear and always encouraging me for a better result. Thanks to Carlotta, who followed my first steps in the laboratory, and thanks to Federica, Giulia, Stefania and Mattia, for always being friendly.

Thanks to all my friends, for your presence and support in every moment, when near but also when far. Thanks to Christian, for your love, support and endless faith in my possibilities. Thanks to Letizia, friend and colleague from day one. Thanks to Virginia, your presence in our final days before graduation was important.

Part of my experience, the best one, was in another country, and I would like to thank the several people I met in this journey. Among all of you, I firstly would like to thank Prof. Piergiorgio Gentile, for unconsciously helping me in a crucial moment, when everything was new, and nothing seemed to be working. Your guidance helped me finding the right path.

Thanks to Annachiara, Giorgia, Michele and Simone, as every day in Newcastle with you was a good day and I will treasure every single moment we spent together. Thanks to you, Dalia, for your warmth. I am extremely grateful to have known you.

Thanks to Annie and Tim, for opening the doors of your house and making me think of it as my own. You made me feel part of your family and I will never forget you. The time spent in Newcastle would not have been the same without you and your house as first point of reference.

Last but not least, thanks to my Mom and brother Iacopo, all of this was possible because of your constant love, patience and support. The three of us are now so happier and stronger, and I love you very much.

This experience was a hard challenge yet a great opportunity, and I am happy and proud to say that I did it, thanks to each one of you.

From the bottom of my heart, thank you.

I do not take today for granted.